Flow Regime Identification in a Bubble Column

Von der Fakultät für Lebenswissenschaften

der Technischen Universität Carolo-Wilhelmina

zu Braunschweig

zur Erlangung des Grades eines

Doktors der Naturwissenschaften

(Dr. rer. nat.)

genehmigte

D i s s e r t a t i o n

von Willy Baudelaire Tchowa Medjiade
aus Bamenda, Kamerun

1. Referent: Professor Dr. Adrian Schumpe
2. Referent: Professor Dr. Peter Jomo Walla
eingereicht am: 13.01.2016
mündliche Prüfung (Disputation) am: 11.03.2016

Druckjahr 2016

Vorveröffentlichungen der Dissertation

Teilergebnisse aus dieser Arbeit wurden mit Genehmigung der Fakultät für Lebenswissenschaften, vertreten durch den Mentor der Arbeit, in folgenden Beiträgen vorab veröffentlicht:

Tagungsbeiträge

Tchowa Medjiade, W., Nedeltchev, S., Schumpe, A.: Flow Regime Identification in a Bubble Column by Analysis of the Pressure Fluctuations. (Kurzvortrag und Poster) 1st International Symposium on Multiscale Multiphase Process Engineering (MMPE), Kanazawa – Japan (2011).

Tchowa Medjiade W., Rosenbaum Alvaro, A., Nedeltchev, S., Schumpe, A.,: Analysis of the Pressure Fluctuations in a Bubble Column for Flow Regime Identification in Viscous Liquids. (Poster) 20th International Congress of Chemical and Process Engineering (CHISA), Prague – Czech Republic (2012).

Tchowa Medjiade, W., Rosenbaum Alvaro, A. Schumpe, A.: Analysis of the Pressure Fluctuations in a Bubble Column for Flow Regime Identification. (Vortrag) 21st International Congress of Chemical and Process Engineering (CHISA), Prague – Czech Republic (2014).

Tchowa Medjiade, W., Ngialou Ngouffo, W., Rosenbaum Alvaro, A., Schumpe, A.: Identification of Pressure Fluctuations Sources in a Bubble Column. (Kurzvortrag und Poster) 2nd International Symposium on Multiscale Multiphase Process Engineering (MMPE), Hamburg – Germany (2014).

Acknowledgement

This project becomes true thanks to the contribution of a bright spectrum of persons which can unfortunately not be all listed. However, I would like to thank especially:

Prof. Adrian Schumpe my academic supervisor, whose supervision went wide above the scientific level,

Prof. Dieter Kaufmann whose invitation in Germany and early supervision marked the beginning of this project,

My colleagues Dr. Nedeltchev, Dr. Ngo, Dr. Jatzwauck, N. Golfinger, E. Mohsenzadeh,

The students under my supervision A. Rosenbaum and W. Ngouffo whose daily collaboration cannot be listed,

Dr. D. Eiting, the research teams Menzel and Jördening, the technicians MM. Ahrens, Himstedt, Sladeczek, Harendorf, Pablocki and secretaries G. Schirmer, A. Scherbarth and C. Vogel who technically and humanly eased my daily life at the institute,

My spouse Dulcinée Medjiade who shared the daily stresses and difficulties with me, for her support and comfort,

My daughters E. Kitaye, E. Salem and E. Jireh for the joy and encouragement which were a valuable motivation for the challenges to be faced,

My elder sister Anny Tchowa Deumeni whose incessant financial, moral and spiritual support I cannot forget,

My (dead) father who put me on this way since my childhood, my mother Madelaine Tchowa for the sufferance she endured to grow me up me, my brethren Martinel Tchowa, Arice Tchowa, Clément Zol and Lionel Tchowa,

All these families which gave of their time, money to help me F. Lah (especially Olivia), F. Stumpe, F. Adjia, F. Miltner, F. Manyimb, F. Petersen, F. Knödler, F. Fami, F. Yimbou, F. Houmegni, F. Yanke, F. Foyet, F. Asselmann, F. Jung, F. Mazié,

My brother in Christ and friends Valerie Fowa, Rudie Baumgart, Pascaline Yedou, Elise Ekambi, Rolande Tchana, Conrad Bobale, Cédric and Gibril Djikeussi, Juray Saller, Madine Yakam, Diane Kepomwo, Thierry Ngang, H. Hausmann, Brice Yanze, Tatiana Nya, Olaf Neese, Thorsten Feuersänger, Klaus Becker, Lucie Fontem and Renart Tebo who all gave a significant contribution to the achievement of this work.

“Better the end of a thing than its beginning” Ecclesiastes 7:8a

Content

List of Figures

List of tables

List of symbols and abbreviations

a	Major axis of an ellipsoidal bubble	**m**
b	Minor axis of an ellipsoidal bubble	**m**
C_O	Sound velocity in the gas	**m s^{-1}**
d	Total number of defined spaces for the Kolmogorov entropy	**-**
d_0	Diameter of the sparger orifices	**m**
d_{eq}	Equivalent diameter of a sphere possessing the same volume	**m**
d_B	Diameter of a bubble	**m**
d_F	Fractal dimension	**-**
D_C	Inner diameter of the column	**m**
Eo	$\left(=\frac{\Delta\rho g {d_B}^2}{\sigma_L}\right)$ Eötvös number also known as the Bond number (Bo), ratio of the buoyancy (inertial force) to the surface tension	**-**
f	Frequency	**s^{-1}**
f_B	Frequency of bubbles release	**s^{-1}**
Fr	$\left(=\frac{{v_B}^2}{gL}\right)$ Froude number, ratio of the buoyancy to the gravitational force	**-**
F_B	Buoyancy (force)	**N**
F_D	Drag force	**N**
F_L	Lift force	**N**
g	Gravity acceleration	**m s^{-2}**
Ga	$\left(=\frac{\Delta\rho g L^3}{\nu^2}\right)$ Galilei number, ratio of the gravity force to the viscous force	**-**
h	Sensor axial location above the sparger	**m**
H	Hurst exponent	**-**
h_0	Height of un-aerated liquid	**m**
I_E	Total information entropy	**bit**
I_{max}	Maximum information entropy	**bit**
$J_{GL,W}$	Drift flux after Wallis et al. (1969)	**m s^{-1}**

$J_{GL,ZF}$	Drift flux after Zuber and Findlay (1965)	**m s^{-1}**
k	Consistency index	**Pa s^{n}**
K_E	Kolmogorov entropy	**bit s^{-1}**
l_o	Embedding dimension for K_E determination	**-**
L	Characteristic length of the bubble	**m**
L_d	Distance between the orifice and the bubble base	**m**
n	Flow behaviour index	**-**
n_c	the number of times the signal crossed the mean value	**-**
N	Size of the pressure dataset	**-**
N_h	Number of holes in the perforated plate	**-**
P	Operating pressure	**Pa**
P_i	Discrete pressure value	**Pa**
$\overline{P}$	Mean of a series of pressure values	**Pa**
p	Probability	**-**
Q	Gas volumetric rate	**m^3 s^{-1}**
R	Cumulated range of the signal	**Pa**
Re	$\left(=\frac{d_B v_B \rho_L}{\mu_L}\right)$ Reynolds number, ration of the buoyancy (inertial forces) to the viscous forces (friction)	**-**
S	Standard deviation for Hurst exponent determination	**Pa**
t_x	Time at the instant x	**s**
T	Length of time series	**s**
T_C	Average cycle time	**s**
u_0	gas velocity in the sparger orifice	**m s^{-1}**
u_G	Superficial gas velocity	**m s^{-1}**
u_L	Liquid velocity	**m s^{-1}**
v_B	Bubble velocity	**m s^{-1}**
V_B	Volume of a bubble	**m^3**
V_C	Volume of the plenum chamber	**m^3**
V_G	Volume of the gas	**m^3**
V_L	Volume of the liquid	**m^3**

We	$\left(=\frac{\rho_L L {v_B}^2}{\sigma_L}\right)$ Weber number, ratio of the buoyancy (inertial force)to the liquid surface tension	-
We$_0$	$\left(=\frac{\rho_G d_0 {u_0}^2}{\sigma_L}\right)$ Orifice Weber number suggested by Mersmann (1978)	-

List of abbreviations

AAD	Average absolute deviation
BC	Bubble column
CARPT	Computed automated radioactive particle tracking
CMC	Carboxymethyl cellulose
CompaCT	Compact computed tomography
DGD	Dynamic gas disengagement
GFC	Gas flow controller
HireCT	High resolution gamma-ray computed tomography
MEG	Mono ethylene glycol
PDF	Probability density function
PFS	Pressure fluctuation signal
PSD	Power spectral density

Greek symbols

γ	Skewness	**-**
Δh	Distance between two sensors used	**m**
ΔP	Operating pressure difference	**Pa**
ΔP_0	Still stand pressure difference	**Pa**
ε_G	Gas hold-up	**-**
ϵ	Defined space in which the orbitals are searched	**-**
κ	Kurtosis	**-**
μ_L	Viscosity of the liquid	**Pa s**
σ	Standard deviation	**Pa**
σ_L	Liquid surface tension	**N m^{-1}**
ϱ_L	Liquid density	**kg m^{-3}**
τ	Time lag	**s**
Φ	Power spectral density	**Pa^2 s**
$\mathcal{F}$	Fourier transform	**-**

1. Introduction

Bubble columns are multiphase reactors or contactors. In their simplest form, they are made of a vertical cylinder at the bottom of which a gas is supplied through a distributor. The absence of a mechanical agitating system solves the problem of reactors tightness; an important issue for industries, especially for processes carried out under high operating pressure. Additionally, because of their simple structure, bubble columns have low construction and maintenance costs. At last, the gas flow rate being almost the only operating parameter to be varied, the operations are simplified. Due to these advantages, bubble column reactors have gained importance in the petrochemical, the chemical and the biochemical industries.

However, under these attractive characteristics are hidden some disadvantages such as the high degree of back mixing and especially the difficulty of scale-up. Although the modelling of the behaviour of single bubbles rising in quiescent liquids has already been well performed, the hydrodynamics in bubble columns remains pretty tricky. It implies a sum of random phenomena and hardly predictable mechanisms. Thus, the prediction of the hydrodynamics in bubble columns has captivated the interest of many researchers during the past decades. This difficult task passes through the identification of the flow regimes and their boundaries.

Homogeneous and heterogeneous are the main flow regimes prevailing in an operating bubble column. Depending on several parameters proper to the equipment or the gas-liquid system in presence, additional flow patterns can be observed. The prevailing flow patterns define the quality of mixedness and the heat and mass transfer which in turn determine the performance the reactor.

The identification of the prevailing flow regime in bubbles columns started with visual observation and gas hold-up analysis. Most of the authors in the literature agreed then with the subjectivity of the first method and the lack of accuracy of the second one. The importance of this task led to the set-up of many other methods such as the analysis of the pressure fluctuations, the analysis of the conductivity in the continuous phase and the analysis of the sound produced by the flow. Nowadays, more sophisticated computed methods such as the automated particle tracking or the tomography focused the attention of many authors.

Among all these techniques, the processing of pressure fluctuation data is known as simple, cheap, and applicable both at laboratory and industrial scale (Vial et al., 2000), without influencing the flow in the reactor. These methods, which can be classified in statistical, spectral, fractal and chaos analyses, have unfortunately revealed numerous limits. The discrepancies between results reported in the literature can be easily pointed out.

The aim of this study is the optimisation of the pressure fluctuation analysis for bubble columns. This passes through the better understanding of the up to now used analysis methods and their applicability.

2. Theory

2.1 Bubble columns reactors

Bubble columns are used as contactors or chemical reactors for heterogeneous reactions. These include two phase (liquid-gas) and three phase (liquid-solid-gas) reactions. In the latter case, the solid is usually a catalyst in form of a powder suspended in the liquid.

The simplest bubble column (BC) as depicted on Figure 1A is made of a vertical cylinder equipped with a gas distribution unit at its base. For heat exchange purpose, the cylinder can be equipped with a double-wall. The gas distributors, also called spagers, are grouped into static and dynamic ones (Deckwer, 1992). Among the static distributors, perforated plates, sintered plates or simple inserted tubes can be mentioned (see Figure 1B). The volume of the cylinder and the ratio between its length and its inner diameter can vary widely. Deckwer (1992) reported volumes up to 20 000 m^3 depending on the application field. Many other types of BCs exist. These are specifically modified in order to improve their performance in relation to the processes they are used for. Among these, the airlift reactor can be mentioned.

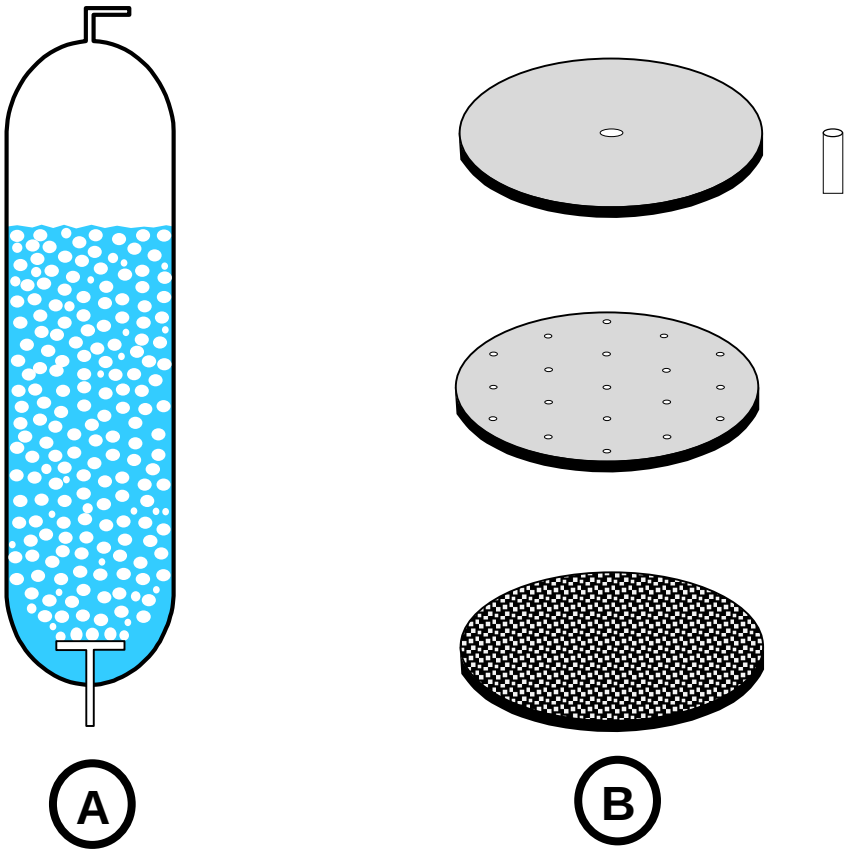

Figure 1: (A) simplified graph of bubble column, (B) three sparger types.

In a BC, the liquid which is the continuous phase can be fed in batch or continuous (upward or downward) mode. The gas, the discontinuous phase, is continuously injected through the sparger into the liquid within the column. Directly after the injection it forms bubbles. These bubbles rise to the top of the column because of the high density difference between the gas and the liquid phase. The dimensions of the formed bubbles depend on the gas distributor design and the gas flow rate but also the liquid/gas system used.

During their flow, the bubbles cause eddies, circulation and other motion within the continuous phase, resulting in a constant radial and axial mixing of the medium. The so provoked mixing induces good heat and mass transfer as widely reported in the literature (Deckwer, 1992); hence the uselessness of an additional mechanical agitation system.

At one hand, the absence of mechanical moving parts within the reactor solves the frequent problem of reactor tightness. This is a serious issue especially for reactors operated at high pressure. On the other hand, it allows the easy construction of extremely huge reactors with low production and maintenance costs. The main operating parameter of a BC is the gas flow rate which determines the hydrodynamics in the column.

In BCs the production costs are more equipment dependent at the opposite of the oil refining process that depends on raw material costs. Due to these advantages, BCs are therefore important reactors in the chemical, petrochemical, pharmaceutical, food and environmental industries (Ribeiro, 2008). Among its current application fields, the Fischer-Tropsch synthesis, the chlorination of toluene and the waste water treatment can be mentioned. The interesting features presented by this reactor lead nowadays to an increasing spectrum of its application. Kantarci et al. (2005) reported current investigations for new applications of bubble columns for bioprocesses.

At the opposite of these important features, BC reactors present a high level of back-mixing when operated at high gas rates. Moreover, the complex hydrodynamics of BCs leads to difficulties in their design and scale-up. Even if the modelling of the flow of single bubbles in different quiescent liquids has already been well performed, the hydrodynamics prediction of operating BCs including the different interactions between bubbles still remains tricky. It is therefore important to review the literature on the hydrodynamics in BCs and important models up to now set-up.

2.2 Hydrodynamics in a bubble column

The hydrodynamics in a BC is the consequence of complex processes which start with the bubble formation and end with the eruption at the liquid surface. The bubbles formed flow in particular features according to their properties (gas density, volume, shape) and those of the liquid (viscosity, density, surface tension). Their flow can take place with or without interactions between one another. The good understanding of the hydrodynamics in a BC passes through the mastery of these basic processes the bubbles go through.

2.2.1 Bubble formation process

According to the model developed by Ramakrishnan et al. (1969), two main steps characterise the bubble formation as depicted on Figure 2. These steps are:

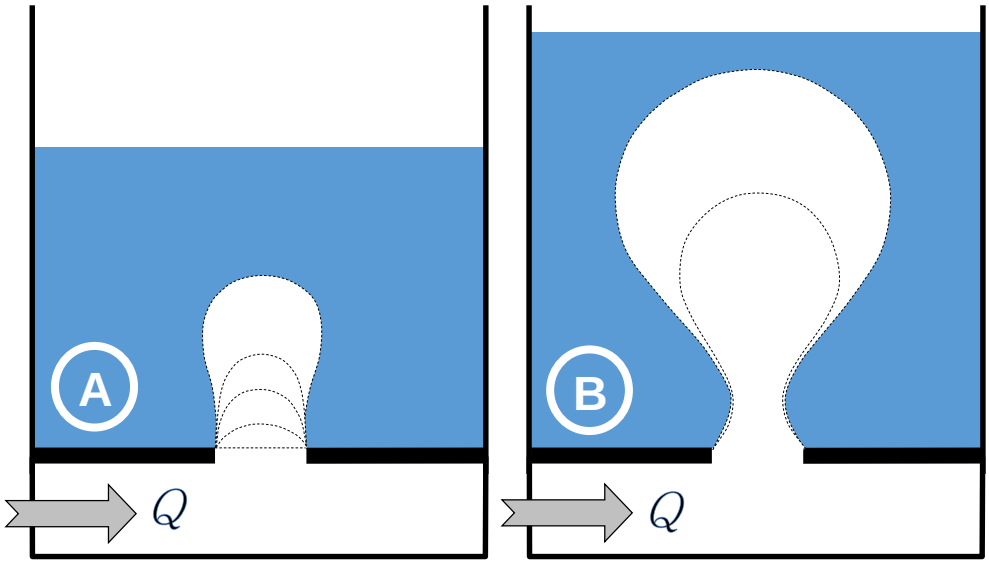

Figure 2: Bubble formation process, Ramakrishnan's model (1969) (A) expansion stage, (B) detachment stage.

- **The expansion stage:** Initially, the gas pressure in the plenum chamber and the pressure in the column due to the liquid are equal. Because of the constant flow of gas the pressure in the chamber overcomes the liquid's one and the bubble formation process starts. The gas entrance in the liquid faces the resistance due to the liquid gravity, the liquid viscosity and superficial tension. The continuous growth of the gas volume on the liquid side will soon lead to

the formation of a pocket as depicted on Figure 2A. This first phase is called expansion stage.

- **The detachment stage:** In the second step, the gas pocket has reached a volume high enough so that the buoyancy pulls it apart from the orifice. It is still connected to the orifice with a "neck" which is contracted by the surrounding liquid. At this level the process is non-reversible. The continuous growth of the gas pocket increases the buoyancy force. The cumulated effects of the buoyancy (pulling the bubble from the orifice) and the pressure of the liquid (strangulating the remaining connection) leads to final rupture of the neck: the detachment. During the detachment stage, the beginning of the expansion stage of the following bubble takes place at the same time.

The different parameters influencing the bubbles formation process and especially the detachment conditions have been widely studied in the literature and several models have been set-up. Although factors like the viscosity, superficial tension and gas density influence the bubble dimension, Davidson and Schüler (1960) reported that the controlling factors are mostly u_G and d_B (gas superficial velocity and bubble diameter respectively). They noted that the detachment process is also influenced by the liquid motion at the orifice. Kumar and Kulor (1970) proposed the relation $L_d = \frac{d_B}{2}$ for the detachment to take place, whereas Räbiger (1984) proposed $L_d = \frac{d_B}{4}$ where L_d is the distance between the orifice and the bubble base.

LaNauze and Harry (1974) reported that the pore size of the gas sparger plays an important role on the initial bubble size distribution and the frequency of the bubble release. They emphasized the importance of the plenum chamber and the gas momentum. The bubbles chain formation due to the gas momentum makes the bubbles differentiation difficult. They proposed equation 1 for the release frequency of single bubbles.

$$f_B = \frac{{C_o}^2 \rho_G Q}{V_C} \qquad (1)$$

Idogawa et al. (1987) confirmed that the critical gas velocity for the bubble release decreases as the orifice diameter increases and Adkins et al. (1996) reported that the increase of the operating pressure causes the sooner bubble release because of a greater upward force caused by the gas momentum.

2.2.2 Bubble geometry

Bubbles rise to the surface of the liquid because of the high density difference between gas and liquid. Due to the tendency to minimise the effect of the surface tension of the surrounding liquid, bubbles are spherical. But when rising, they are submitted to additional forces which can modify this geometry. Clift et al. (1978) classified various shapes of bubbles (elsewhere called regimes) depending on their Reynolds and Eötvös numbers (see Figure 3). The classification, later confirmed by Bagha and Weber (1981) includes the following types of bubbles.

- **Spherical bubbles:** Spherical bubbles (ratio of major to minor axis differs by less than 10%, Amaya-Bower and Lee, 2010) are usually of small diameter (d_B < 0.0013 m). Their geometry is mostly ruled by the surface tension and the viscosity of the liquid. They possess a smooth surface.

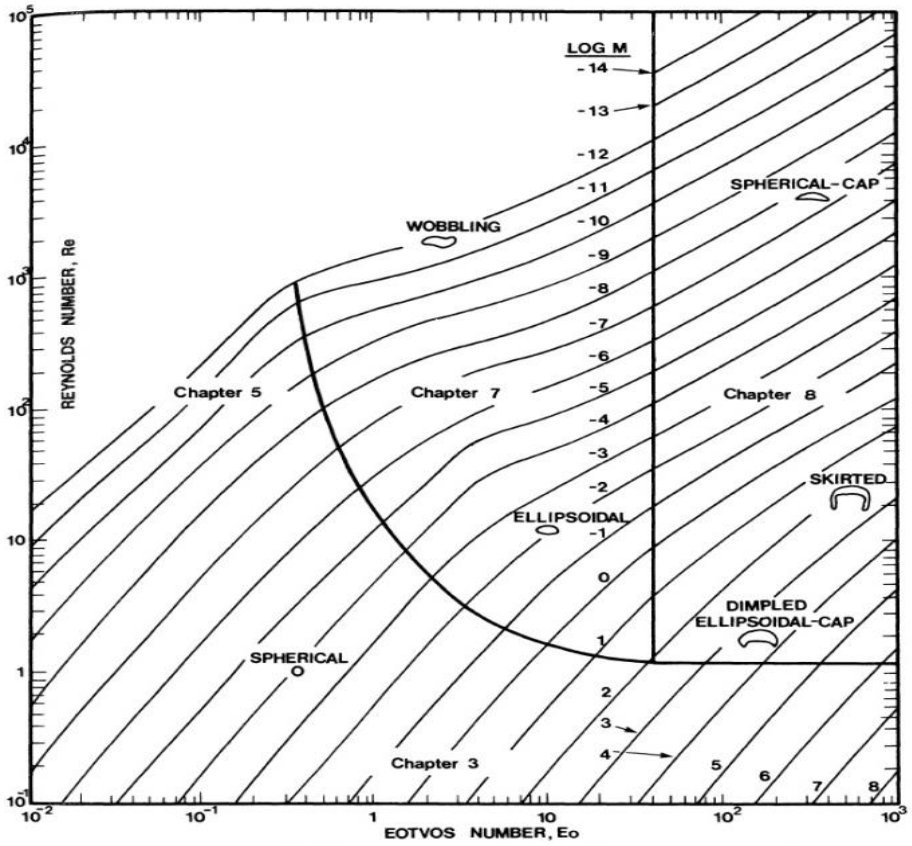

Figure 3: Different types of bubbles: classification according to Clift et al. (1978).

- **Ellipsoidal bubbles:** Above a critical diameter (0.0013 m < d_B < 0.006 m) according to Amaya-Bower and Lee (2010). During the flow, the surface tension alone prevails and the resistance due to the fluid causes the flattening of the bubble along its motion axe. For an ellipsoidal bubble, Kazakis et al. (2007) used the relation:

$$d_{eq} = \sqrt[3]{a^2 b} \qquad (2)$$

where $\boldsymbol{d_{eq}}$ is the equivalent diameter of a sphere possessing the same volume,

a is the major axis of an ellipsoidal bubble and

b the minor axis of an ellipsoidal bubble

Wobbling bubbles: For higher volumes, a characteristic shaking of the bubble interface is noticed during the rise. Veldhuis et al. (2008) reported that from the critical effective

diameter of 0.0028 m and above, the oblate ellipsoidal shape of bubbles was distorted by surface oscillation having a capillary nature. The Table 1 shows the oscillation frequencies reported by Veldhuis et al. (2008) for various bubbles in water. $f_{2,0}$ and $f_{2,2}$ are the bubble shape oscillation frequencies and f_{path} is the frequency oscillation of the bubble path about its minor axis.

Table 1: Measured frequency of bubble oscillation for several bubbles diameters (Veldhuis et al., 2008).

d_{eq} (mm)	$f_{2,0}$ (s^{-1})	$f_{2,2}$ (s^{-1})	f_{path} (s^{-1})	$f_{2,0}/f_{path}$ -	Path
3.0	61.8	40.6	6.7	6.0	Zigzag
3.4	50.7	34.0	7.0	4.9	Zigzag
3.6	45.5	-	5.5	-	Spiral
4.0	39.0	20.5	6.5	3.2	Flattened spiral
4.5	-	17.5	6.2	2.8	Titled flattened spiral
5.2	-	14.0	5.2	2.7	Chaotic

- **Spherical cap bubbles:** for d_B > 0.006 m, the inertia forces prevail on the flow entraining high turbulences. The front face of the bubble is spherical whereas the trailed face is globally flat.

2.2.3 Bubbles flow path

A rising bubble is submitted to three main forces which define its path. These are: buoyancy, lift and drag forces as depicted on Figure 4A. Abdulmouti (2014) presents the three rising paths of bubbles commonly reported in the literature. These paths are:

- **The straight rising path:** The straight (or rectilinear) rising path is presented on Figure 4B. It corresponds to a rectilinear motion of the bubble which is

usually observed for d_B < 0.81 mm, Re < 740 and We < 2.7 (Abdulmouti, 2014). This path is typical for bubbles with small diameter but can also be favoured by the liquid properties. In the case of a straight rising path, the bubble does not cause significant vortex after its passage.

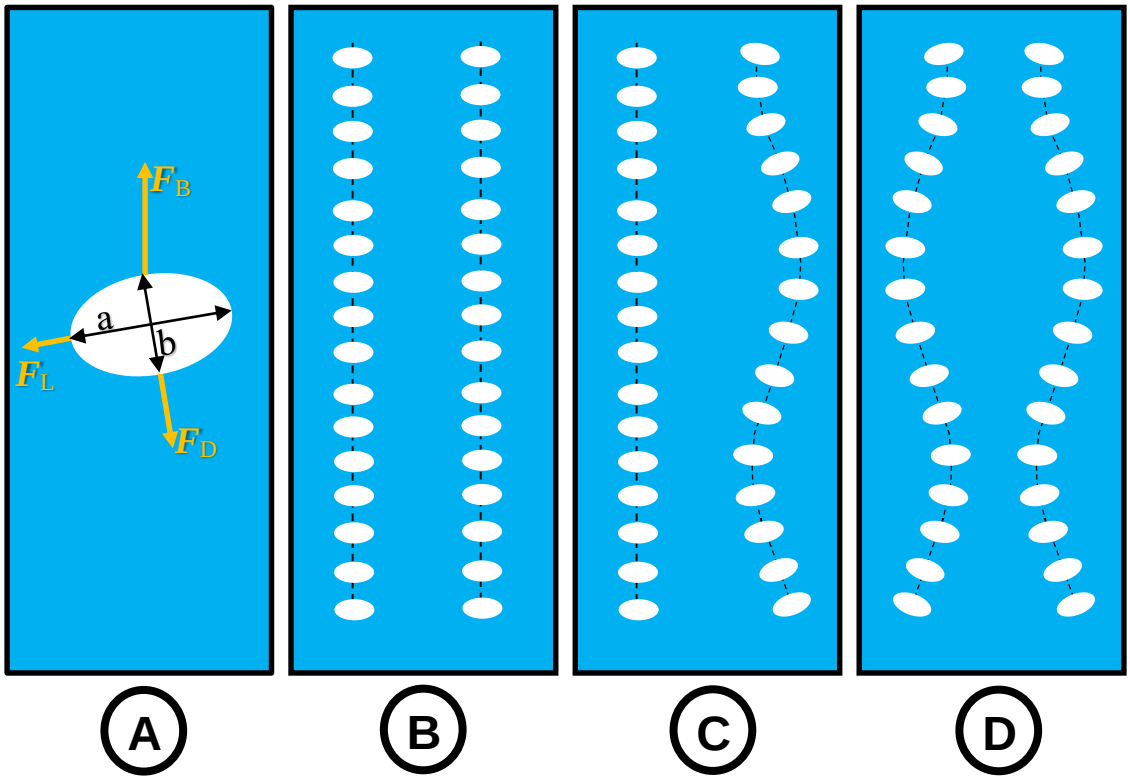

Figure 4: Bubbles rising process (A) Forces acting on a rising bubble, and mutually perpendicular view of a bubbles (B) rectilinear rising mode, (C) zigzagging rising mode, (D) spiralling rising mode.

with $\boldsymbol{F_B}$ the buoyancy (force) pulling the bubble upward,

$\boldsymbol{F_D}$ the drag force oriented along the bubble path and

$\boldsymbol{F_L}$ the lift force

- **The zigzagging rising path:** The zigzagging rising path corresponds to a sinusoidal pattern in one projection and a rectilinear one in the other projection plan as depicted on Figure 4c. There is an unstable wake close to the bubble.

- **The spiralling rising path:** The spiralling rising path corresponds to a sinusoidal pattern in both projection plans as depicted on Figure 4d. Bubbles rise spirally, although a top view of their motion does not depict a circle but an ellipsoid (Gerardus, 2001). The spiralling rise is characterised by a stable wake.

Gerardus (2001) reported that the curvature of the bubble path becomes zero when the buoyancy balances the lift force. The bubble path follows then the buoyancy direction and becomes linear. To avoid confusion between the different rise modes, a three dimensional tracking of the bubble is always necessary for the determination of its path. Figure 5 shows evidence of the bubble path oscillation in water for wobbling and non-wobbling bubbles and the possible induced wake (Veldhuis et al., 2008).

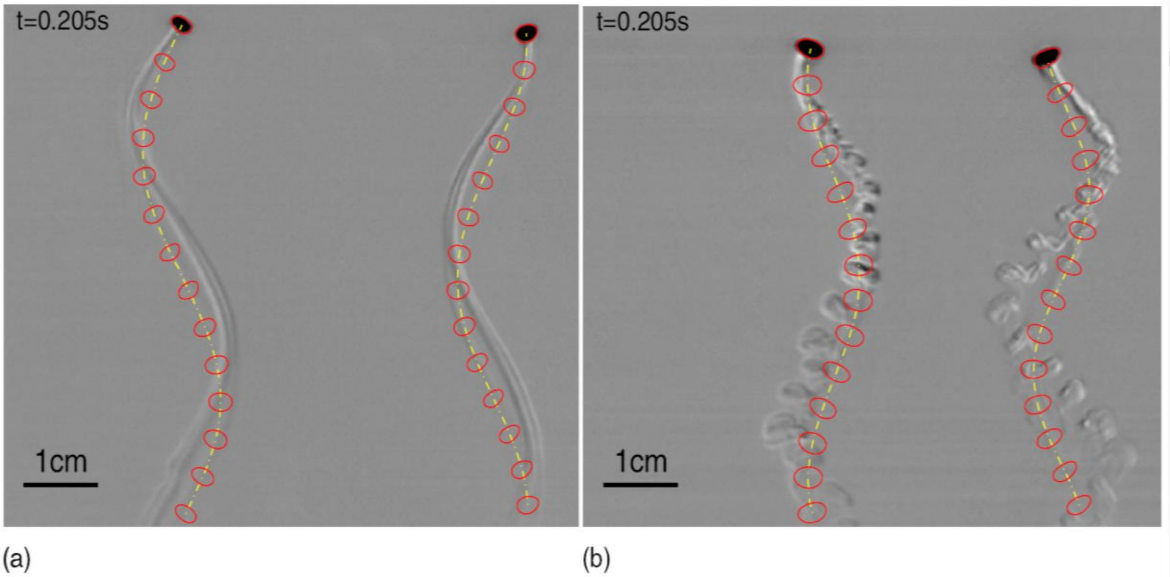

Figure 5: Bubbles rising in purified water (A) without shape oscillation (B) with shape oscillation (Veldhuis et al., 2008).

Many investigations have been carried out on the bubble terminal rise velocity and several models were developed. Figure 6 shows the influence of the bubble dimension on the terminal velocity.

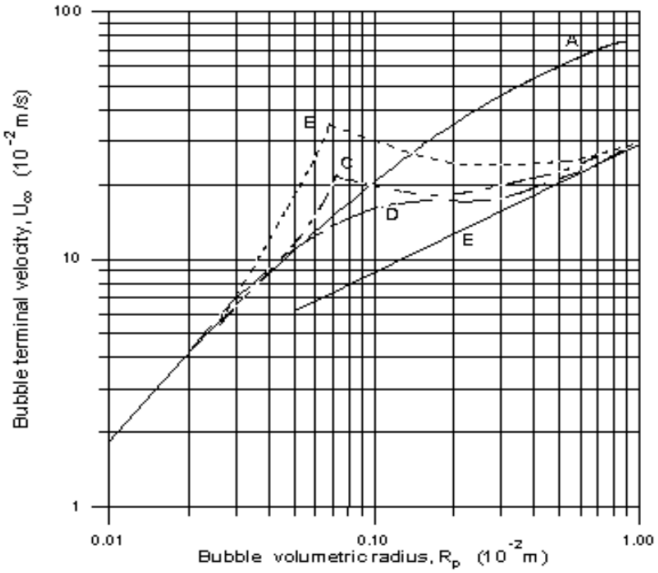

Figure 6: Terminal bubble rise velocity reported by Scheid et al. (1999) (A) The particle is a rigid sphere, (B) The bubble in distilled water, (C) The bubble in aqueous solution of terpeniol (3.7 10^{-3} kg/m^3), (D) The bubble in aqueous solution of terpeniol (2.2 10^{-2} kg/m^3), (E) The bubble is a spherical cap.

2.2.4 Bubble coalescence

Coalescence describes the process during which two distinct bubbles collide with one another and form a new single bubble. The coalescence process can be described in four successive steps as depicted on Figure 7:

- **The collision:** Two bubbles in motion approach and collide with each other. If the collision energy is not high enough, they can repel and simply continue their flow. But if the collision energy is high enough, the coalescence pursues its process. In

this case, Oolman and Blanch (1986) reported the flattening of the bubbles involved.

- **The film formation:** The successful collision of two bubbles leads to the formation of a two-bubble system, bound and separated by a film (see Figures 7A and 7B). Oolman and Blanch (1986) reported that the film has a thickness between 10^{-3} and 10^{-4} m for aqueous systems.

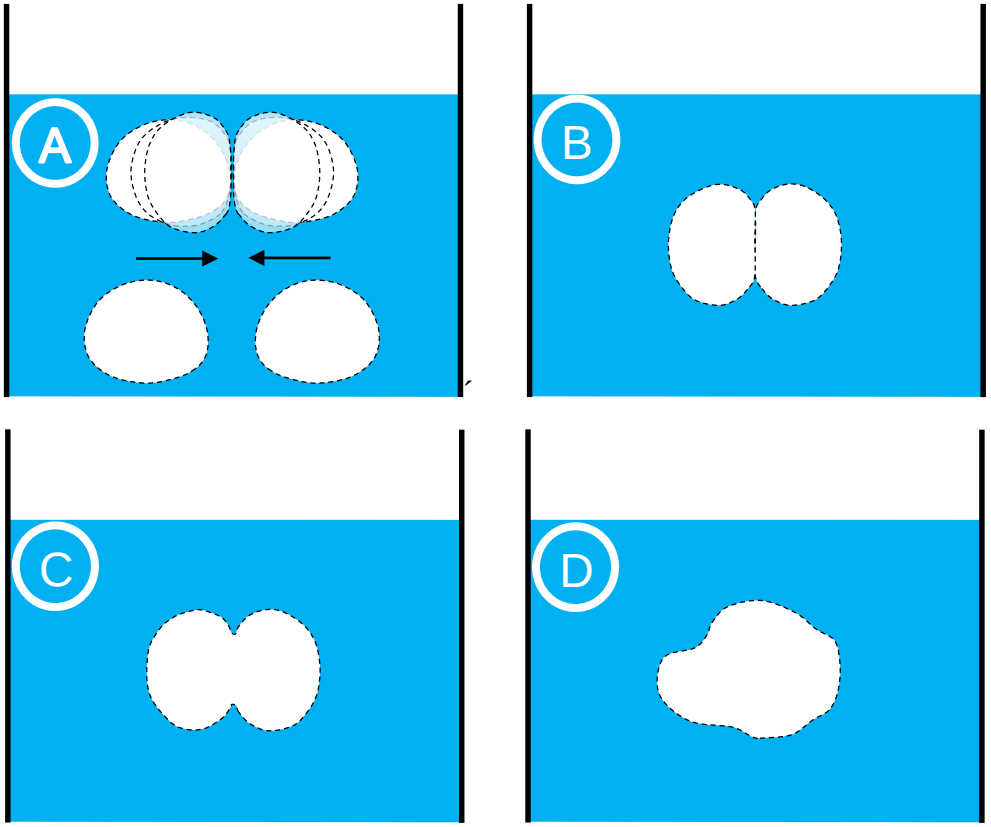

Figure 7: The bubble coalescence steps.

- **The film rupture:** According to Oolman and Blanch (1986), the film formed goes through a thinning process till a critical value around 10^{-6} m is reached. If the thinning lasts longer than the collusion duration, film rupture will not occur. Otherwise, the thinning process reaches the critical value and ends with the break-up of the remaining film. This step happens at a much faster speed that the two previous ones.

- **The bubbles fusion:** With the film rupture, the bubbles' fusion takes place. The new larger bubble mutes to a geometry adequate to the hydrodynamic conditions.

In an operating BC, the collision does not always happen frontally and between bubbles of comparable dimensions. Collisions between large rising bubbles with high velocity and smaller ones rising in the same direction but at lower velocity occur frequently. It can take place frontally and tangentially as well.

The evidence of another case of coalescence taking place at the sparger was reported by Kazakis et al. (2007). They mention the possibility of bubble coalescence during the formation process if the orifices are too close one another, as it is the case for porous plates.

2.2.5 Bubble break-up

The break-up describes the process during which a large mother bubble is split to give birth to at least two distinct daughter bubbles. According to Clift et al. (1978), this phenomenon can happen through two different ways. These are:

- **Break-up due to resonance:** Wobbling bubbles (see part 2.2.2) can break-up in a turbulent flow when their vibration frequency matches that of the field in which they flow (Clift et al., 1978).

- **Break-up due to velocity gradient:** The shear caused by the velocity gradient entrains a continuous elongation of the bubble which ends up in its splitting. Figure 8 depicts this break-up process, which usually ends up with the simultaneous formation of small satellite bubbles.

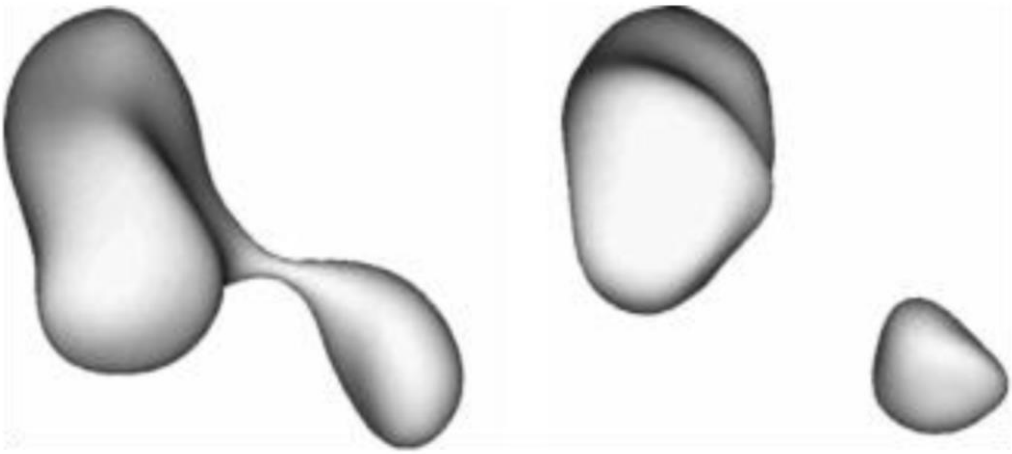

Figure 8: The bubble break-up process according to Brennen (2005).

The break-up and bubbles motion can hardly be predicted. The initial and the final condition are difficult to be determined. Abdulmouti (2014) reported a difference of spectrum energy decrease with wavenumber between the simulation and the experiments. Because of the likehood associated to the break-up process, Qian et al. (2006) characterised it as a stochastic phenomenon.

2.2.6 Bubble eruption process

The eruption (also called bursting) is the process during which a bubble is released at the surface of the liquid. Brennen (2005) describes this process in four main steps illustrated on Figure 9. These steps are:

- **The film formation:** The bubble arriving at the surface emerges progressively as depicted on Figure 9a. The liquid film covering the front side of the moving bubble grows and, at the same time, the film thickness decreases.

- **The film break-up:** When the (decreasing) film thickness reaches a critical value, the buoyancy forces overcome the film resistance, leading to film break-up as depicted on Figure 9B. As a result, the exit passage is opened for the gas which is ejected from the liquid. The sudden break-up of the film can also lead to the creation of droplets, especially for liquids with low viscosity.

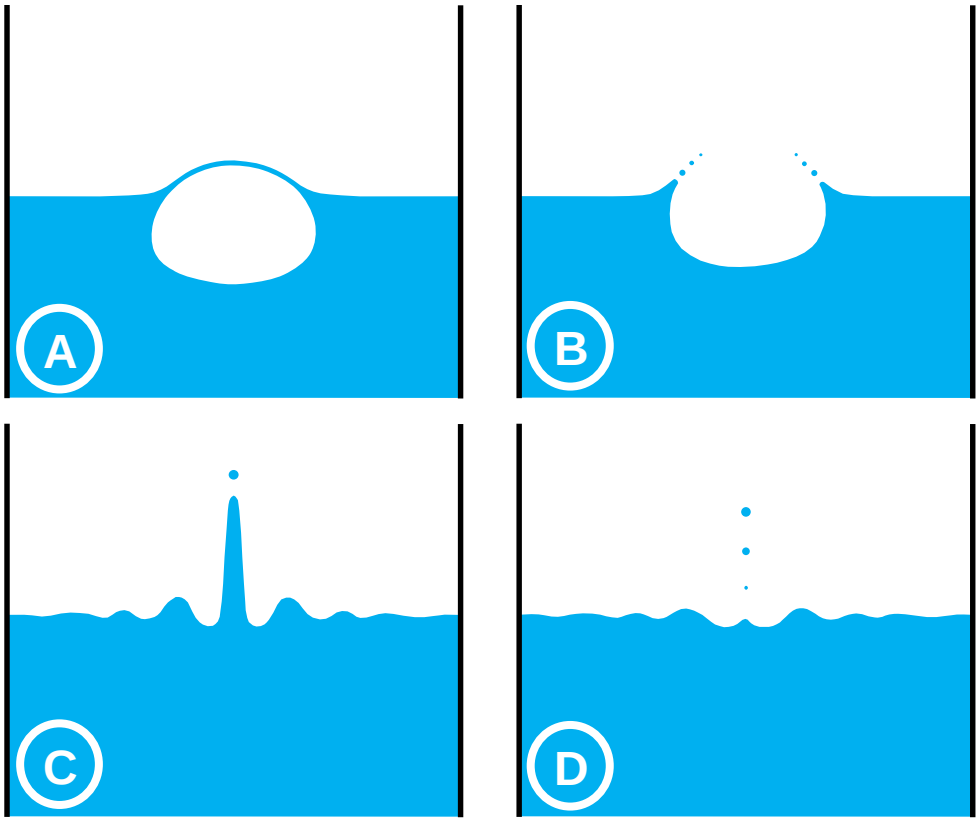

Figure 9: The bubble eruption process

- **The jet formation:** The sudden rupture of the surface film, characterised by Kientzler et al. (1954) as an extremely rapid phenomenon, causes a fast retraction of the remaining film and the collapse of the cavity left (surface tension). Whereas the film withdrawal occurs centrifugally, the cavity's collapse (i.e. the liquid filling the space released by the bubbles) takes place centripetally. These concentric liquid motion towards the axis results in a masses collision at the focus. The collision provokes a shock wave and generates a jet as depicted on Figure 9C. Some liquid droplets can be ejected.

- **The jet break-up:** Finally, because of the gravitational forces and the surface tension, the jet collapses, hitting the liquid at the focus. Kientzler et al. (1954)

reported that, for large bubbles, the liquid droplets were relatively large (about one tenth of the bubble size) and could bounce once or twice at the liquid surface.

The bubble eruption can adopt special features, depending on the bubble type, the bubbles size and the liquid properties. Lee et al. (2011) reported the limiting conditions hindering the jet formation.

2.2.7 Encountered flow regimes

The simultaneous and continuous formation of bubbles at a sparger and their rise in a BC leads to particular patterns called flow regimes. Figure 10 illustrates the flow regimes in two phases BC, from very low to very high values of u_G, as Zhang et al. (1997) reported.

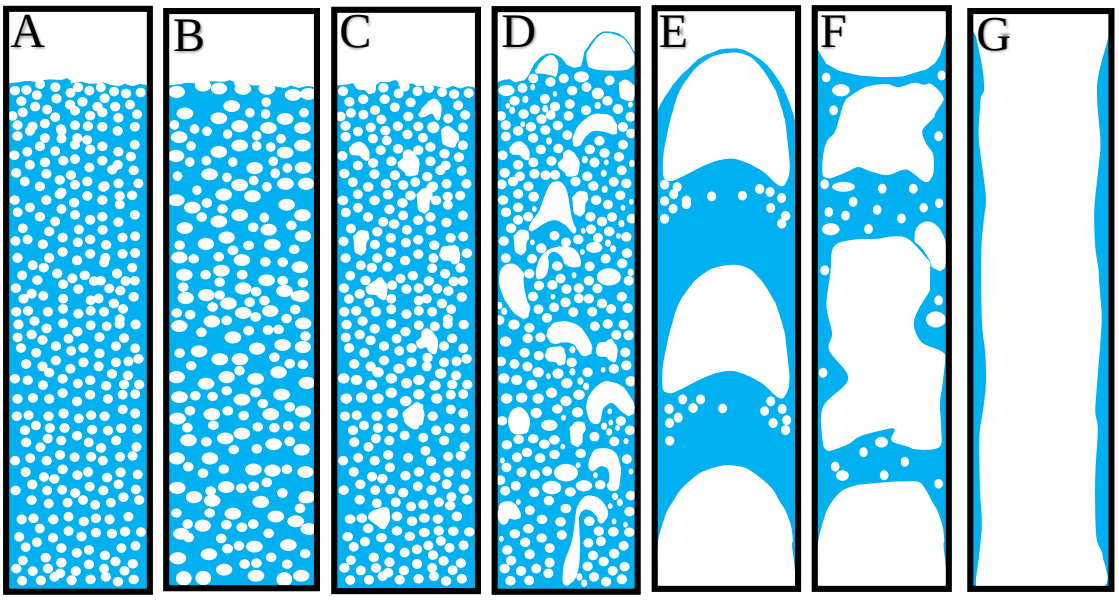

Figure 10: Encountered flow regimes in bubble columns (Zhang et al., 1997).

The homogeneous flow regime, also called bubbly flow regime, is the flow of relatively small bubbles with a negligible size distribution, rising without (or with minor) interaction. They flow in straight vertical paths; their low velocity is comparable to that

of a single bubble. This regime takes place at low gas velocity. The design of the sparger determines the geometry of the bubbles and their occupation of the full section of the column, which usually leads to no radial profile of the gas hold-up. Absence of the homogeneous flow regime was mentioned for the use of single-whole distributors and for viscous liquids such as monoethylene glycol (MEG).

Zhang et al. (1997) distinguished a perfect bubbly regime (unique bubble diameter as depicted on Figure 10A) from an imperfect bubbly flow regime (slight distribution of the bubble diameter as depicted on Figure 10B). In the same view, Kazakis et al. (2007) called it "pseudo-homogeneous regime", later confirmed by Yang et al. (2010) in their study with viscous liquids. Some authors like Wilkinson et al. (1992) proposed the linear increase of the gas hold-up with the gas velocity as the criterion for the homogeneous regime.

Typical application fields of the homogeneous flow regime in industry are bioprocesses such as the cultivation of bacteria, the cultivation of mold fungi, the production of single cell protein, the animal cell culture and the treatment of sewage. Some chemical processes such as the hydro-conversion of heavy oil are also carried out under these conditions (Shaikh and Al-Dahhan, 2007).

The transition flow regime, also called coalesced or interacting flow regime, starts when the bubbles interact with each other. The divergencies concerning the encountered interactions can be easily pointed out. Drahoš et al. (1991) reported the appearance of bubbles clusters resulting in liquid circulations which lead to coalescence and break-up phenomena. Chilekar (2007) related the regime to the formation of the first large bubble at the sparger with a diameter greater than 6 mm. Ruzicka et al. (2001) considered the transition regime as a smooth change, the coexistence of homogeneous and heterogeneous flow regime. Nedeltchev et al. (2007) carried out a study focussed on that region and reported the existence of two distinct phases within the transition. Finally, the transition regime is even not mentioned by many authors and just assimilated to the churn-turbulent flow.

The churn-turbulent flow regime, also called heterogeneous or turbulent flow, is described as the simultaneous flow of bubbles interacting with each other and having a wide size distribution. These interactions (coalescence and break-up in equilibrium according to Letzel et al., 1997) are mainly due to the helicoidal rise of large bubble in the core of the column, leading to high turbulence and a radial profile of the gas hold-up.

The churn-turbulent flow regime is mostly used in the chemical industry for reactions such as the Fischer-Tropsch synthesis and the chlorination of toluene (Shaikh and Al-Dahhan, 2007).

The experimental results obtained in pilot plants with inner diameter, $D_C \leq 0.15$ m present difficulties to be extrapolated to the industrial scale. In such "narrow" BCs, special flow features can be observed for high u_G values and viscous liquids. These particular flow features are:

The slug flow regime, illustrated on Figure 10E, is a flow in which bullet-shaped large bubbles and dispersed bubbly flow portions appear alternately (Matsui, 1984). The gas phase appears as large spherical-capped bubbles, stabilised by the column wall (Wild et al. (2003) and followed by a collection of much smaller voids in bubbly form (Vince and Lahey, 1982). This flow pattern causes high axial mixing.

The bridging flow regime, depicted on Figure 10F corresponds to the gas flow in form unshaped large bubbles pushing the liquid towards the wall, but frequently interrupted by liquid bridges occupying the core of the column, hence the name: "bridging flow". The gas forms almost a continuous phase in the core of the column but the liquid gravity intermittently overcomes the shear due to the gas.

The annular flow regime, depicted on Figure 10G, corresponds to the liquid flow on the wall of the pipe whereas the gas-phase (containing small liquid droplets) flows in the center (Matsui, 1984).

2.2.8 Flow regime boundaries

The flow regime map presented on Figure 11 was developed by Shah et al. (1982). It roughly shows the boundaries between the slug, the homogeneous and the heterogeneous regime as a function of the superficial gas velocity (u_G) and the column diameter (D_C) for water as the liquid phase.

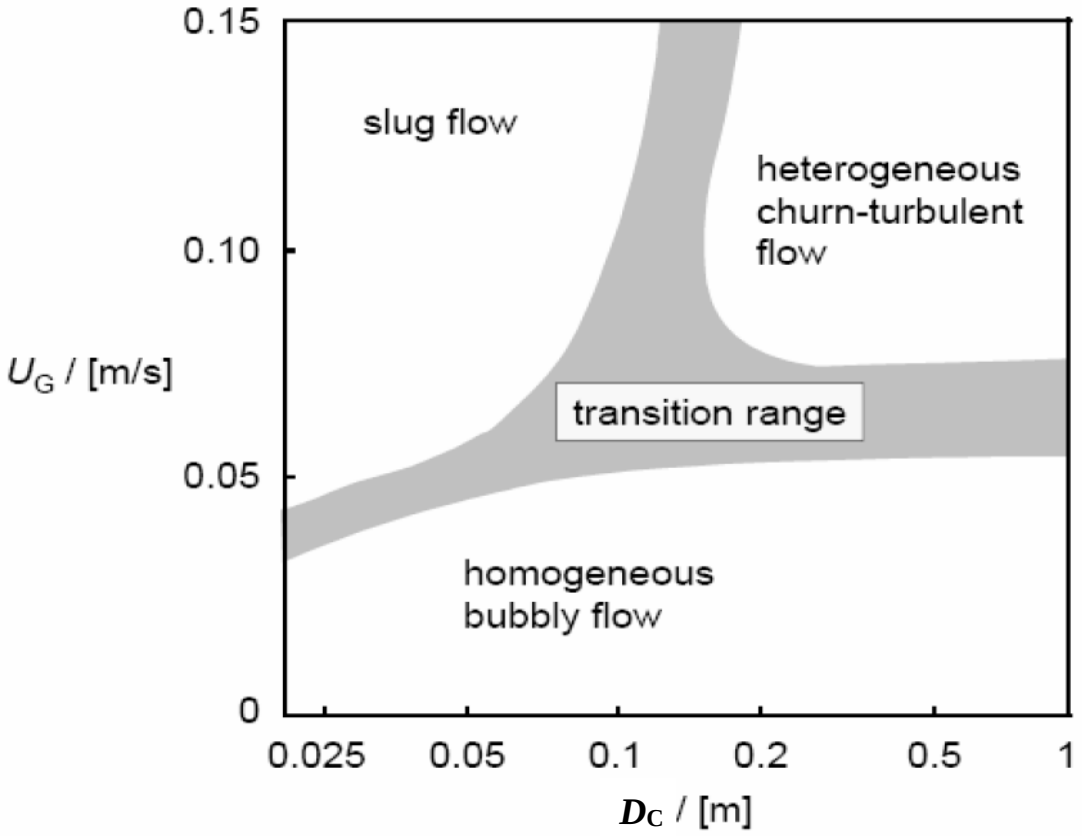

Figure 11: Regimes boundaries in water, (Shah et al., 1982).

Each of the previously presented flow regimes corresponds to specific axial dispersion, heat and mass transfer characteristics which highly influence the reactor performance. Seek for optimisation led to the development of many methods for the identification of flow regimes and the boundaries between them.

2.3 Flow regime identification methods

The identification of flow regimes started by visual observations carried out on transparent horizontal pipes. Later the studies were extended to inclined, then vertical pipes and to the hydrodynamics in BC. The gain in interest led to the development of new sophisticated methods. Among these methods are the Computed Automated Radioactive Particle Tracking (CARPT), the High Resolution Gamma-Ray Computed Tomography (HireCT) and the Compact Computed Tomography (CompaCT). Because of the high technological level, such methods face the disadvantage of high cost and their non-applicability to operating reactors at the industrial scale. The following literature review on the identification of flow regime is focussed on the so called "classical methods" (visual observation and gas hold-up analysis) and the signal processing of the pressure fluctuation recordings.

2.3.1 The classical methods

a. Visual observation and photography

The first flow regime charts were based only on visual observations (Drahoš and Cermak, 1989). These studies were carried out on narrow transparent tubes (D_C ~ 2 to 4 cm) where the fluids behaviour could be easily observed. Changing gradually the superficial velocity u_G allowed the establishment of the flow regime boundaries. Later, the need of more objectivity in the investigations led to the use of back-light high speed photography, which could enhance the reliability level of assertions made. It allowed the view of bubbles in-situ during their flow. Despite this new information, the discrepancy of the established models was noticed and the subjectivity of the method was pointed out by Matsui (1984 and 1986). The visual methods require a high number of photos (up to 200 per velocity step) which have to be analysed one after another. Moreover, these pictures represent usually a specific zone of the reactor, which is not necessarily representative of the hydrodynamics in the entire column. The recent work of Li et al. (2013) depicted on Figure 12 confirms this assertion. The flow transition cannot be objectively and clearly distinguished on the sole basis of the photos presented.

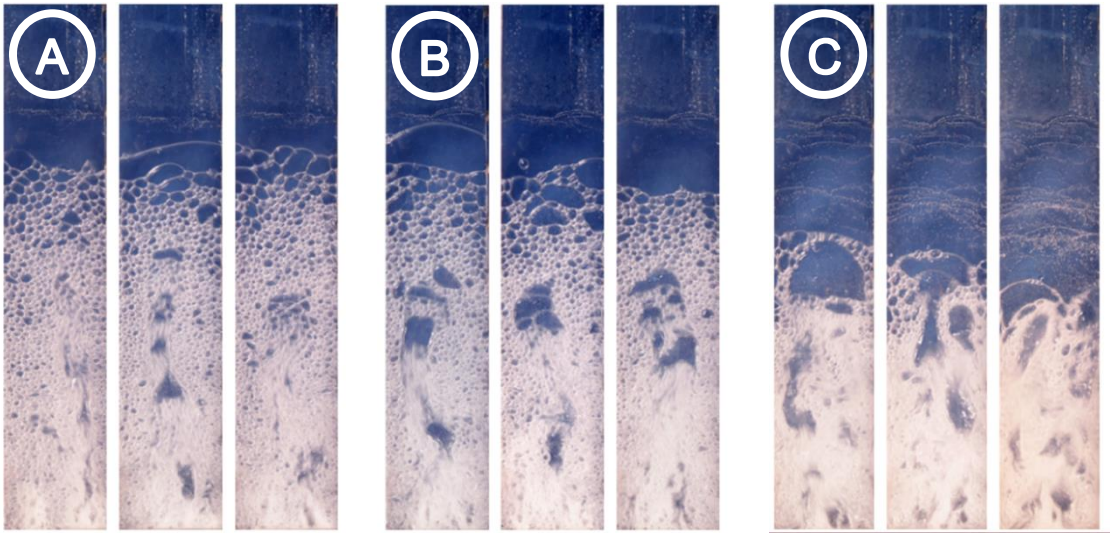

Figure 12: Pictures of the flow structure, Li et al. (2013): (A) before the transition, (B) at the transition and (C) above the transition.

Finally, the application of the visual method cannot be extended to industrial BC or those with large diameter (Letzel et al., 1997 and Chilekar et al., 2007). That is why 2D BCs (two dimensions BC) were developed. Their narrow rectangular cross section enables the viewing and recording of the flow. This allowed Chilekar et al. (2007) to show evidence of the presence of bubble clusters in the homogeneous regime. However, from the restraint due to the walls arises the question of the validity for industrial reactors.

Nowadays, the visual method is still used, but more for the better understanding of the hydrodynamics. Recently, Li et al. (2013) emphasized their findings on the transition point identified with other methods, using photos snapped in the different flow regions. The pictures were taken at the top of a 2D BC and showed evidence of the bubbles coalescence and the decline of the expansion height of the bed related to the flow pattern.

b. Gas hold-up

The gas hold-up (ε_G) or void fraction represents the ratio of the gas volume (V_G) to the total volume of the dispersion:

$$\varepsilon_G = \frac{V_G}{V_G + V_L} \tag{3}$$

where V_L is the volume of the non-aerated liquid

From the axial pressure difference in an unaerated BC (ΔP_0) and that in the aerated BC (ΔP), local values of the gas hold-up can also be determined:

$$\varepsilon_G = \frac{\Delta P_0 - \Delta P}{\Delta P_0} \tag{4}$$

The evolution of ε_G as a function of u_G has been widely studied for flow regime identification. It is characterised by proportionality of ε_G to u_G in the homogeneous phase. This phase ends with the split of the curve from the initial line. The following transition phase is shorter and often characterised even by a decrease of ε_G as u_G increases. Then, in the heterogeneous phase, ε_G adopts once more a positive but smaller slope than in the homogeneous phase.

The sparger design can highly influence the previously described trends, e.g., depending on the hole diameter (d_0) in a perforated plate. The perforated plate (A) of Figure 13 possess 0.5 mm diameter holes. The trend it shows resembles that observed for porous plates, which Vial et al. (2000) proved to give sharp slope changes. The trends depicted by the plate B, which possess 1.6 mm holes diameter is similar to that of nozzle distributors.

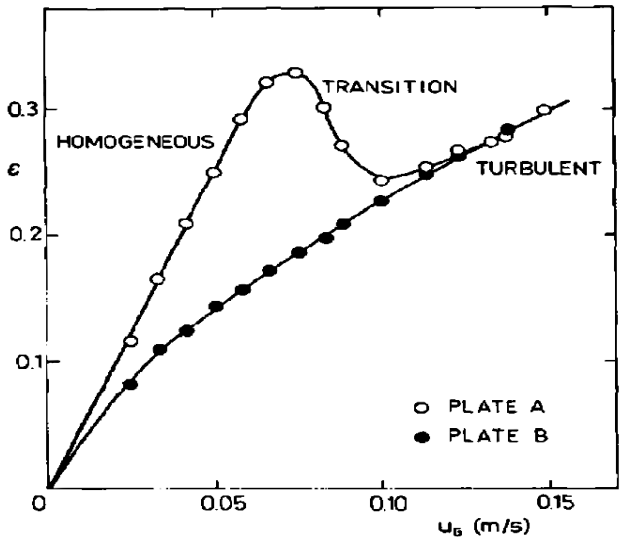

Figure 13: Gas hold-up as a function of the superficial gas velocity (perforated plates, water/air), (A) $d_0 = 0.5\times10^{-3}$ m (B) $d_0 = 1.6\times10^{-3}$ m (Drahoš et al., 1991).

The transition phase can shows zero to highly negative slope (Lin et al., 2001) depending on the sparger and the liquid. Nedeltchev et al. (2007) and Vial et al. (2000) showed that the transition could totally be missing. This last case is very well illustrated by the plate B shown on Figure 13. Even if Letzel et al. (1997) reported that it was impossible to determine an exact transition point based on the gas hold-up, ε_G is still widely used by many authors as a standard.

To improve the accuracy, it was proposed to use the drift flux which is calculated from gas hold-up.

c. Drift flux

Zuber and Findlay (1965) defined the drift flux as the ratio of the superficial gas velocity to the gas hold-up:

$$J_{GL,ZF} = \frac{u_G}{\varepsilon_G} \tag{5}$$

Later, Wallis (1969) proposed another expression for the drift flux, which (for $u_L = 0$) is defined as:

$$J_{GL,W} = (1 - \varepsilon_G)u_G \tag{6}$$

It is usually plotted as a function of the gas hold-up (ε_G).

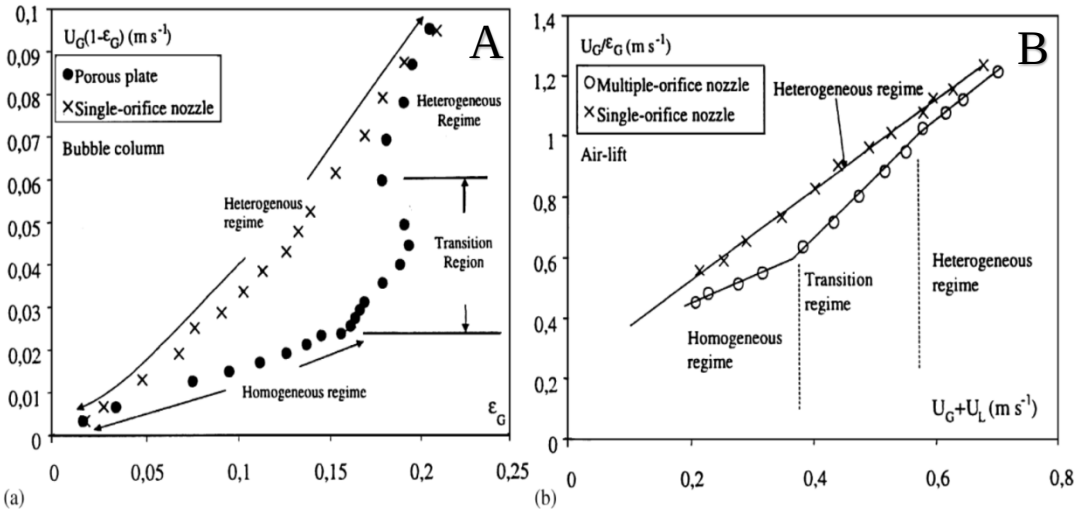

Figure 14: Drift flux (Vial et al., 2000): (A) Wallis method as a function of ε_G, (B) Zuber and Findlay method as a function of u_G.

Figure 14 shows typical graphs obtained with the two drift flux models. The Wallis expression presents an inverted version of ε_G, whereas the Zuber and Findlay's expression depicts strait lines with different slopes. Lin et al. (1999) used the drift flux for the identification of the regime transition in a high pressure BC. It was also used by Vial et al. (2000), Barghi et al. (2004) and Gourich et al. (2006) at atmospheric conditions. Except for the results reported by Gourich et al. (2006), the trends obtained in the literature are all similar.

Besides the previously explained methods, Grund and Schumpe (1986) used the pressure difference signal to analyse the bubbles size distribution based on the gas disengagement technique.

d. Dynamic gas disengagement (DGD)

Seeking for the setting up of new methods for an accurate determination of the bubbles size distribution led to the development of the gas disengagement. This method was initially proposed by Sriram and Mann (1977). It is based on the rise velocity difference existing between bubbles of different volume. It consists in stopping suddenly the gas supply of an operating bubble column. At higher pressure, a valve in the off-gas line has to be closed simultaneously. The drop of the dispersion height or the increase of the pressure difference between two sensors at different axial positions gives information

about the bubbles classes in presence. Figure 15 depicts a representative case of dynamic gas disengagement based on the pressure difference carried out at heterogeneous flow. Three steps can be observed:

- **The stationary phase:** Up to the instant t_0, the reactor is working in a stationary mode at constant u_G. The pressure difference signal is proper to the prevailing regime.

- **The disengagement phase:** At the time t_0 the gas supply is suddenly stopped. During the phase II, the large bubbles possessing a higher rise velocity flow fast out of the observed region, carrying a fraction of small bubbles in their motion. The nature of their flow provokes high fluctuation observable on the graph. The last large bubble passes the upper sensor at the instant t_1. During the phase I, the remaining fraction of small bubbles flows out of the measuring region at a nearly constant velocity. Because of their size and number, small bubbles produce a smooth signal.

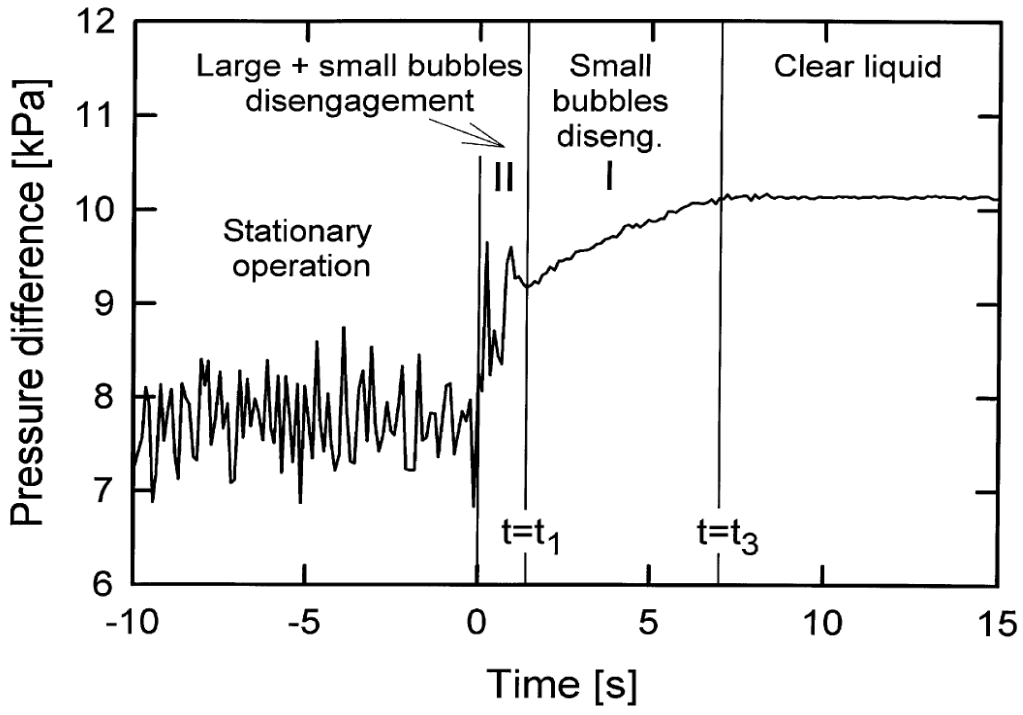

Figure 15: Dynamic gas disengagement at heterogeneous flow: u_G = 0.20 m s^{-1}, toluene/helium, P = 3×10^5 Pa (Jordan et al., 2003).

- **The still phase:** From the time t_3 all bubbles have left the observed region (clear liquid).

A simplified and smoothed version of this graph is given for the homogeneous and heterogeneous regimes by Figure 16. The stationary phase is replaced with a horizontal line representing the mean value of the pressure difference. The number of sub-regions during the disengagement phase corresponds to the number of bubble classes present in the mixture. If the disengagement is performed in a BC operating in the homogeneous regime, a single smooth slope will be observed as depicted on Figure 16.

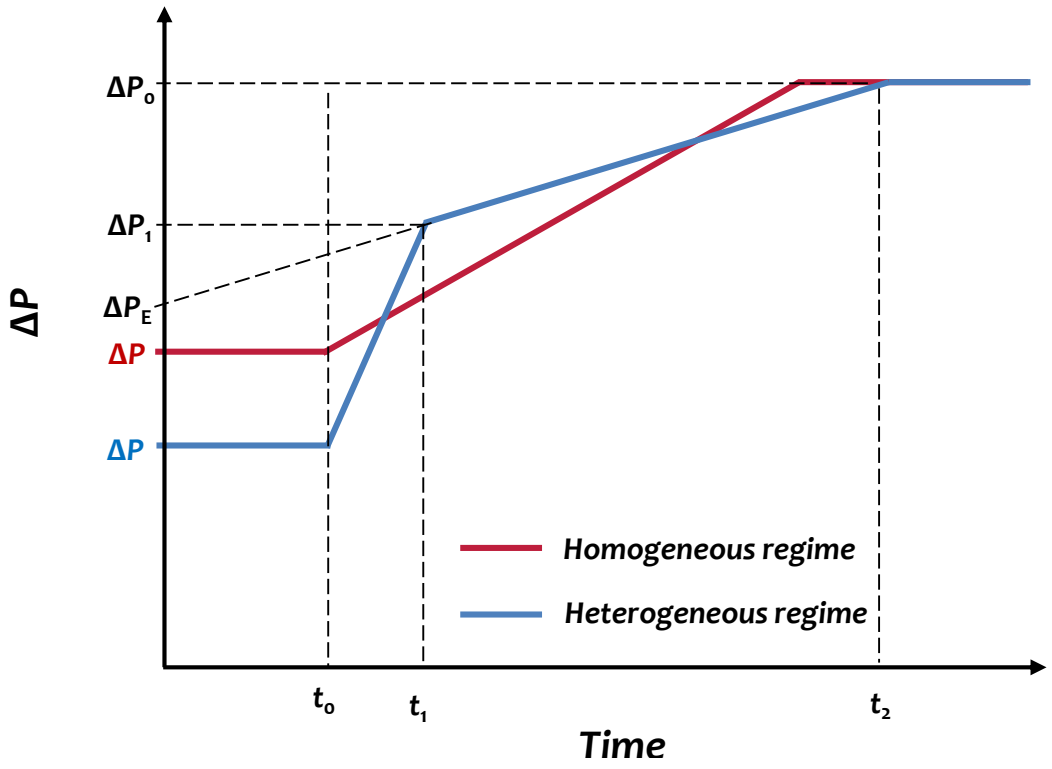

Figure 16: Simplified representation of the dynamic gas disengagement.

Grund and Schumpe (1986) used successfully the gas disengagement technique to extract information on the gas hold-up structure in bubble columns. They recommended its use for the two bubbles classes modelling of the heterogeneous flow regime and highlighted some limits of the method. Based on the slopes observed in the heterogeneous regime (as shown on Figure 16), Jordan et al. (2003) proposed the following equations to improve the estimation of the large and small bubbles proportion in the swarm.

$$\varepsilon_{G,large} = \frac{\frac{\Delta h}{t_1}\frac{\Delta P_1 - \Delta P}{\Delta P} - \frac{\Delta h}{t_2}\frac{\Delta P_0 - \Delta P}{\Delta P_E}}{\frac{\Delta h}{t_1}\frac{\Delta P_1}{\Delta P} - \frac{\Delta h}{t_2}\frac{\Delta P_0}{\Delta P_E}} \quad (7)$$

$$\varepsilon_{G,small} = \frac{\frac{\Delta h}{t_1}\ \frac{\Delta P_0 - \Delta P_1}{\Delta P_0}}{\frac{\Delta h}{t_1}\ \frac{\Delta P_1}{\Delta P} - \frac{\Delta h}{t_2}\ \frac{\Delta P_0}{\Delta P_E}} \quad (8)$$

Knowing that the homogeneous regime is characterised by the presence of a sole bubble class, the appearance of a second bubble class could mark its end and the beginning of the transition. However, DGD can hardly be applied in industry. More promising is the analysis of pressure fluctuation during continuous operation.

2.3.2 Pressure fluctuation analysis

The flow regime identification based on the analysis of the pressure fluctuation data started in the 70s. It consists in recording the variation of the local absolute pressure or the differential pressure in an operating BC. The collected data are then processed by different methods which can be classified into statistical, stochastic, chaos and spectral analysis.

a. Statistical analysis

The statistical analyses are based on the evolution of statistical parameters as a function of u_G. The Probability Density Function (PDF) has been used first. It is defined as the cumulative function of the probability of appearance of the discrete pressure values in a defined dataset. Its sum is unity. It generally depicts peaks which show the tendency of the signal to fluctuate around particular pressure values. The number and proportion of the peaks depicted can then be correlated to the prevailing flow regime. A pronounced peak is characteristic of the homogeneous regime; the slug and heterogeneous flow

regime are both characterised by a bimodal curve possessing a high and a small peak, but with an inverted tendency (Tutu, 1982).

Shaban and Tavoularis (2014) led a similar study for the different prevailing flow regimes. They confirmed the tendency reported by Tutu (1984), but reported the possibility to observe a single peak in the slug flow regime. They showed for the first time a three dimensional PDF graph as shown on Figure 17. Despite the trends differences related to the flow regimes, an accurate identification of the transition is impossible. This lack of accuracy of the PDF led to the investigation of its different moments.

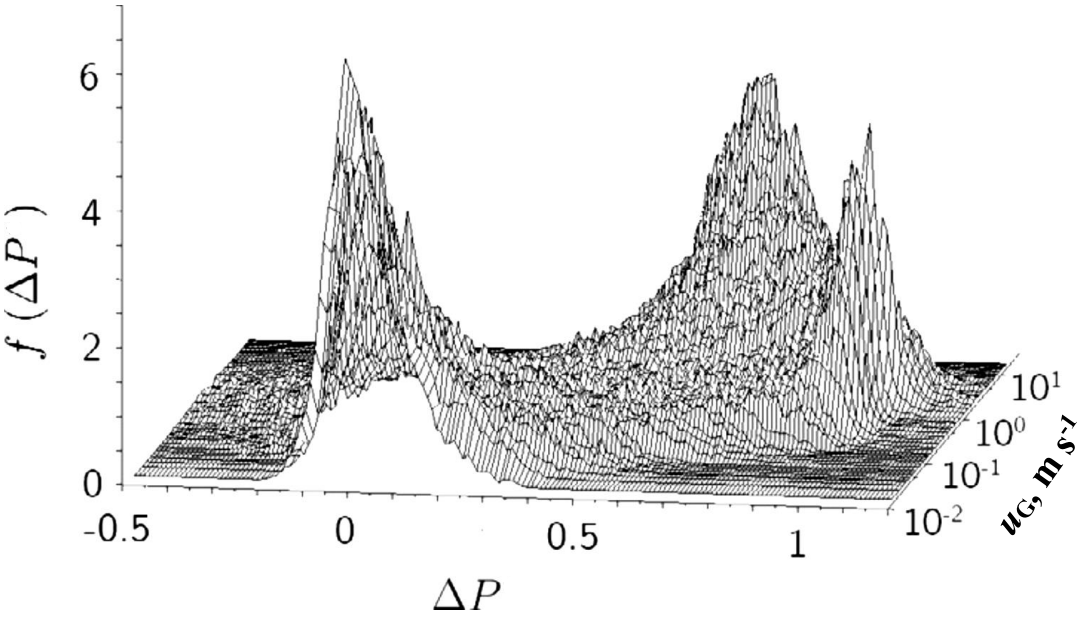

Figure 17: Probability density function (Shaban and Tavoularis, 2014).

The standard deviation (σ), also called second moment of the PDF, measures the dispersion of a set of N data values around its mean value $\bar{P}$. It is defined as:

$$\sigma = \sqrt{\frac{1}{N-1} \times \left(\sum_{i=1}^{N} (Pi - \bar{P})^2 \right)} \tag{9}$$

The evolution of σ as function of u_G gives very low values in the homogeneous regime and increases progressively with u_G. Because of this general trend, Drahoš et al. (1991) reported a linear dependence of σ on u_G and linked it to the linearity existing between u_G and the rate of energy dissipation per unit mass in the bubble column. Vial et al. (2001) proposed the term $\sigma/\overline{P} = 1.5$ for the end of the homogeneous regime; unfortunately, the value depends strongly on the experimental conditions. Although some authors like Gourich et al. (2006) reported the successful use of σ for the identification of the flow regime boundary in BCs, no sharp transition based on this method can be clearly defined. This fact was pointed out by Letzel et al. (1997) and Lin et al. (1999). These authors emphasised the inaccuracy of the method by calling the transition a "point/zone". Recently Nedeltchev and Shaikh (2013) used as an alternative the average absolute deviation which gives the same trend but with higher values than σ. Figure 18 shows two representative graphs of σ as a function of u_G. Except for the case of the single nozzle orifice, the trends are similar, with different absolute values related to the specific operational conditions.

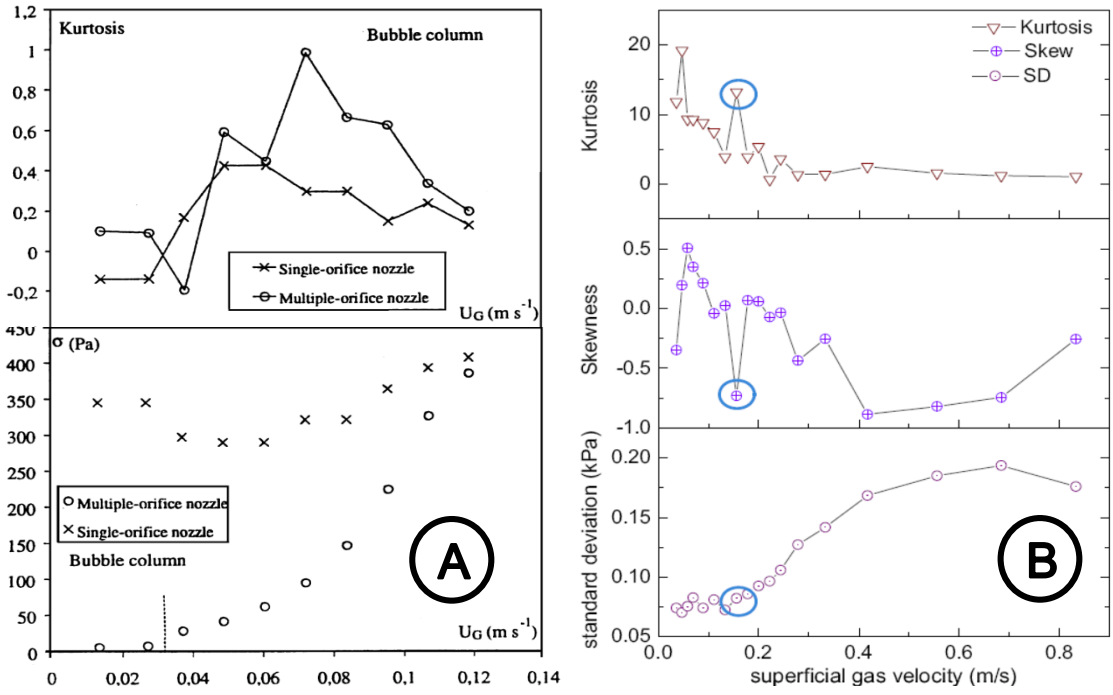

Figure 18: Standard deviation, skewness and kurtosis as a function of the superficial gas velocity (A) Vial et al. (2000) and (B) Li et al. (2013).

The skewness (γ) and the kurtosis (κ), also called third and fourth moment of the PDF distribution, respectively, were used by several authors. They measure the symmetry and the peaked (or flatted) behaviour of a distribution. They are defined as:

$$\gamma = \frac{1}{(N-1)} \times \frac{1}{\sigma^3} \sum_{i=1}^{N} |P_i - \bar{P}|^3 \tag{10}$$

$$\kappa = \frac{1}{(N-1)} \times \frac{1}{\sigma^4} \sum_{i=1}^{N} |P_i - \bar{P}|^4 \tag{11}$$

γ and κ are less robust in comparison with lower moments of the PDF. They also require a larger amount of precise data so that the results can be considered as relevant (Vial et al., 2000). Although some authors claimed to have successfully used these invariants, their results do never depict similar trends. Moreover, their transition criteria are all different. While Vial et al. (2000) and Waheed et al. (2007) found no significant dependence of γ on the flow pattern, Barghi et al. (2004) reported the intersection of two straight lines and Li et al. (2013) a sharp peak. Concerning κ, Vial et al. (2000) and Waheed et al. (2007) reported a pronounced maximum as transition criterion whereas Barghi et al. (2004) reported a change of slope and Li et al. (2013) once more a singular pronounced peak. Figure 18 is an illustrative sample of the incongruity mentioned.

b. Fractal analysis

The fractal or stochastic analysis described here derives from the work of Harold Edwin Hurst (1880-1978), a British hydrologist. In his quest of predicting the long-term storage capacity of reservoirs for irrigation plan purposes, he analysed the long time (over 100 years) discharge stream dataset of the Great Lakes of the Nile River Basin. The method proposed by Hurst (1852), the rescaled range$\left(\frac{R}{S}\right)$, consisted in characterising a whole dataset by the comparison of the cumulated fluctuation of the signal around its mean value

to its dispersion around this mean value. He further led the analysis to shorter segments of the dataset, which he correlated to the time lag τ. Then Hurst proved $\frac{R}{S}$ to depend on the time lag τ between two events. The Hurst exponent (*H*) which expresses the roughness or smoothness level of a signal is calculated from the expression:

$$\left(\frac{R}{S}\right)_{\tau} = \tau^{H} \tag{12}$$

The detailed method is well explained by Franca et al. (1991), Drahoš et al. (1992), Briens et al. (1997), Vial et al. (2000) and Li et al. (2013). *H* is the slope of the log-log plot of $\left(\frac{R}{S}\right)_{\tau}$ to *τ*. The value of *H* is a real number in the interval [0, 1] characterising the process studied:

- If $H > 0.5$ we are in presence of a persistent process. Such processes have a "long-term memory" meaning that in their further evolution, they tend to conserve their previous tendency, increasing or decreasing.
- If $H < 0.5$ we are in presence of an anti-persistent process. Such processes have a "short term memory" meaning that in their further evolution, they tend to depict reverses.
- If $H = 0.5$ we are in presence of a random process. No prediction can be done for such processes.

The fractal analysis allows the determination of slow and rapid stochastic phenomena that are cyclic, but not necessarily periodic (Gourich et al., 2006). Since the Hurst exponent is based on the self-similarity principle as the fractal theory, the method was renamed fractal analysis, deducting the fractal dimension (d_F) from the Hurst exponent (*H*) through the simple following expression:

$$d_{\mathrm{F}} = 2 - H \tag{13}$$

In analogy with studies carried out on fluidized beds, Drahoš et al. (1996) used this method for the first time on BCs. Vial et al. (2000) conclude that, although it could provide interesting qualitative information, it was limited for the accurate identification of flow regimes in a BC. The homogeneous regime seemed to present a pronounced persistent character, whereas an anti-persistent character could be observed only in the fully developed heterogeneous flow. No clear transition could be identified. Zhang et al. (2009) emphasized the discrepancy of results between the works of Vial et al. (2000) and Camarasa et al. (2001) who, despite similar experimental conditions, found a maximum at the transition point and different trends.

Especially they reported a faster increase of H in the homogeneous than in the heterogeneous regime. Gourich et al. (2006) reported that the systems were slightly persistent in the homogeneous regime whereas in the heterogeneous regime the system was characterised as a positively correlated process. They also noticed a discrepancy between the results obtained by Vial et al (2000) and Drahoš et al. (1992) which they attributed to different experimental conditions. The transition is said to appear at a sudden high increase of H (Gourich et al., 2006). More recently, Li et al. (2013) reported also a high increase of H in the homogeneous regime and identified a maximum as the transition point which was not in agreement with the other methods they used. They also reported persistence for the whole range. Figure 19 illustrates a sample of the discrepancies previously mentioned. It shows the results for water/air system reported by Gourich et al. (2006) and Li et al. (2013).

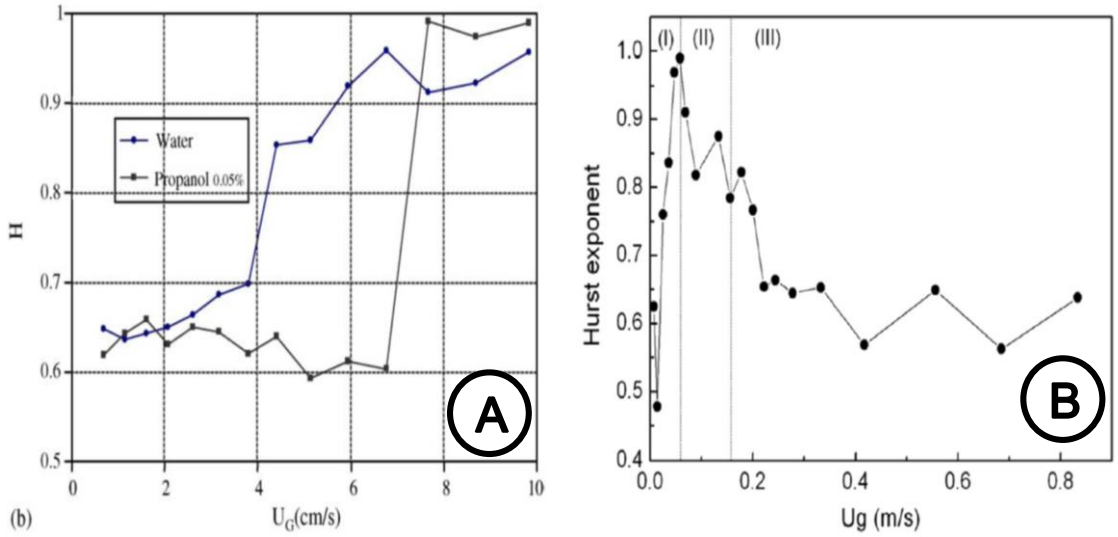

Figure 19: Hurst exponent as a function of the superficial gas velocity, (A) Gourich et al. (2006) and (B) Li et al. (2013).

c. Chaos analysis

Letzel et al. (1997) defined a chaotic system as a non-linear, deterministic system that exhibits a great sensitivity to small variations in initial conditions. The Chaos analysis studies dynamic systems aiming at their characterization and prediction. Several chaos parameters are used in the literature. These are the Lyapunov exponent, the correlation dimension, the Kolmogorov entropy (K_E) and the information entropy (I_E). Since the two first invariants were proven to be similar to or particular cases of the Kolmogorov entropy, this study is restricted to K_E and I_E.

- **The Kolmogorov entropy**

Andrey Kolmogorov (1902-1987) developed the entropy as a quantitative measure of the rate of information loss of system dynamics. It was initially expressed as:

$$K_E = -\lim_{\tau\to 0}\lim_{\epsilon\to 0}\lim_{d\to\infty}\frac{1}{d\tau}\sum_{i=1}^{d} p(i_1,\dots,i_d)\times ln\, p(i_1,\dots,i_d) \quad (14)$$

Where τ is the interval of time during which the state of the system is measured, ϵ is a defined space, d the total number of defined spaces and $p(i_1, i_2,\ldots,i_d)$ the joint probability to find the reconstructed attractor in their corresponding predefined spaces. The value of K_E characterises the system:

- If K_E is infinite, we are in presence of a random system
- If $K_E = 0$, we are in presence of an ordered system
- If $K_E > 0$, we are in presence of a chaotic deterministic system.

Schouten et al. (1994) have developed an algorithm to quantify K_E for time series data, such as those recorded in laboratories for natural phenomena. The method is well explained by Letzel et al. (1997) and Nedeltchev et al. (2003).

K_E has often been recommended for the flow regime identification as giving a sharp transition between the homogeneous and heterogeneous regimes. Letzel et al (1999) could successfully use K_E for data collected in a BC operated at high pressure. But once more, an unexplained discrepancy can be pointed out between the studies of Letzel et al. (1997, 1999) and those of Nedelthev et al. (2007) who all used the algorithm proposed by Schouten et al. (1994). As depicted on Figure 20, Letzel et al. (1997) identified a single pronounced minimum as the transition point whereas Nedeltchev et al. (2007) reported a series of maxima marking the boundaries between several sub-flow regimes. From this remark arises the issue of the transition criteria or generally the interpretation of the results.

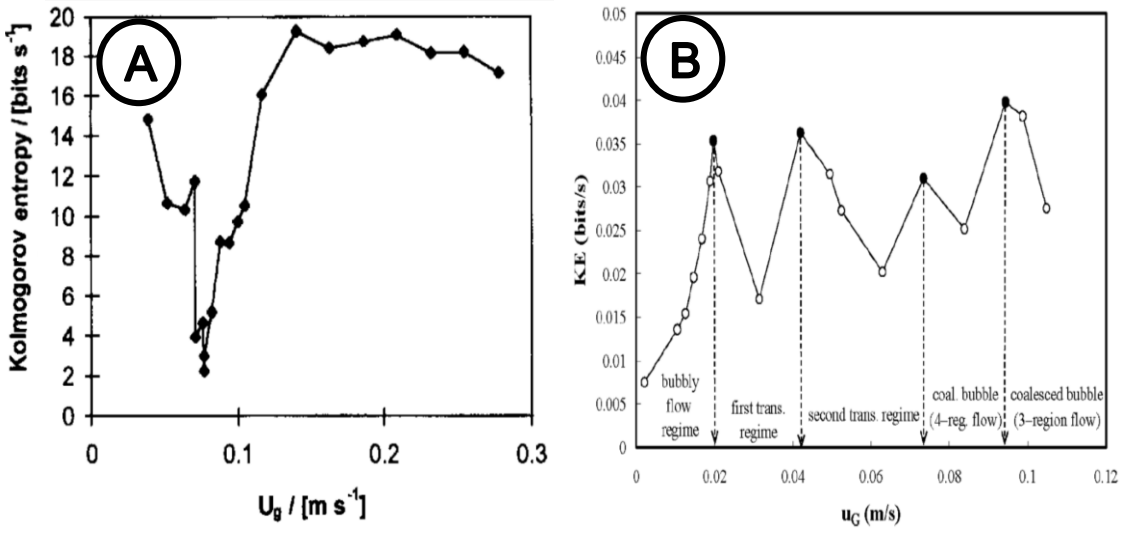

Figure 20: K_E as a function of the superficial gas velocity (A) Letzel et al. (1997) and (B) Nedeltchev et al. (2007).

- **The information entropy**

The information entropy corresponds to the amount of information contained in or given by a dataset. It is expressed as:

$$-I_E = \sum_{i=1}^{n} p_i \log_2 p_i \tag{15}$$

The maximum information entropy is expressed as:

$$-I_{E,max} = p_{max} \log_2 p_{max} \tag{16}$$

Up to now, it has only be used by Nedeltchev and Shakh (2013) for the pressure fluctuation analysis on a BC. Figure 21 shows the results obtained for the total information entropy and the maximum information entropy.

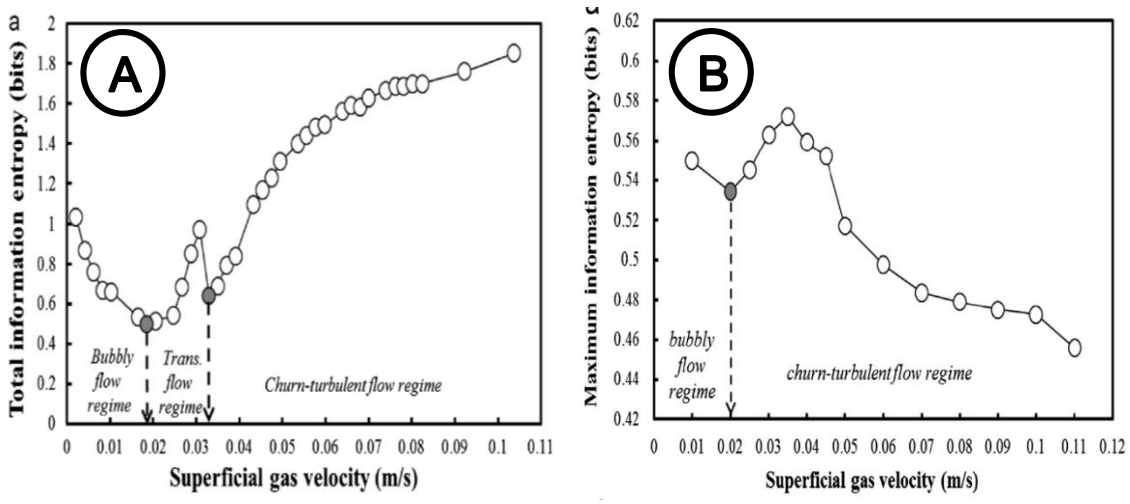

Figure 21: (A) Total information entropy and (B) maximum information entropy as a function of the superficial gas velocity (Nedeltchev and Shaikh, 2013).

Nedeltchev and Shaikh (2013) reported two I_E minima to mark the boundaries of the identified flow regimes for the analysis of the total information entropy. The maximum information entropy seemed to give less information.

d. Spectral analysis

The spectral analysis derives from the work of the French scientist Jean Baptist Joseph Fourier (1760 – 1830), whose proposed thesis in 1807 was firstly subject of controversy. In his heat transfer study, Fourier stated that any continuous periodic function could be expressed as the sum of specific elementary sine functions. The Fourier transform nowadays plays a key role for the signal processing and is widely used in various fields of science and technology. It allows transposing signals expressed in the time domain into the frequency domain. Such signals are usually acquired from natural phenomena. The obtained results lead to the identification of the main frequencies contained in the initial signal, or simply reveal the information it carries. That study opened a wide door to the discretisation of phenomena taking place at the same time, which cannot be separately recorded at their source. The Fourier transform is expressed as:

$$\mathcal{F}_x(f) = \frac{1}{T}\int_0^T P_x(t)e^{-2\pi i f t}\,dt \tag{17}$$

Additionally to the information brought by the Fourier transform, the power spectral density (PSD) was developed to express the contribution of each elementary sine function to the whole signal. This is done thanks the discrete integration of these sine functions, traducing then the power carried by the signal per unit of frequency. The PSD is expressed as:

$$\Phi = \frac{1}{T}E\,(\mathcal{F}\cdot\mathcal{F}^*) \tag{18}$$

Conversely to the other analysis methods, the PSD has in fact not yet successfully been used for flow regime identification. The efforts made by the researchers have mostly brought some hypotheses concerning the identification of the frequency of the elementary sine function and the pressure sources they correspond to.

Table 2 summarises the different sources of pressure fluctuations proposed up to now and the corresponding frequencies. Drahoš et al. (1991) reported that the homogeneous regime was dominated by very low frequencies of the order of 10^{-2} s^{-1}. The heterogeneous regime was dominated by frequencies of the order of 3 s^{-1} or higher. They correlated the broad peak in the frequency range 2 – 7 s^{-1} to the formation of large aggregates of bubbles since its amplitude decreased as the pressure probe was receded from the gas distributor.

Table 2: Summary of the pressure sources and their corresponding frequencies reported in the literature

Pressure sources			Specific frequencies attributed, s^{-1}				
			Drahoš et al. (1991)	Letzel et al. (1997)	Vial et al. (2000)	Chilekar (2007)	Gourich et al. (2006)
Bubble dynamics	Formation		**2 – 7**		**15 - 20**	**2 - 3**	
	Passage			**1 – 10**	**3 - 5**	**10 - 15**	
	Coalescence						
	Break-up						
	Eruption		**not at all considered**				
Eddies	Large-scale		**0.1**	**0.1**	**3 - 5**		
	Med./small-scale		**1.5 - 2.5**				
Liquid level fluctuations			**0.01**	**≤ 0.1**	**0.1**		**0.1**

In agreement with the results of Drahoš et al. (1991), Letzel et al. (1997) attributed the frequencies in the range 1-10 Hz to the large bubbles dynamics (without specifying exactly what they understand under this term). They assumed that high frequencies were irrelevant in the study of bubbles behaviour. They then filtered the raw data, eliminating from the signal the effects due to frequencies higher than 20 s^{-1}. Figure 22 illustrates such a signal filtering carried out by Li-shun et al. (2009).

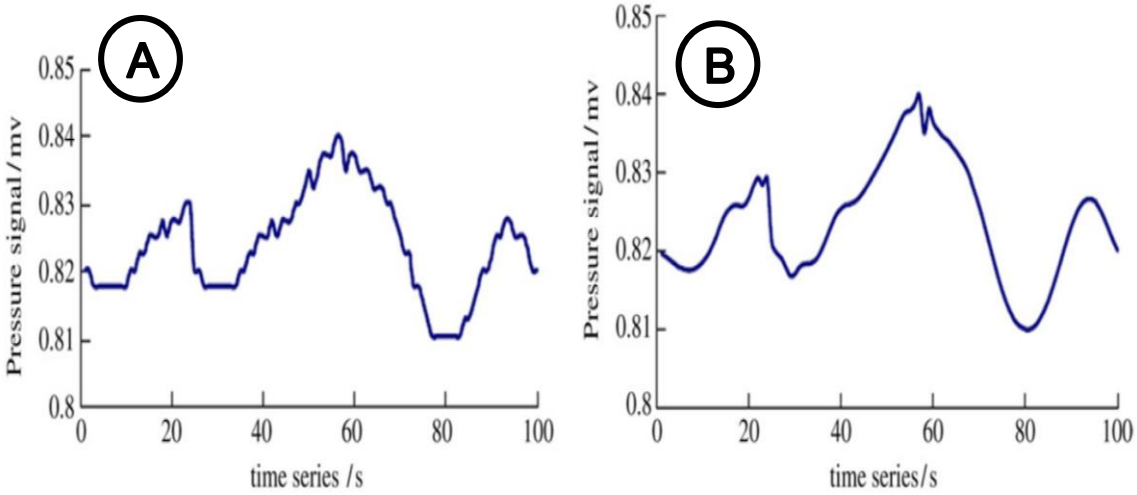

Figure 22: Comparison between (A) original pressure signal and (B) pre-treated signal (Li-shun et al., 2009).

Using a single orifice nozzle, Vial et al. (2000) found what they called "noisy" PSD functions which they explained as the consequence of the non-uniform gas distribution. They reported the presence of peaks in the range of 15 – 20 s^{-1} which they suggested to be probably due to the bubble formation process. They reported the total absence of this peak in the riser of airlift reactors.

Similarly Chilekar (2007) observed a singular peak at about 3 s^{-1}. He attributed that peak to the bubbles formation. At the opposite of the other researchers whose peaks are systematic at all velocities, he observed singular peaks in the range 10-15 s^{-1} and also 20-25 s^{-1} for specific velocities. He attributed the first one to the fast rising large bubbles and did not comment the second one at all.

Finally, Gourich et al. (2006) found a unique peak at frequencies lower than 10 $^{-1}$ s^{-1}, which they attributed to the surface level fluctuation (in agreement with the former works). Frequencies higher than 20 s^{-1} are globally considered as uninteresting or attributed to noise. On the other hand, Veldhuis et al. (2008) in their elementary analysis on the shape oscillation of bubbles proved to have measured the bubbles' vibration in a frequency range up to 100 s^{-1}.

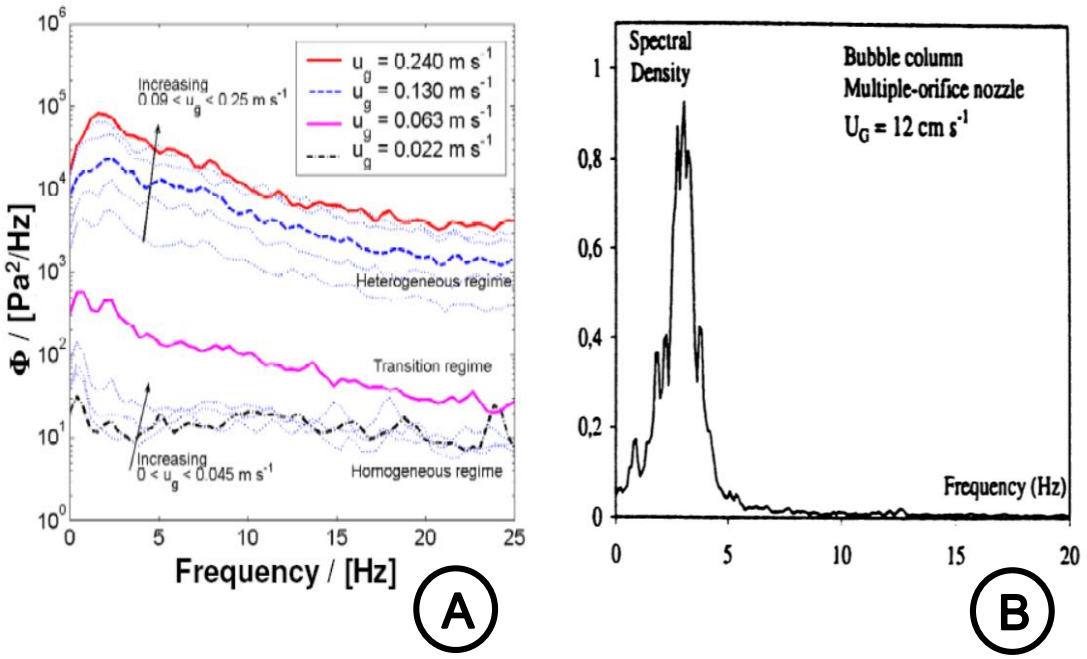

Figure 23: Power spectral density as a function the superficial gas velocity (A) for water/nitrogen (Chilekar, 2007) and (B) for water/air (Vial et al., 2000).

Except for Chilekar (2007), no systematic PSD as a function of the superficial gas velocity is reported (Figure 23). At the difference of the other researchers, their diagram does allow an easy identification of the specific frequencies. The literature studies agree in relating the lowest frequencies (≤ 0.1 s^{-1}) to liquid level fluctuations. The discrepancies with respect to the other frequencies are obvious (Table 2).

2.4 Parameters influencing the flow regime in a bubble column and its identification

Many factors influence the flow regimes in bubble columns and their identification:

- Factors related to the equipment: sparger type and geometry, column dimension, axial and/or radial sensor location.
- Factors related to the system used: viscosity, surface tension and gas and liquid density.

- Factors related to the operating conditions: operating pressure, temperature and clear liquid height.

Among these, our investigation is oriented on the following important factors:

2.4.1 The sensors axial location (*h*)

The sensor axial location (*h*) is referred to the distance between the sparger and the pressure sensor. Drahoš et al. (1991) reported that, depending on the type of sparger, *h* had almost no influence on the standard deviation in the homogeneous and transition regimes but in the turbulent regime this effect was more pronounced. Using the PSD analysis, he also reported that pressure sensors located in the lower half of the column allowed a better regime identification. Letzel et al. (1997) reported that the proximity of the sensor to the gas distributor led to the impossibility to identify a transition.

Deckwer (1992) reported that the heterogeneous regime takes firstly place at higher axial position. It means that for the same operating conditions, a difference in sensors axial location would lead to different results.

2.4.2 The clear liquid height (h_0)

The clear (static, un-aerated, un-gassed) liquid height (h_0) is the height liquid when no gas is being injected into the column. Drahoš et al. (1991) reported that h_0 has no influence on the formation and passage of the bubbles in the homogeneous and transition regime. According to them, this effect is small on the coalescence and the recirculation in the transition regime. But in the heterogeneous regime there is a relatively steep increase of the standard deviation with h_0.

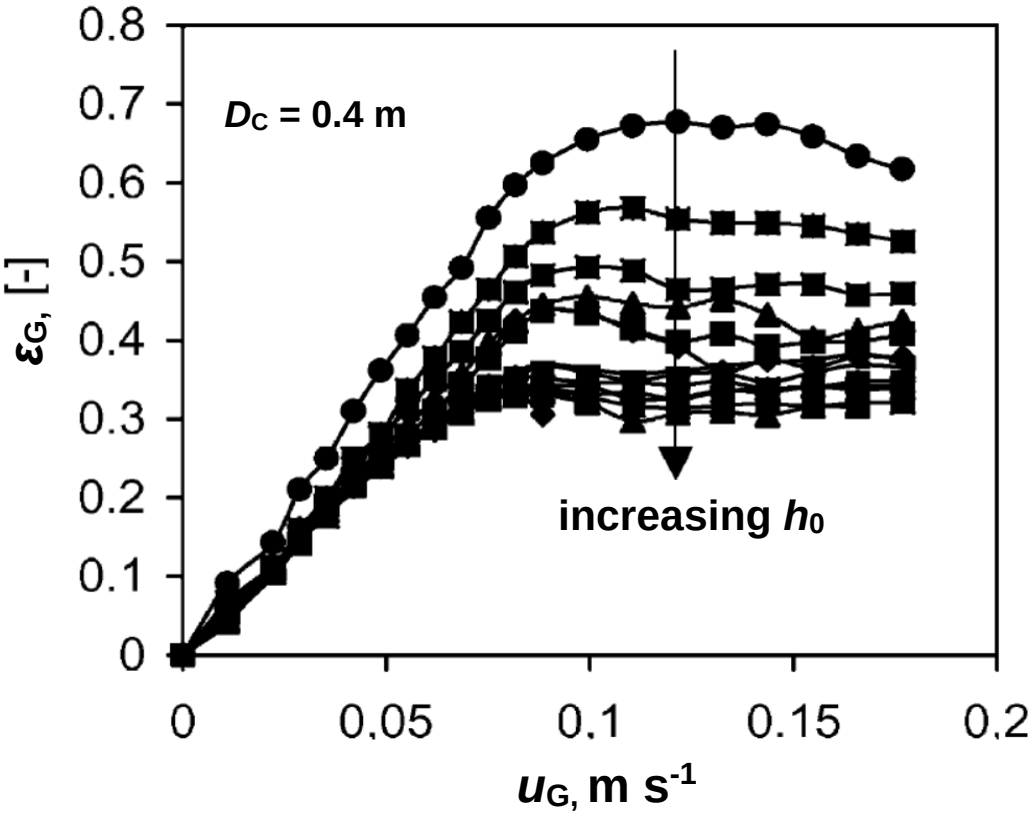

Figure 24: Influence of the clear liquid height h_0 (from 0.1 m to 1.5 m) on the voidage (Ruzicka et al., 2001).

Ruzicka et al. (2001) investigated the influence of the clear liquid height on the stability of flow regimes. Contrary to the previous researchers, they reported that the increase of h_0 destabilizes the homogeneous regime to smaller u_G values. Figure 24 shows the primary data of Ruzicka et al. (2001) on the influence of the clear liquid height on the gas hold-up. A clear decrease of the voidage with the clear liquid height is observed.

2.4.3 The liquid viscosity (μ)

The influence of the variation of the liquid viscosity on the flow regime is usually studied either using liquids with different viscosities, e.g., ethylene glycol with different dilution degree. Carboxymethyl cellulose (CMC), a water soluble salt widely used in laboratories and industries, is another viscosity-increasing agent. CMC-solutions are slightly

pseudoplastic. The bubbles flow causes a shear stress which, depending on the flow behaviour index influences the viscosity. It is already well-established that the increase of viscosity shifts the first transition point to lower u_G values.

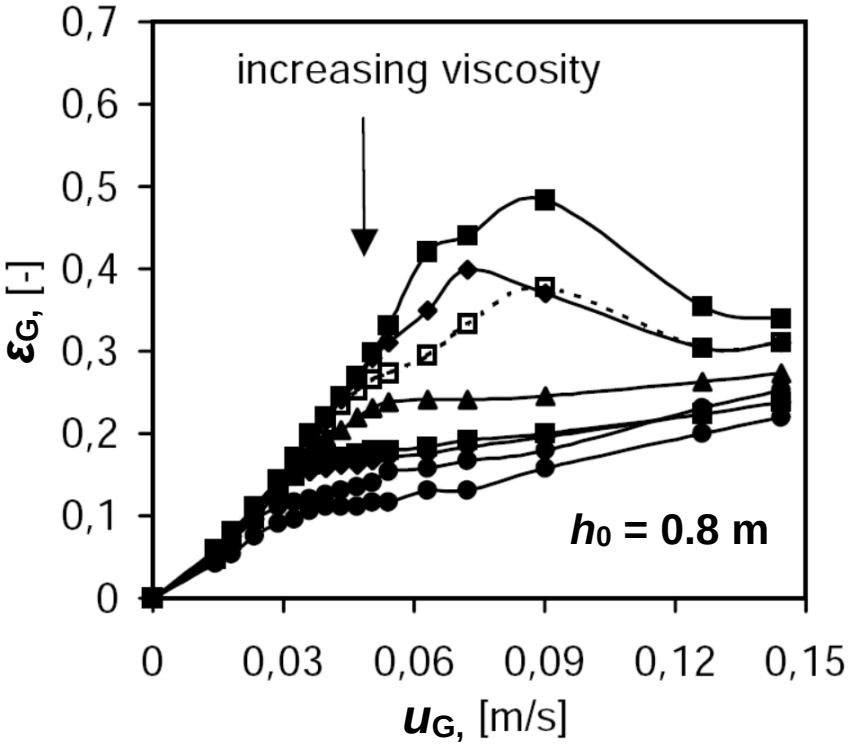

Figure 25: Influence of the viscosity on the flow transition (Ruzicka et al., 2003).

Figure 25 (Ruzicka et al., 2003) shows that the change in slope of the gas hold-up vs. u_G curves is shifted to lower gas velocity as the viscosity increases. This is due to the fact that the bubble size increases with the viscosity.

2.4.4 The operating pressure (*P*)

Some important chemical reactions such as the chlorination and oxidation are carried out under high pressure conditions in bubble columns. Therefore, the influence of the operating pressure on the hydrodynamics in a BC is relevant. LaNauze and Harris (1974) confirmed that the increase of the operating pressure leads to the formation of smaller

bubbles. They attributed it to the increased momentum of the gas during the bubbles formation process which in turn increases the frequency of bubble release. The reduction of the bubble size due to the increase of the pressure leads to the increase of the total gas hold-up as widely reported in the literature.

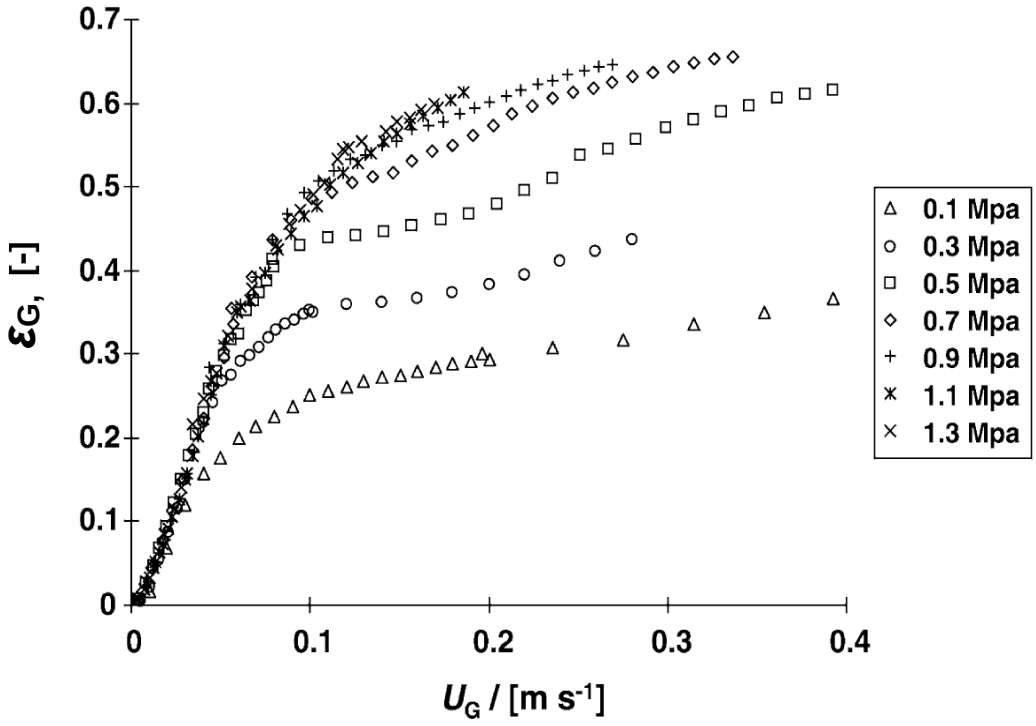

Figure 26: Gas hold-up as a function of the superficial gas velocity, water/nitrogen at different operating pressures (Letzel et al., 1999).

Figure 26 shows an example of the influence of the operating pressure on the gas hold-up. As also reported by Luo et al. (1999), the increase of the operating pressure shifts the homogeneous regime (end of the initial strait line) to higher u_G values.

2.5 Prediction equations

Equation (19) is one of the simplest and oldest models developed for gas hold-up prediction. The coefficients α and β depend on the system involved and the sparger type. β varies between 0.7 and 1.0 in the homogeneous, and between 0.4 and 0.7 in the heterogeneous regime (Deckwer, 1992).

$$\varepsilon_G = \alpha\, {u_\mathrm{G}}^{\beta} \tag{19}$$

Due to the trend difference between homogeneous (linear) and heterogeneous regime (nonlinear), equation 19 does not perfectly fit the evolution of the gas hold-up as a function of the superficial gas velocity in the whole range. This complexity led to the development of a multitude of models. Some of those correlations predict separately the two previously mentioned flow regimes whereas others, the evolution of the gas hold-up for both flow regimes. The incompatibility of the developed models with one another and their non-applicability to changing operating conditions has well been pointed out by some authors. Hristov (2009) emphasised this fact and related it to the "blind approach" of the Bingham π-theorem.

The prediction of the gas hold-up based on the operating conditions has also been the interest of many authors. For the pressure effect, Reilly et al. (1994) proposed the following relation for $\varepsilon_{G,crit}$, the critical gas hold-up value at the transition between homogeneous and heterogeneous regime.

$$\varepsilon_{G,crit}\ \alpha\ {\rho_\mathrm{G}}^{0.04} \tag{20}$$

2.6 Motivation

Table 3 summarizes the up to now major studies carried out on the flow regime identification based on visual observation (photography), gas hold-up and analysis of the pressure fluctuations. It presents chronically the different analysis methods used. From the previous literature review, relevant discrepancies and lacks can be emphasized:

- For comparable experimental conditions and identical analysis methods, the results reported in the literature present unexplainable divergencies. Except the gas-hold up and the standard deviation, the other analysis methods usually depict different trends. Different criteria for boundaries identification are used by the researchers. A clear understanding of the methods limits, the criteria for boundary identification and the reason for the divergences is still missing.

- Although the Fourier transform is a powerful tool, its use (the PSD analysis) is more limited to suppositions which unfortunately do seldom match with one another. The point the authors have in common is in contradiction with the results given by the elementary analysis of single bubble flow. While many authors who dealt with the flow regime identification consider frequencies above 20 s^{-1} to be either not relevant or belonging to a noise effect, Veldhuis et al. (2008) proved the bubbles oscillation to belong to that range. Moreover, the PSD analysis has seldom been studied as a function of the gas velocity, and is thus not considered as a flow regime identification method.

- Despite its inaccuracy, the gas hold-up is still used for the set-up of prediction equations. The Kolmogorov entropy (which seems to be the most accurate analysis method) is still seldom used. The computation time and its complexity seem to remain major hindrances.

- Most of the studies on the comparison between the analyses methods were carried out at atmospheric conditions with the system water/air. Although comparative analyses on the flow regime identification have already been done, a systematic study of the existing methods is still missing.

Table 3: Summary of some important flow regime identification analyses.

Year	Authors	Bibliography	Photography / visual	Gas hold-up	Drift flux	Gas disengagement	Probability Density Funct.	Standard deviation	Skewness / Kurtosis	Average cycle Time	Kolmogorov entropy	Lyapunov exponent	Correlation dimension	Mutual information	Information entropy	Fractal dim. / Hurst exp.	Power Spectral Density	Coherence	Other methods
2013	Li et al.		■					■	■							■			■
2013	Nedeltchev & Shaikh.										■				■				
2010	Chilekar et al.			■														■	
2010	Zhang et al.									■			■						■
2009	Zhang et al.																■	■	
2009	Zhang and Li			■												■	■		
2009	Shun et al.											■		■			■		
2007	Nedeltchev et al.			■							■								
2006	Gourich et al.			■	■			■					■			■	■		
2004	Barghi et al.			■	■		■	■	■										
2001	Ruzicka et al.			■															
2001	Vial et al.			■	■												■		
2001	Lin et al.			■								■	■	■					
2000	Vial et al.			■	■			■	■				■			■	■	■	
2000	Kang et al.												■	■					
1997	Letzel et al.		■	■				■			■		■				■	■	
1996	Drahoš et al.															■			
1992	Shnip et al.			■															
1991	Drahoš & Zahradnik			■				■									■	■	■
1991	Franca et al.						■						■			■	■		
1986	Schumpe & Grund					■													
1986	Goishi Matsui			■			■	■	■										
1982	Narinder K. Tutu						■												

3. Material and Methods

3.1 Experimental set-up

Figure 27 shows the experimental set-up used and Figure 28 is a photo. The bubble column is a cylinder made of stainless steel with 0.102 m inner diameter and 2.40 m height. Two windows (one at the front and one at the back) located at 0.84 m from the gas sparger allow a view of the bubbles flow within the column. The windows are parallel and have 0.048 m diameter.

The filling of the column with the liquids and its emptying is achieved with a membrane pump (Model VA 20, VERDERAIR). The pumping direction can be reversed by a system of pipes and manual valves. A faucet directly connected to the top of the column is especially used for fillings with tap water.

The reduction of the liquid evaporation during processes involving solvents is assured by a packed-bed saturator of 0.22 m diameter and 0.65 m height. The saturator is filled with the same liquid and kept at the same temperature as the column.

The operating temperature regulation is assured by a double-wall heat exchanger located at the lower part of the column. The heat exchanger is thermally isolated and connected to a thermostat (Model FP 50, JULABO) operating with an ethylene glycol solution. The temperature sensor of the thermostat (for the temperature regulation) is located at 0.62 m from the sparger. The upper part of the column (not in contact with the heat exchanger) is isolated with glass wool and coated with an aluminium foil.

The operating pressure regulation (from 0 up to 50 bar) is assured by the system made of a pressure sensor (Model 3994, SAMSON), a pressure regulator (Model 3760, SAMSON), an overpressure protection valve (Model 3277, SAMSON) all installed at the top of the column, and a regulator station (Model TROVIS 6412, SAMSOMATIC) at which the set value is adjusted.

A camera (D700, Nikon) is fixed on a tripod before the front window and a flash (SB-910, Nikon) is fixed at the back window. Both are connected with a cable, which allows the simultaneous back lightning photography.

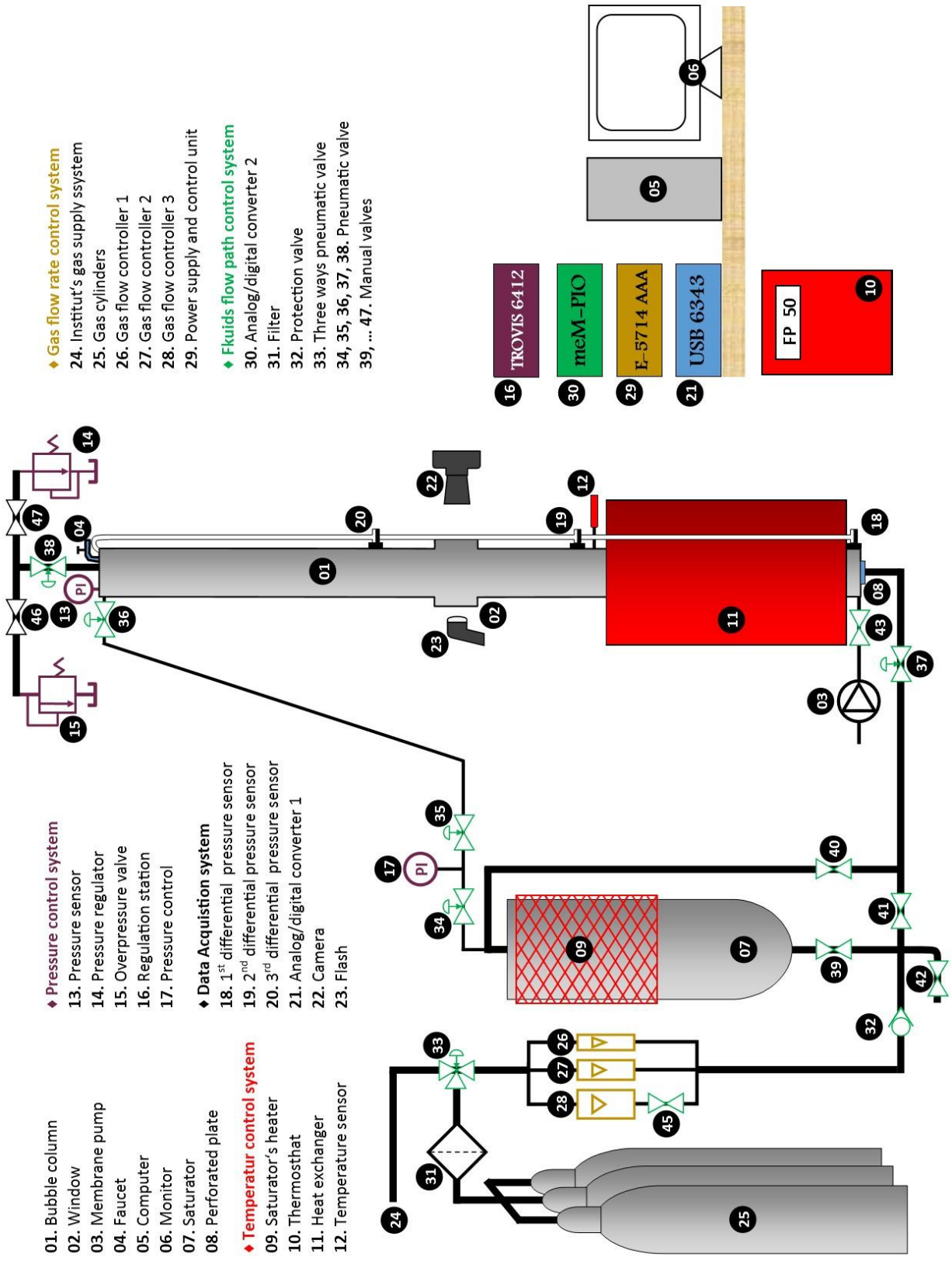

Figure 27: Simplified flow diagram of the experimental set-up.

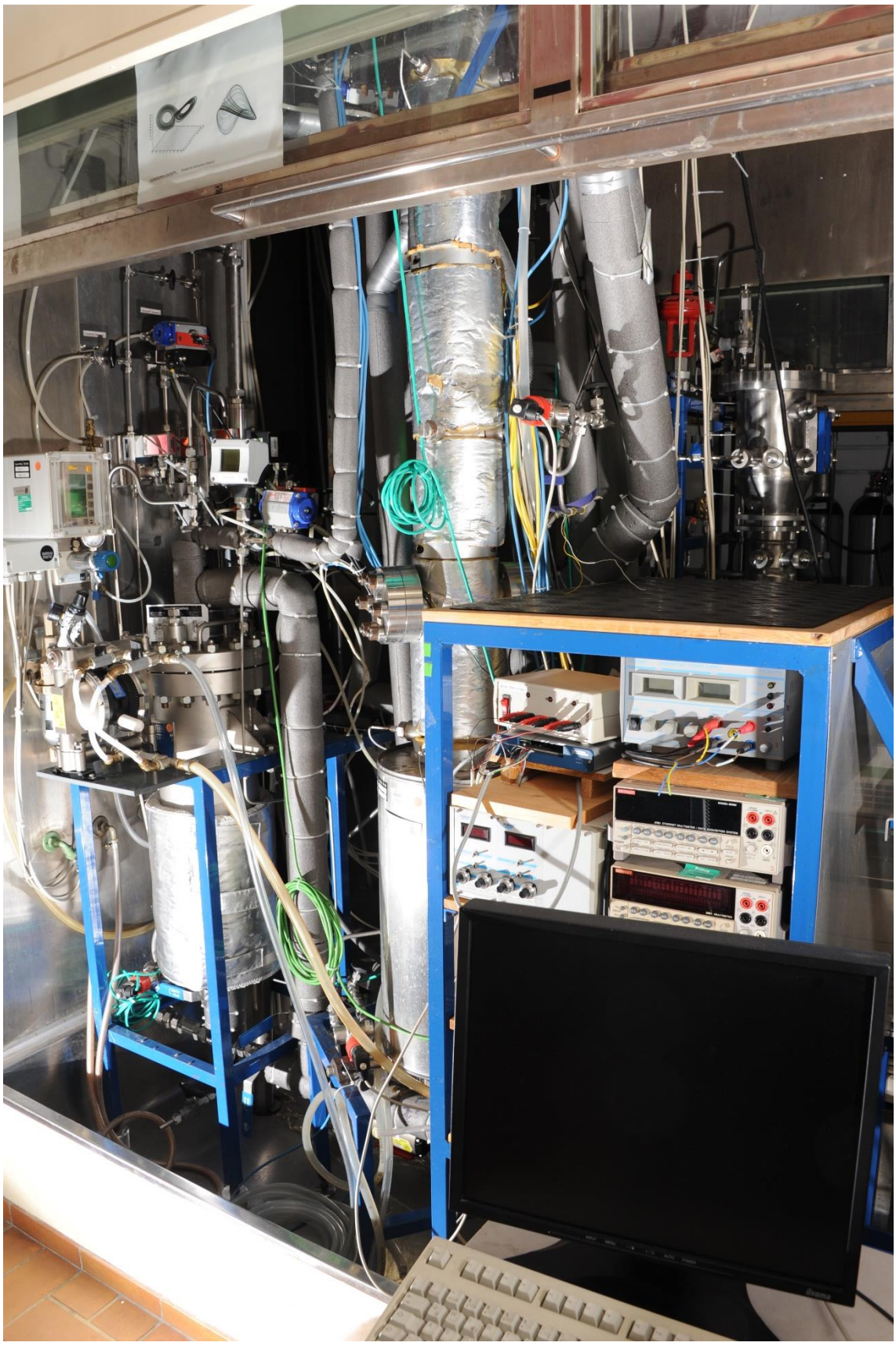

Figure 28: Photo of the experimental set-up used.

The measurement of the differential pressure fluctuations is performed by means of three differential pressure sensors (Model CP 1013, LABOM). Figure 29A shows a photo of the sensor used. Each sensor measures in the range 0 to 1 bar with a precision ≤ 0.5%. It possesses a positive and a negative pole. As depicted on Figure 29B, a pipe (syphon) fixed on the positive (high pressure) pole of the sensor is connected to the column. It is always filled with the liquid being used. The syphon prevents the entry of gas into the pipe during operation. This could influence the signal badly. The release of any gas from this pipe (before the measurements start) can be achieved by manually opening a valve (see Figure 29B).

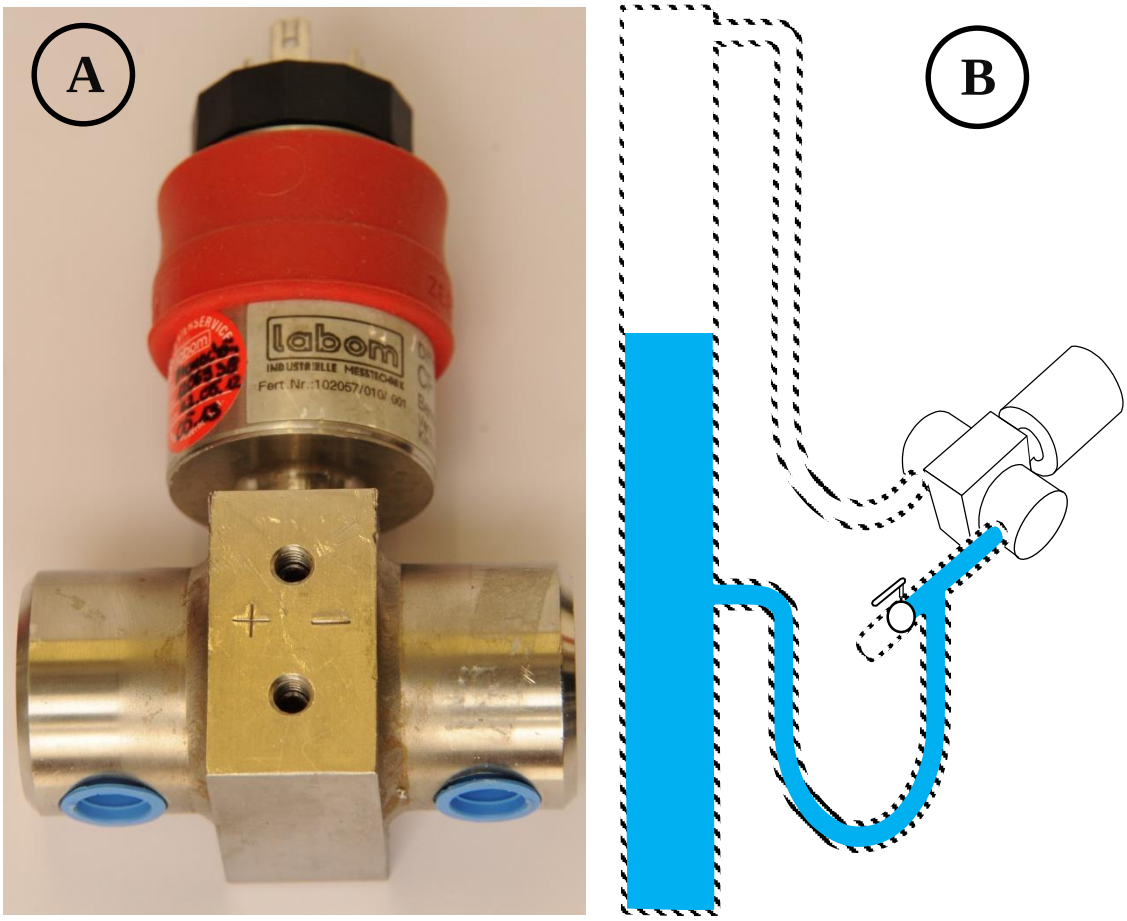

Figure 29: (A) Differential pressure sensor used, (B) Installation of the sensor.

The sensors 1, 2 and 3 are connected at 0, 0.65 and 1.20 m above the gas distributor, respectively. The second pipe fixed at the negative pole is connected to the top of the column. Thus the values given by the sensors are the differential pressures with respect to the top of the column. The sensors (which produce an analog signal of 4 to 20 mA) are

connected to an AD converter (Model USB 6343, NATIONAL INSTRUMENTS) for data acquisition. The sampling rate is 100 s^{-1}.

The gas distribution is performed through a perforated plate located at the bottom of the column. It has a diameter of 0.08 m and thickness of 0.003 m. It is made of stainless steel and has 19 holes of 0.001 m diameter each. Figure 30 shows the holes distribution on the perforated plate used. The distance between two neighbour holes is always 0,016 m.

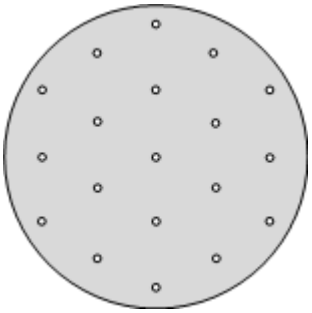

Figure 30: Holes distribution on the perforated plate used.

The gas supply is assured either by the nitrogen supply system of the institute (delivering a pressure up to 7 bar) or by a system of up to six gas bottles connected in parallel (delivering a pressure up to 250 bars). The control of the gas flow rate is assured by three gas flow controllers (Model El-flow and IN-flow, BRONKHORST) powered by a power supply and control unit (Model E-5714 AAA, BRONKHORST), which is regulated by the AD converter USB 6343. These GFC (gas flow controllers) 1, 2 and 3 have 50, 500 and 5000 $NL \times min^{-1}$ nominal capacity. An upstream high pressure filter protects the GFCs from impurities.

The control of the fluids flow path in the pipes of the experimental plant is assured by a system of pneumatic valves (AIR TORQUE) and manual valves (BEE and Parker). The use of the manual valves is not involved during operation whereas the pneumatic ones are mostly used for the instantaneous and automatic changes taking place when the system is running. The pneumatic valves are all connected to an AD converter (Model meM-PIO, BMC MESSSYSTEME) which is connected to the computer.

As depicted on Figure 27, the different control systems previously described are all connected to the computer. Using a virtual simulated plant, the liquid level and the opening and closing of the valves and the pressure difference can be controlled from the monitor. The automatic control of the experimental set-up from the computer is powered by the software LABVIEW, NATIONAL INSTRUMENTS.

3.2 Chemical material

Tables 4 and 5 give some relevant properties of the liquids used.

Table 4: List of the liquids used and their properties at 25°C.

Chemical	Formula	Viscosity mPa s	Surface Tension N m^{-1}	Density Kg m^{-3}
Tap water	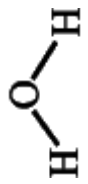	0.894	0.07	1000
Toluene	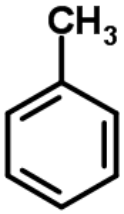	0.550	0.028	866.9
Ethylene glycol		16.1	0.047	1096.7

Table 5: Rheological properties of the carboxymethyl cellulose (CMC, Sigma) solutions.

CMC solution	Flow index (*n*) -	Consistency index (*k*) *mPa* s^n
CMC 0.5 %	**0.85**	**2.5**
CMC 1.0 %	**0.97**	**6.7**
CMC 1.25 %	**0.94**	**3.23**
CMC 2.0 %	**0.96**	**9.4**
CMC 4.0 %	**0.89**	**90**

The rheological characterization was carried out with a concentric cylinder rheometer (RheoStress RS100, HAAKE).

3.3 Methods

3.3.1 Experiments

All experiments were carried out at 298 K with nitrogen as the gas phase.

- **Data acquisition process:**

Figure 31 shows a global view of the steps followed in the experiments:

t_0: Gas injection

t_1: Starting of the data acquisition

t_2: Closing of the valves 37 and 38 and set of the GFC to 0

t_3: End of the data acquisition and opening of the valves 37 and 38

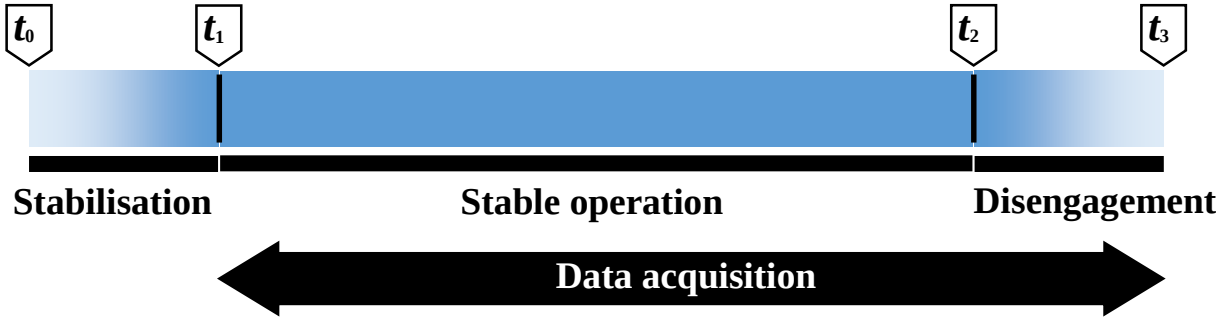

Figure 31: Data acquisition process.

- **The stabilisation phase:** At t_0 the gas is injected into the column containing the quiescent liquid. To avoid an ejection of liquid from the column, the set gas velocity is gradually reached in up to 10 seconds. Before any measurement, a stabilisation phase of two minutes served to bring the system into stable operation.

- **The stable operation phase:** At t_1 the system has reached a stable status. The data acquisition of the differential pressure fluctuations is started. The acquisition frequency was set at 100 s^{-1}. A few minutes after the beginning of data acquisition, the photography is simultaneously carried out for up to 30 s. Photography is performed at a speed of 200 s^{-1}, an aperture of 22 and frequencies up to 6 frames per second. The stable operation phase lasts eleven minutes.

- **The disengagement phase:** At t_2 the gas supply is suddenly stopped by simultaneously closing the valves 37 and 38 while the data acquisition continues. The command of the gas velocity is then set at zero. At t_3, the data acquisition is stopped and then the valves 37 and 38 are opened. The disengagement phase lasts two minutes.

The whole procedure described took place automatically thanks to LabVIEW programs. Three experiments were carried out for each superficial gas velocity. Depending on the operating pressure and the flow rate, the gas supply was achieved from gas bottles or the institute nitrogen supply system through the most adequate GFC of the three previously mentioned. For an operating pressure of 0.1 MPa, the nitrogen supply system of the institute was used. For higher pressures, the gas supply was assured by bottles. Table 4 shows values of u_G for the several operating pressures used and the chosen GFC.

Table 6: Adjustment of the superficial gas velocity depending on the operating conditions.

	GFC 1 Nominal capacity: 50 NL/min		**GFC 2** Nominal capacity: 500 NL/min		**GFC 3** Nominal capacity: 5000 NL/min	
Operating pressure	%	Expected u_G, m s^{-1}	%	Expected u_G, m s^{-1}	%	Expected u_G, m s^{-1}
0.1 MPa	4	0.0038	10	0.0968		
	100	0.0968	25	0.2518		
2.5 MPa	10	0.0042	10	0.0420		
	100	0.0420	60	0.2521		
5.0 MPa			2	0.0043	10	0.2162
			100	0.2162	11	0.2378
10 MPa			4	0.0043	10	0.1097
			100	0.1097	20	0.2194
20 MPa			8	0.0044	10	0.0552
			100	0.0552	38	0.2100
40 MPa					2	0.0055
					80	0.2227

Depending on the liquid phase used, specific operating parameters were varied. These are:

- **Tap Water**

For an operating pressure P = 0.1 MPa, the data acquisition process was performed for each of the following clear liquid heights 0.75, 1.00, 1.25, 1.50, 1.75 and 2.00 m. For the clear liquid height h_0 = 1.50 m, the data acquisition process was performed for the following operating pressures 0.1, 0.25, 0.5, 1.0 and 2.0 MPa.

- **Toluene**

The gas passed the saturator filled with toluene. The aerated phase was set at 7 minutes. For an operating pressure P = 0.1 MPa, the data acquisition process was performed for each of the following clear liquid heights: 1.40, 1.55, 1.70, 1.75 m.

For the clear liquid height h_0 = 1.55 m, the data acquisition process was performed for the following operating pressures: P = 0.1, 0.25, 0.5, 1.0 and 2.0 MPa.

- **Mono ethylene glycol**

For the operating pressure P = 0.1 MPa, the data acquisition process was performed for each of the following clear liquid heights: h_0 = 0.75, 1.00, 1.25, 1.50, 1.75 and 2.00 m.

For the clear liquid height h_0 = 1.50 m, the data acquisition process was performed for the following operating pressures: P = 0.1, 0.25, 0.5, 1.0 and 2.0 MPa.

- **CMC solutions**

For the operating pressure P = 0.1 MPa and the clear liquid height h_0 = 1.50 m the data acquisition process was performed for each for the following CMC solutions: 0.50 %, 1.00 %, 1.25 %, 2.00 % and 4.00 % by weight.

Using a precision balance (Model MJ-3000, YMC CO.LTD), the desired amount of CMC powder was weighed. It was then slowly poured into a 30 l plastic bucket containing the corresponding amount of bi-distilled water. Simultaneously the mixing was performed

with a dispersing instrument (Ultra Turax T50 digital, IKA). The dispersion continued for several hours until the complete dissolution of CMC.

The viscosity of the CMC solutions was checked before and after the experiments.

3.3.2 Data analysis

The pressure data collected were then analysed on the basis of 65000 points (4000 points for toluene). Mean value of three trials was calculated.

The gas hold-up was determined for the lower, the upper and both regions of the column (between the pressure sensors).

The pressure signal processing was carried out by:

- The statistical analysis consisted of the evaluation of the PDF, the skewness, the kurtosis, the standard deviation and the average absolute deviation. Additionally, as a new parameter, the average cycle time is evaluated. The average cycle time is the average duration of a complete cycle or the average time needed for the signal to cross its mean value twice.

$$T_C = \frac{T}{0.5 \times n_c} \tag{21}$$

where T is the length of the time series and n_c is the number of times the signal crossed the mean value.

- The chaos analysis consisted of the evaluation of the information entropy and the Kolmogorov entropy. The Kolmogorov entropy was based on the algorithm developed by Schouten et al. (1999), with the vector dimension set at 50 and the embedding dimension l_o = 3×AAD. The use of an adequate algorithm reduced considerably the computation time, making this method fast (contrary to the reports of other researchers who made a comparative analysis.

- The stochastic analysis consisted of the evaluation of the fractal dimension as a function of the gas velocity. The smallest vector used according to the algorithm of Hurst had a dimension of 1250.

The previously listed analyses are already explained in chapter 2.3. They were performed using macros written in Visual Basic.

- The spectral analysis consisted of the evaluation of the power spectral density as a function of the gas velocity. This was performed with the toolbox "periodogram" of the software MATLAB. The analysis was made on the base of 1024 points (10.24 s).

4. Results and Discussions

4.1 Flow regime identification

4.1.1 Results obtained by the analysis methods

An overview of the results obtained by the several analysis methods used is given. This preliminary analysis does not take into account the influences of the viscosity and the operating pressure. The system and operating conditions selected are water/nitrogen at P = 0.1 MPa and h_0 = 1.50 m. The influence of the sensors axial location is presented whereas the effect of the clear liquid height is mentioned in few cases only. The criteria for the identification of the boundaries between the flow regimes are mainly extrema or clear changes of slope. The initial identification of the main transition point (boundary between homogeneous and heterogeneous flow regime) based on the gas hold-up analysis is marked by a vertical dashed line. The other plausible boundaries (between sub-regimes) are marked on the graphs by vertical dotted lines and discussed later.

a. The gas hold-up analysis

Figure 32 depicts the gas hold-up analysis at atmospheric conditions. The clear liquid height has no influence on the gas hold-up analysis. Depending on the sensors' axial locations, two to three regimes can be identified. The first region is always characterised by a linear increase of ε_G with u_G and is independent of the sensor axial location. The last region, is also characterised by a (nonlinear) increase of ε_G with u_G, but the slope is clearly smaller than the slope in the first region. For high axial location of the sensors (between sensors 2 & 3), a third region separating the two previous ones is noticed. It is characterised by a slight decrease of ε_G with u_G.

These results are in good agreement with those widely reported in the literature. The upper region of the column allows with some approximations the identification of a first and second transition point. The transitions are observed more clearly in the upper part of the column where the coalescence of the bubbles starts (Deckwer, 1992). At the opposite, the overall gas hold-up (between sensors 1 & 3) does not allow the clear identification of a single transition point. This last observation supports the doubts of Letzel et al. (1997) on the usefulness of the gas hold-up for the flow regime identification. Thus the need for more reliable analysis methods is obvious.

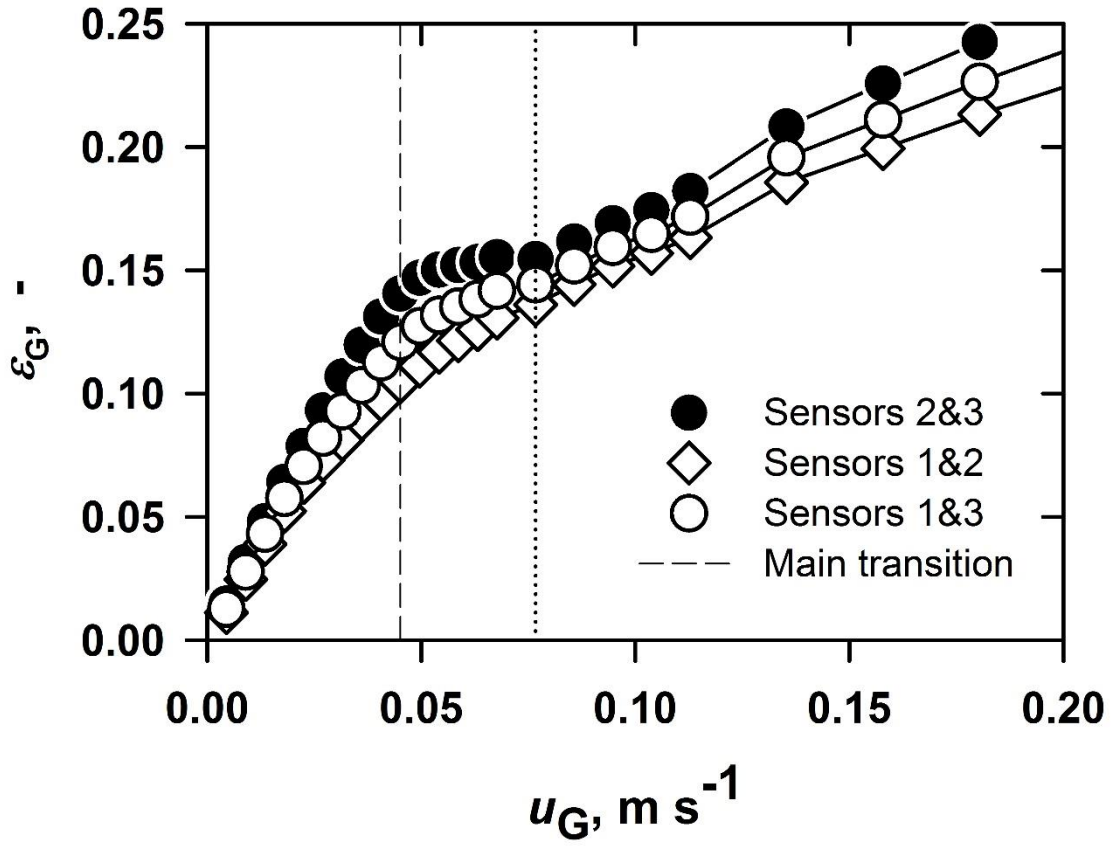

Figure 32: Gas hold-up (water/nitrogen, P = 0.1 MPa, h_0 = 1.50 m).

Based on the gas hold-up analysis, the main transition point is located at about 0.045 m s^{-1}. This first approximation is helpful to establish the criteria of boundary identification for the other methods studied.

The use of the drift flux aims at increasing the accuracy of flow regime identification based on the gas hold-up measurement. Figure 33 depicts the evolution of the drift flux as expressed by Zuber & Findlay (1965) and Wallis (1969), respectively. Two to four regions can be identified. At low u_G values, a new region characterised by the decrease of the drift flux is identified for the Zuber & Findlay model. This region is followed by an increase of the drift flux with u_G. In the upper region of the column, this increase shows two (to three) changes of slope.

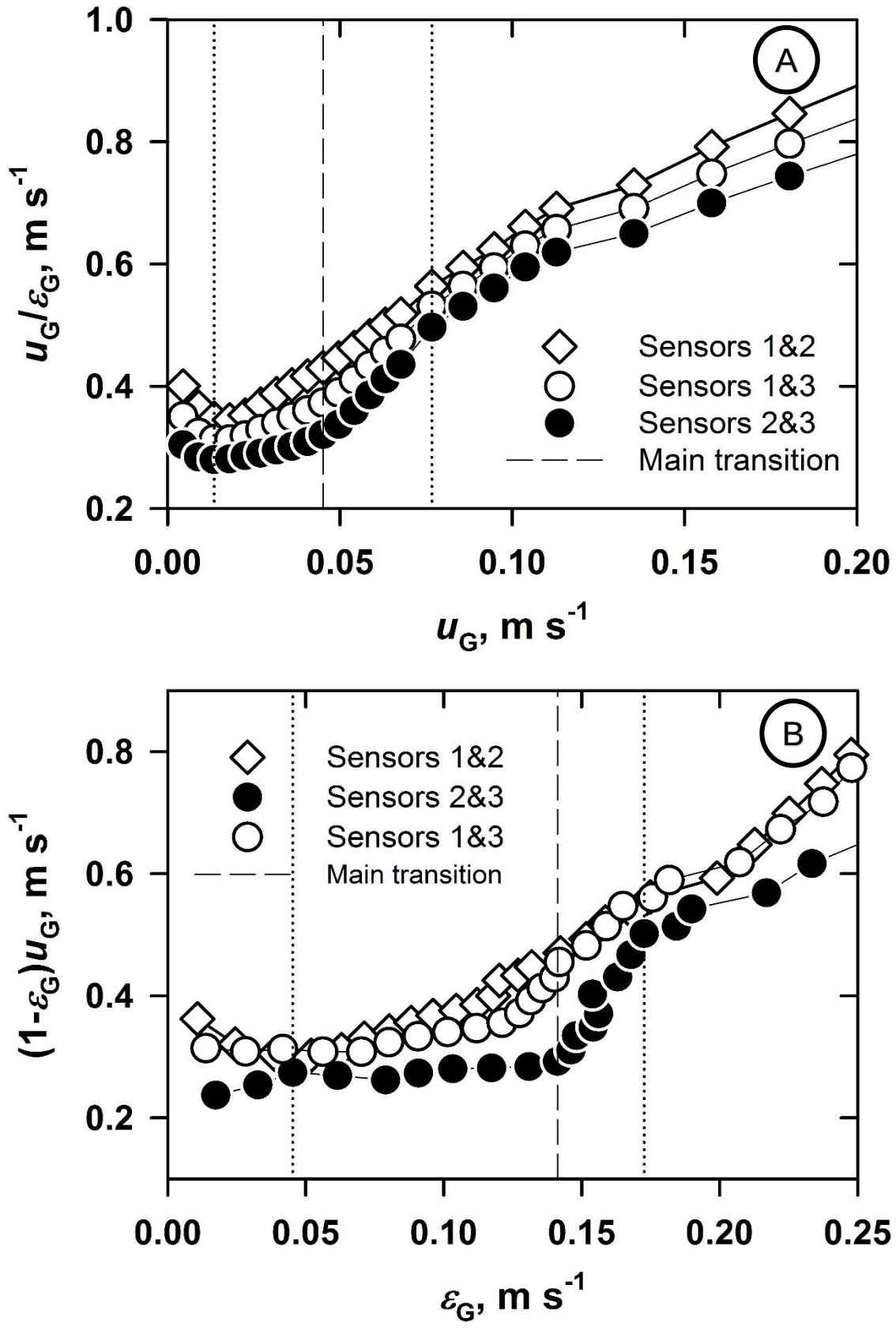

Figure 33: Drift flux A: Zuber & Findlay's model (eq. 5), B: Wallis model (eq. 6) (water/nitrogen, P = 0.1 MPa, h_0 = 1.50 m).

Globally, the curves obtained show more structure than those reported in the literature. The Wallis model expressed as a function of the gas hold-up shows also two to three regimes. The main transition located at the critical gas hold-up 0.14 corresponds to the result of the gas hold-up analysis (see Figure 32).

The drift flux did not lead to a more accurate identification of the main transition, but the probable existence of another flow pattern at low gas velocities is an additional information not detectable from the gas hold-ups directly. This specific result does not match with those reported in the literature.

b. The statistical analysis

Figure 34 depicts the characteristic trend found by the standard deviation analysis. The variation of the sensor axial location and the clear liquid height have no influence on the evolution of σ with u_G. Three regions are always identified. The first region located at very low gas velocities is mostly marked by an abrupt decrease of σ with u_G to very low values. The following region is characterised by very low values of σ which slightly increase with u_G by up to 5%. Finally, the third region shows a strong continuous increase of σ with u_G. Except for the first region, these results are in good agreement with the literature. The first region at very low gas velocities is usually missing.

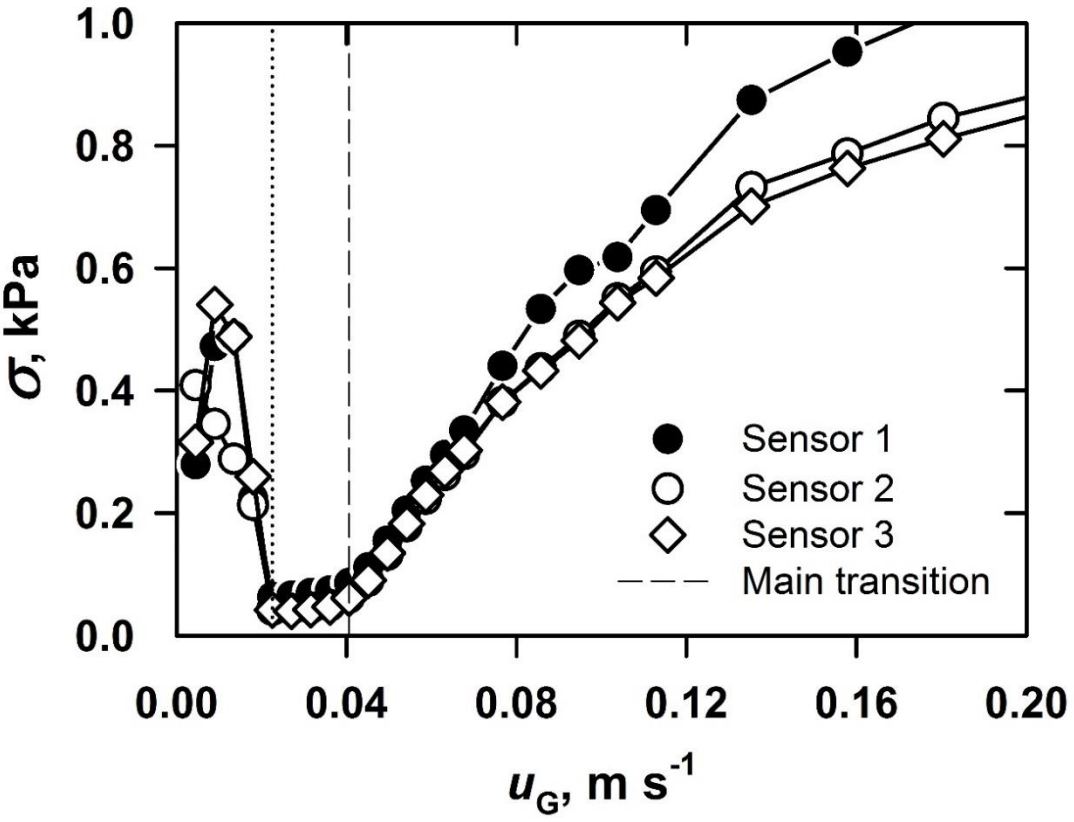

Figure 34: Standard deviation (water/nitrogen, P = 0.1 MPa, h_0 = 1.50 m).

Figure 35 shows a sample of the skewness and kurtosis as a function of the gas velocity. Whatever the sensor location used, no trends and no transition can be detected. This result is in agreement with those reported by Vial et al. (2000) who also found no significant correlation between the skewness and the prevailing hydrodynamic patterns.

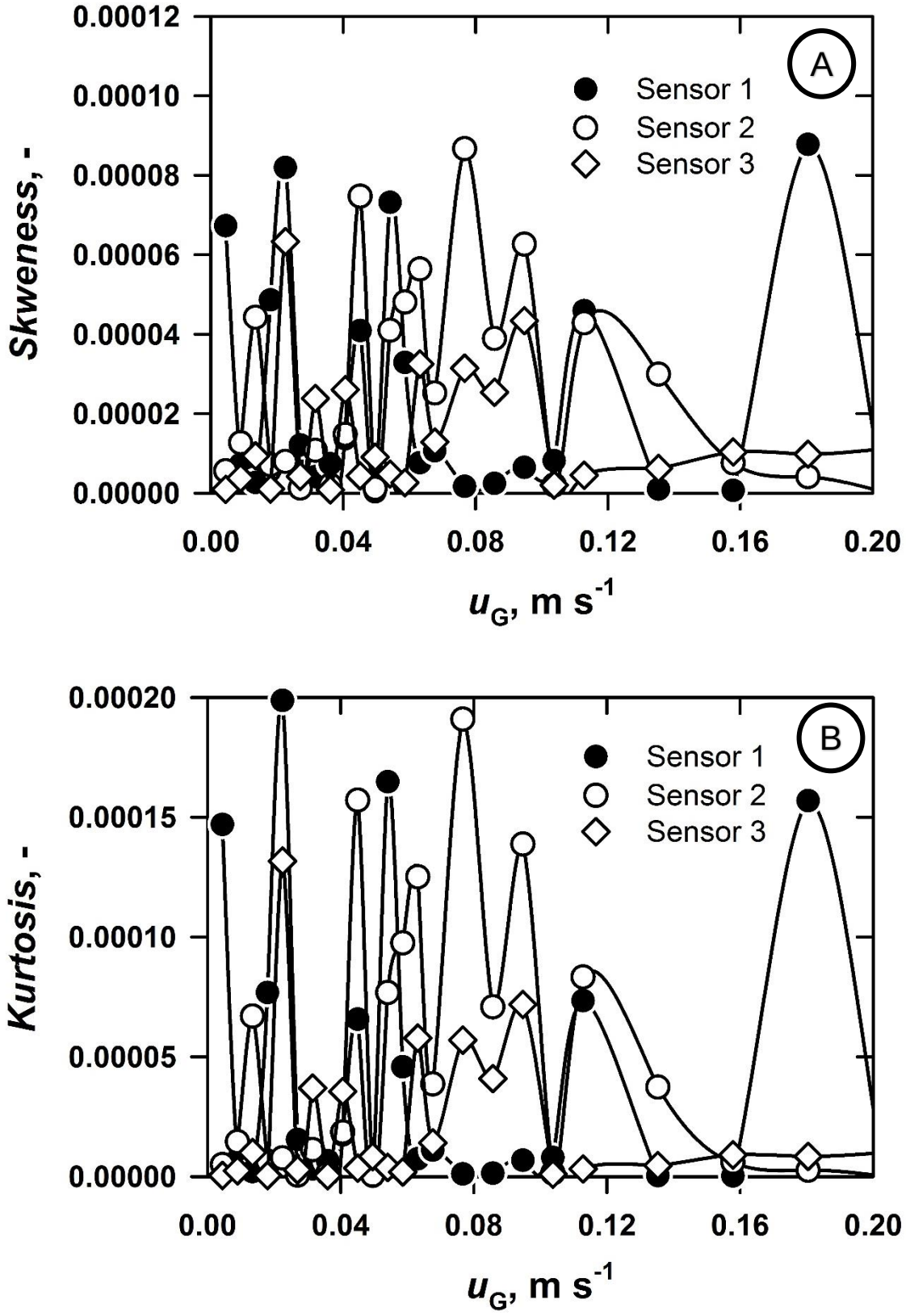

Figure 35: A: Skewness (eq. 10) and B: Kurtosis (eq. 11) (water/nitrogen, P = 0.1 MPa, h_0 = 1.50 m).

Figure 36 depicts the average cycle time (eq. 21) for the system water/nitrogen at atmospheric conditions. The clear liquid height and the sensor axial location affect significantly the evolution of T_C. Sensor 1 shows significant differences at high gas velocities.

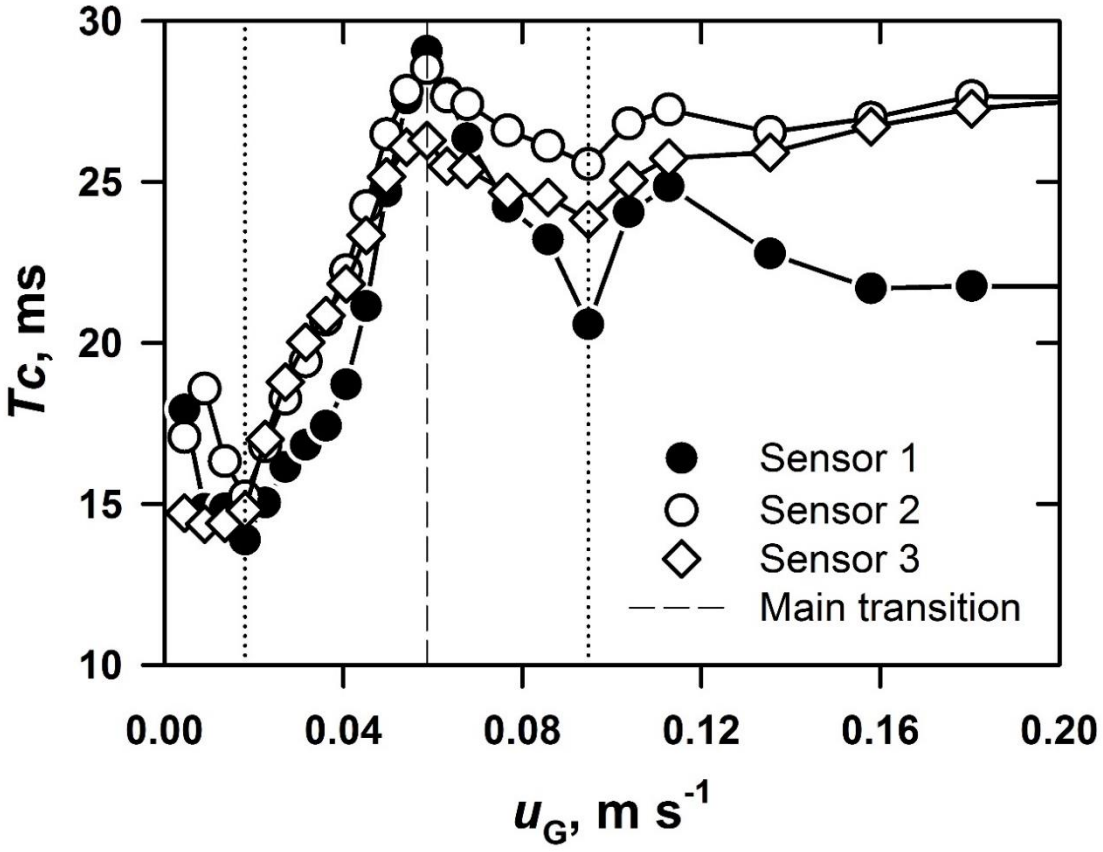

Figure 36: Average cycle time – eq. 21 (water/nitrogen, P = 0.1 MPa, h_0 = 1.50 m).

Despite these differences, four regions are identified. The first region corresponds to low or decreasing values of T_C with u_G. The second region corresponds always to a fast increase of T_C with u_G. After a maximum, the average cycle time decreases in the third region. The forth region shows usually only slight variations T_C with u_G. The maximum of T_C occurs at a high gas velocity of almost 0.06 m s^{-1} whereas the main transition is expected at around 0.045 m s^{-1}. The average cycle time is not used as an identification method in the literature and, therefore, cannot be compared to previously reported results.

c. The fractal analysis

Figure 37 depicts the results obtained by the fractal analysis. The trends are typical for all systems at atmospheric conditions. The variation of the clear liquid height and the sensor axial location give more or less structure to the evolution of d_F with u_G. The boundaries marked on Figure 37 are only related to the first sensor.

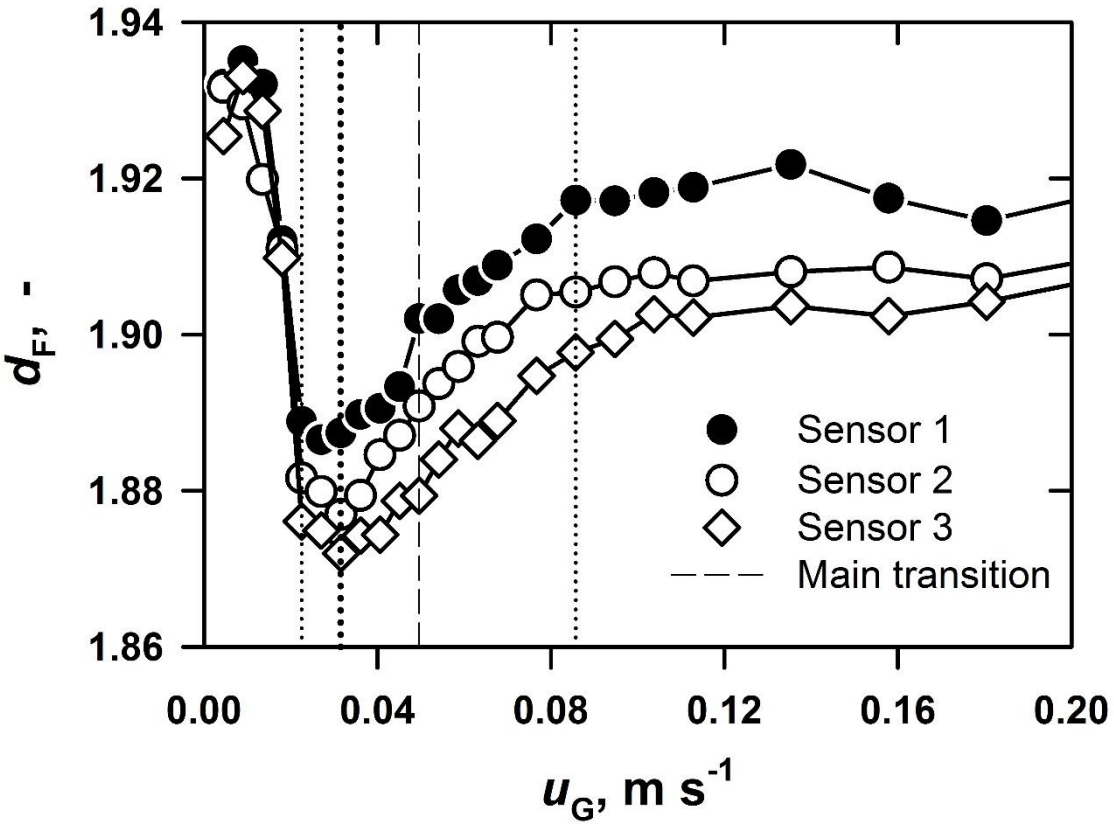

Figure 37: Fractal dimension (water/nitrogen, P = 0.1 MPa, h_0 = 1.50 m).

Despite the shift of the transitions for the three curves, three to four regions are identified. The first region always shows an abrupt decrease of d_F with u_G, the last one corresponds to a very slight variation or a constant value of d_F. In the intermediate region d_F increases with u_G. This region shows more or less structure depending on the system studied, the clear liquid height and the sensors axial location. It is remarkable that the main transition point cannot be identified at all based on the signal of both upper sensors. These results

are in good qualitative agreement with the trends reported by Li et al. (2013), however, their absolute values are significantly lower.

d. The spectral analysis

Figure 38 depicts typical results of the spectral analysis for at atmospheric conditions. The variation of the clear liquid height or the sensors axial location has little influence on the evolution of the power spectral density (PSD) with u_G.

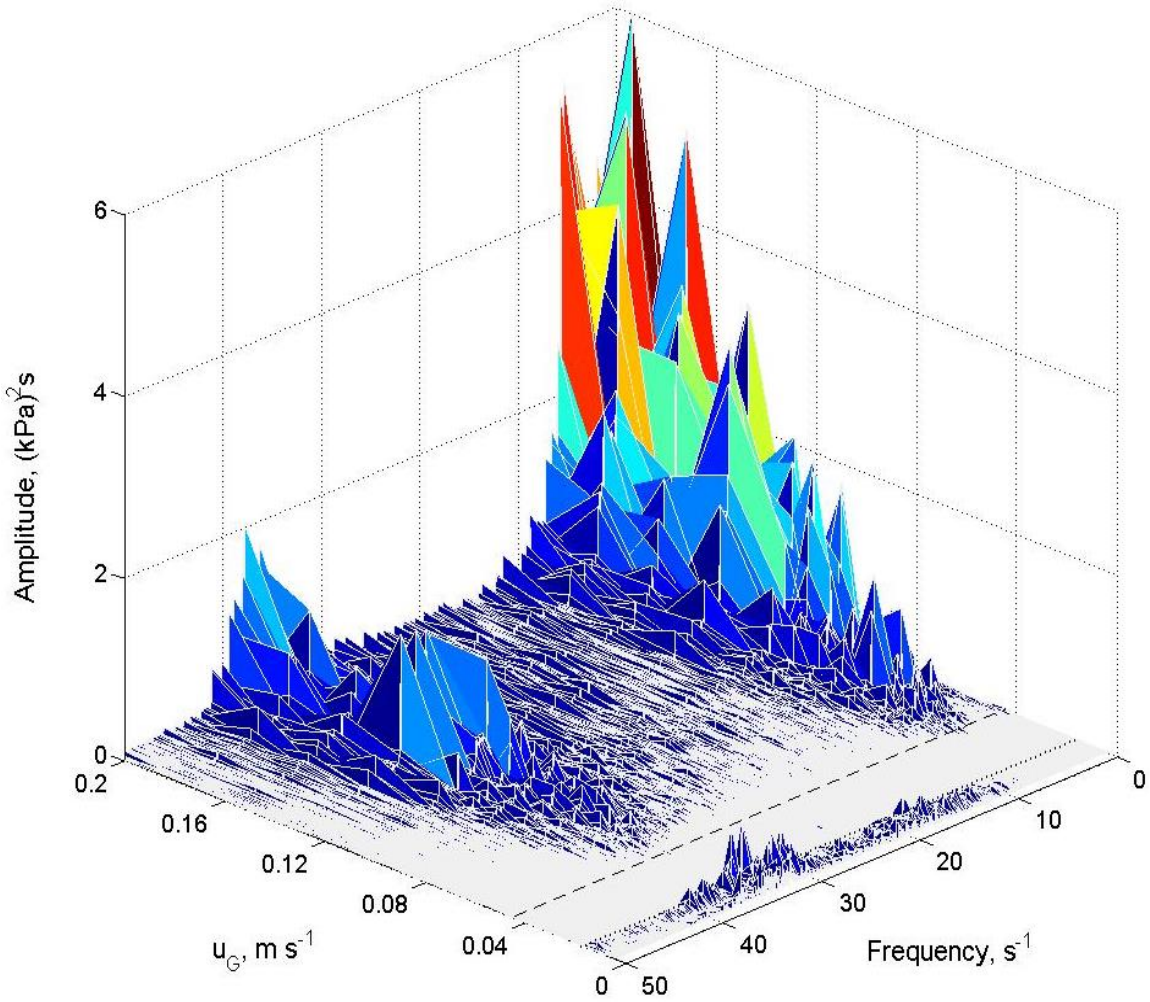

Figure 38: Power spectral density (water/nitrogen, P = 0.1 MPa, h_0 = 1.50 m, sensor 2).

Three main regions are identified. The region at very low u_G values is mostly marked by a pronounced peak at frequencies of about 35 s^{-1}. This peak is wide at its base and splits into two at its top. It follows a region characterised by the total absence of peaks. At the gas velocity typical for homogeneous flow, there is a completely clear zone. High gas velocities are characterised by the presence of pronounced peaks from 0 to 20 s^{-1} and from 35 to 45 s^{-1}. Depending on the axial location of the sensors, these peaks adopt specific frequencies and amplitudes.

The detailed expression of PSD as function of u_G is seldom reported in the literature. Single values of PSD taken in a specific flow regime are often presented. The peak located at 5 s^{-1} is the most reported in the literature. Peaks around 15 s^{-1} were also reported by Vial et al. (2000) and Chilekar (2007). The peaks found below 25 s^{-1} are in good agreement with those reported in the literature while the region above 25 s^{-1} was usually not considered.

e. The chaos analysis

Figure 39 depicts the typical trend of the Kolmogorov entropy K_E. The variation of the clear liquid height and the sensor axial location has no influence on the main transition but can shift the sub-boundaries. Thus four main regions are identified. The first region at very low gas velocities is marked very high K_E values followed by an abrupt decrease of K_E with u_G.

After a sharp minimum at the main transition, the following region shows once more an increase of K_E with u_G. A change of the slope at about 0.065 m s-1 might indicate another transition. Finally, the last region at high gas velocities is characterised by a relatively constant value of K_E. Except for the first region that is seldom investigated, the results obtained from the Kolmogorov entropy analysis are in good agreement with those reported by Letzel et al. (1999). They reported the same trends for higher pressure.

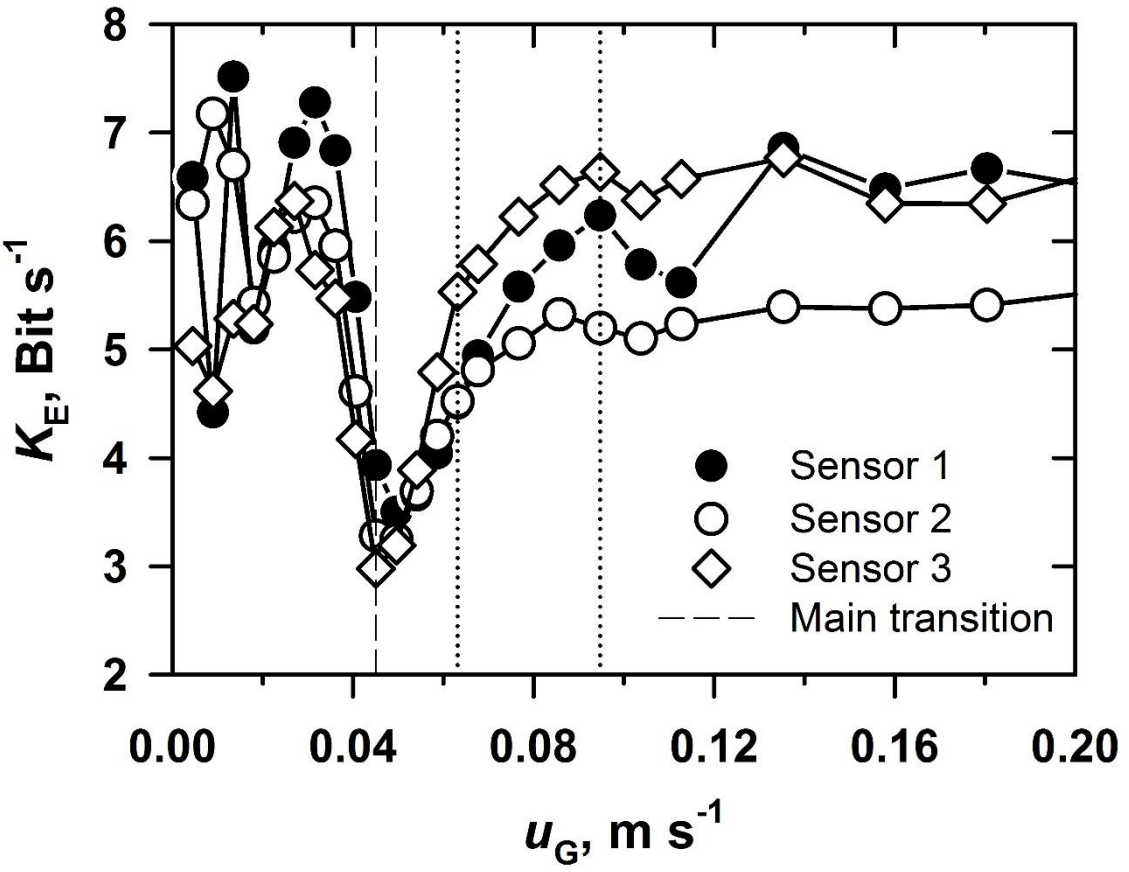

Figure 39: Kolmogorov entropy – eq. 14 (water/nitrogen, P = 0.1 MPa, h_0 = 1.50 m).

Figure 40 is representative of the evolution of the information entropy (eq. 15) with the gas velocity. The variation of the clear liquid height and the sensor axial location has no influence on the evolution of I_E with u_G. Three regions are always identified. The first region at very low gas velocities is always marked by an abrupt decrease of I_E with u_G. The second following region is characterised by a moderate increase of I_E with u_G. In the third region I_E first increases more steeply with u_G but the slope decreases steadily; no clear transition can be found.

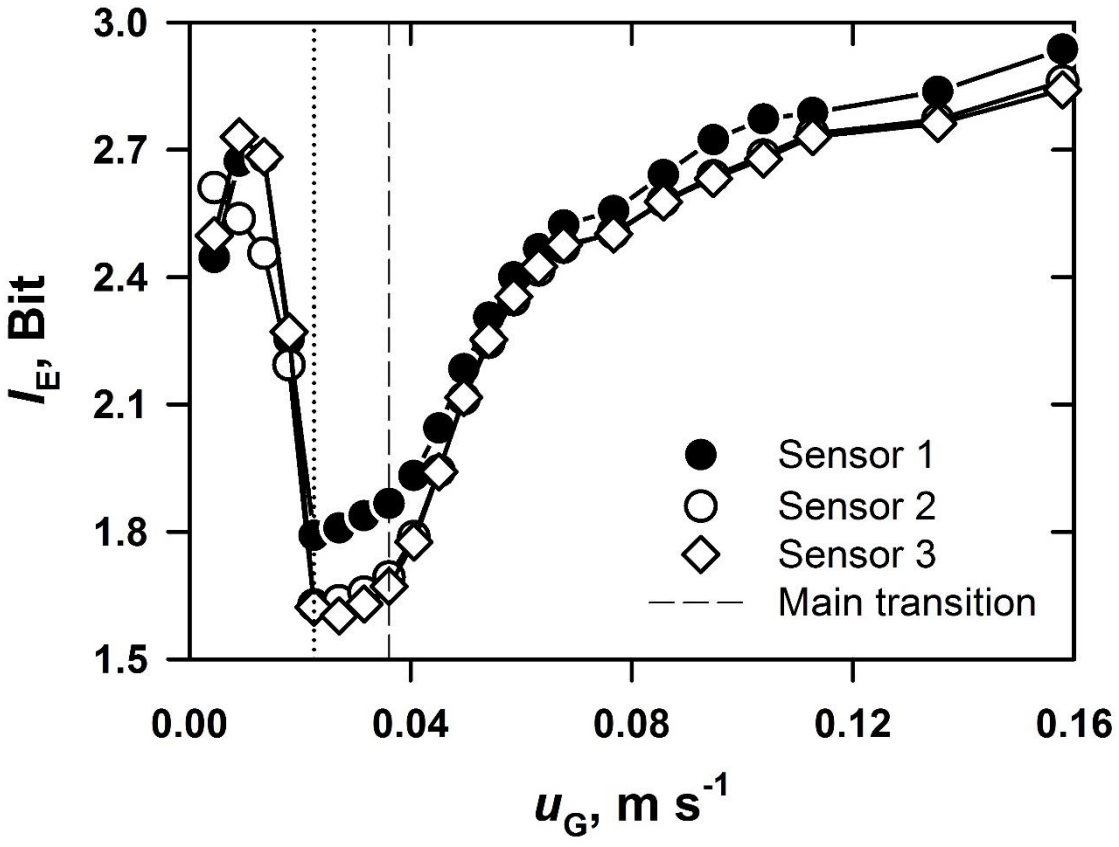

Figure 40: Information entropy – eq. 15 (water/nitrogen, P = 0.1 MPa, h_0 = 1.50 m).

In spite of a global resemblance of trend between these results and those reported by Nedeltchev and Shaikh (2013), the absence of the second minimum (cf. Figure 21) makes an important difference to be emphasised.

4.1.2 Identified flow regimes

Four sub-regimes illustrated on Figure 41 are identified. This identification is mostly based on the Kolmogorov entropy, the fractal dimension and the power spectral density analyses. The other analysis methods contributed partially to the establishment of the three boundaries.

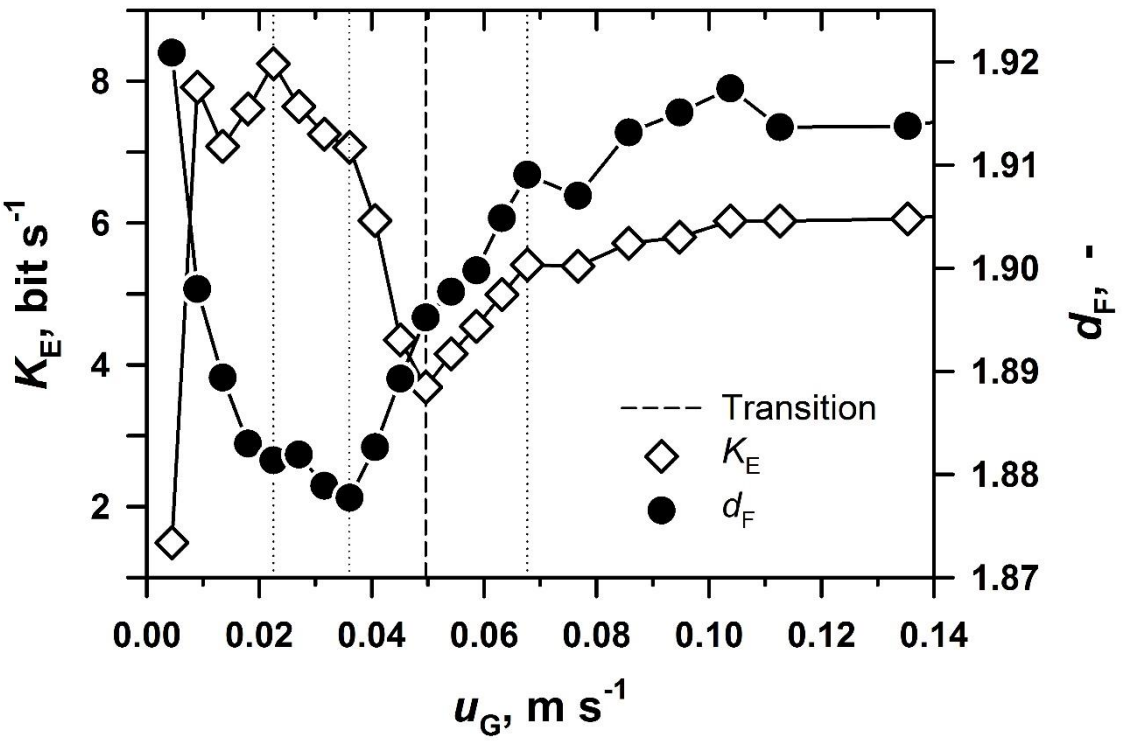

Figure 41: Flow boundaries identified on the basis of the Kolmogorov entropy and the fractal dimension, respectively (water/nitrogen, P = 0.1 MPa, h_0 = 1.25 m, sensor 1).

a. The intermittent flow regime (first region)

The first identified region extends from 0 to 0.02 m s^{-1} superficial gas velocity. As already mentioned, this range of gas velocity is often skipped in the literature. Figure 42 shows a characteristic sample of the pressure fluctuation signal recorded in that region. It depicts a fish like signal made of the intermittence of high and low frequency fluctuations. This explains clearly the high standard deviation values observed in that region (see Figure 34). Figure 43 shows a characteristic sample of the gas disengagement analysis carried out it this region. It proves a narrow size distribution of the bubbles, meaning an almost unique class of bubbles.

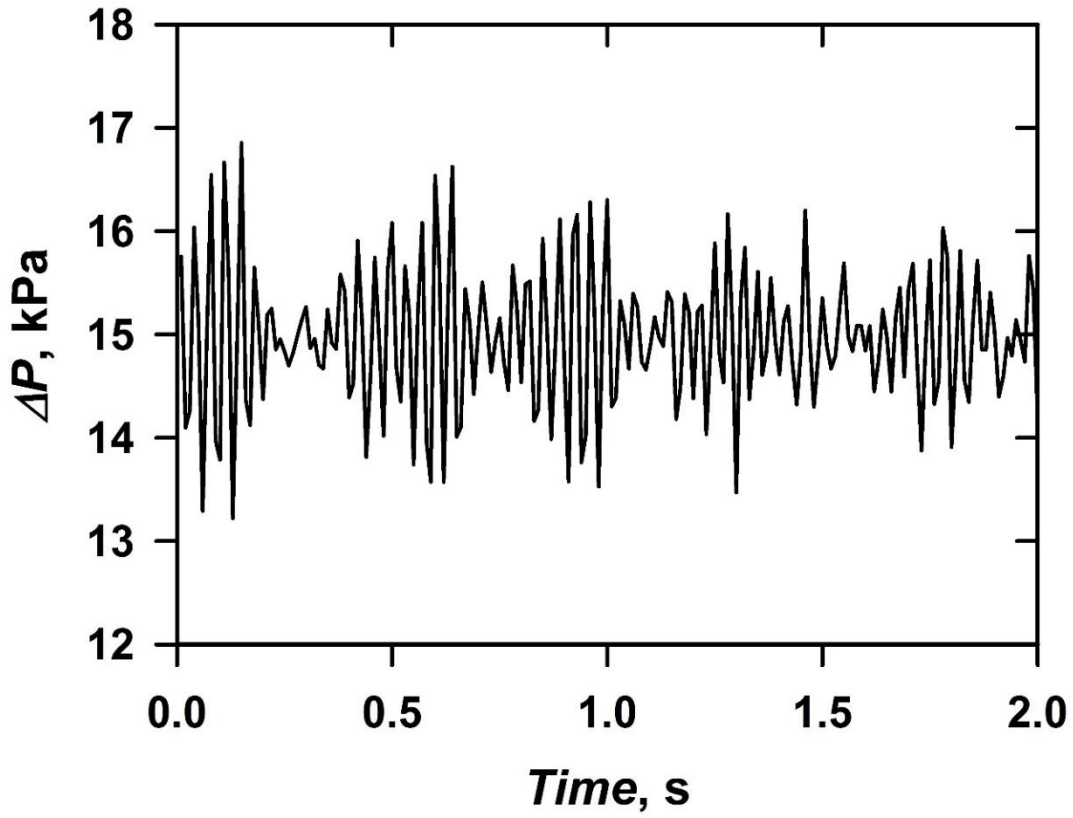

Figure 42: Sample of the pressure fluctuations (water/nitrogen, u_G = 0.001 m s^{-1}, P = 0.1 MPa, sensor 1).

The slightly higher bubble rise velocity noticed in this region (see the drift flux analysis, Figure 33A) can explained by the intermittent release and rise of the bubbles clusters. The drift flux decreases with u_G in this region and reaches the lowest values of the whole curve. Further increase of u_G then entrains a decrease in bubble rise velocity. The decrease of the swarm velocity with the increasing hold-up is a well-known effect (Drahoš et al., 2003)

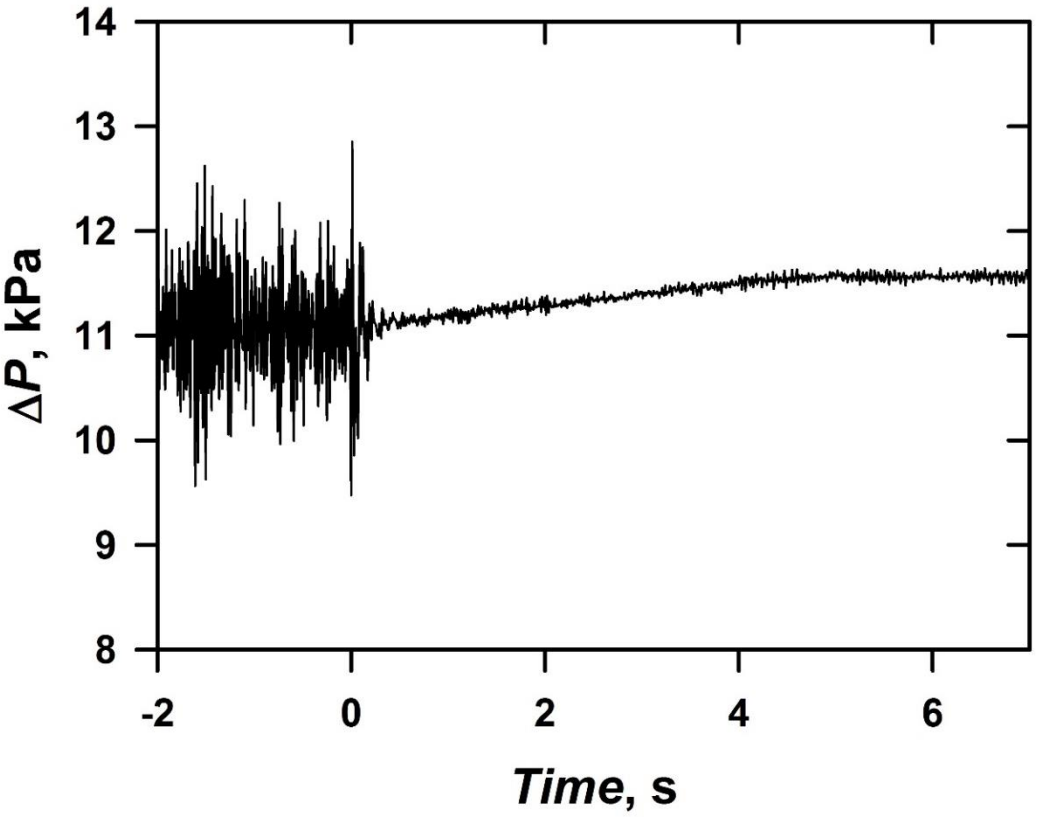

Figure 43: DGD profile (water/nitrogen, u_G = 0.001 m s^{-1}, P = 0.1 MPa, sensors 1 & 3).

This result is confirmed by Figure 44 which shows rising bubbles in the intermittent flow regime. Successive coats of bubbles rising one after another are observed. This supposes a frequency fluctuation in the bubbles' release. The release becomes more uniform with the gas velocity increase. The progressive disappearance of the intermittent pattern is then a function of the distance from the sparger. At high axial location, it can be hardly detectable.

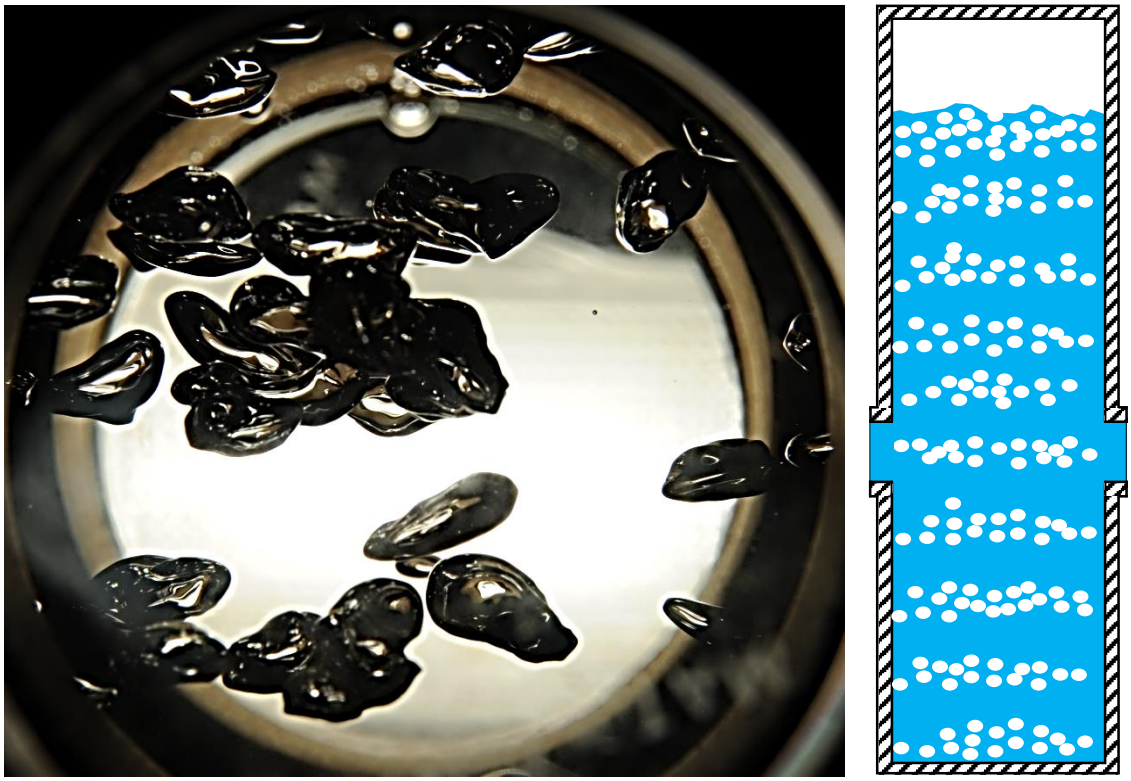

Figure 44: Bubbles at intermittent flow (water/nitrogen, u_G = 0.001 m s^{-1}, P = 0.1 MPa).

According to Mersmann (1978), for the continuous formation of bubbles with operation independent of the pressure fluctuation on both sides of the sparger (Ruzicka et al., 2003), the orifice Weber number should equal at least 2.

We have:

$$We = \frac{\rho_G {u_0}^2 d_0}{\sigma_L} \rightarrow u_o = \left(\frac{W_e \sigma_L}{\rho_G d_o}\right)^{0.5}$$

Knowing that $u_0 = \frac{\dot{V}_G}{N_h \pi \left(\frac{d_0}{2}\right)^2}$ and $u_G = \frac{\dot{V}_G}{\frac{\pi {D_c}^2}{4}}$

Then $u_0 = \frac{{D_c}^2}{N_h {d_0}^2} u_G$

and

$$u_G = \sqrt{\frac{We\ \sigma_L\ {N_h}^2\ {d_0}^3}{{D_c}^4\ \rho_G}}$$

With $We_{crit} = 2$

$\sigma_L = 0.07$ liquid surface tension

$N_h = 19$, number of holes

$d_0 = 0.001$ m, hole diameter

$\varrho_G = 1000$ kg m^{-3}, liquid density

$D_c = 0.102$ m, bubble column inner diameter

$u_{G,\,crit}$ = 0.020 m s^{-1}

This result is in good agreement with the experiments.

b. The homogeneous flow regime (second region)

The second identified region extends from 0.02 to 0.041 m s^{-1}. Figure 45 shows a characteristic sample of the PFS recorded in that region. It depicts a regular sinusoidal signal with significantly lower fluctuation amplitudes than in the first region. This explains clearly the very low standard deviation values observed (see Figure 34). The increasing probability for the signal to cross the mean value explains the increasing values of the average cycle time.

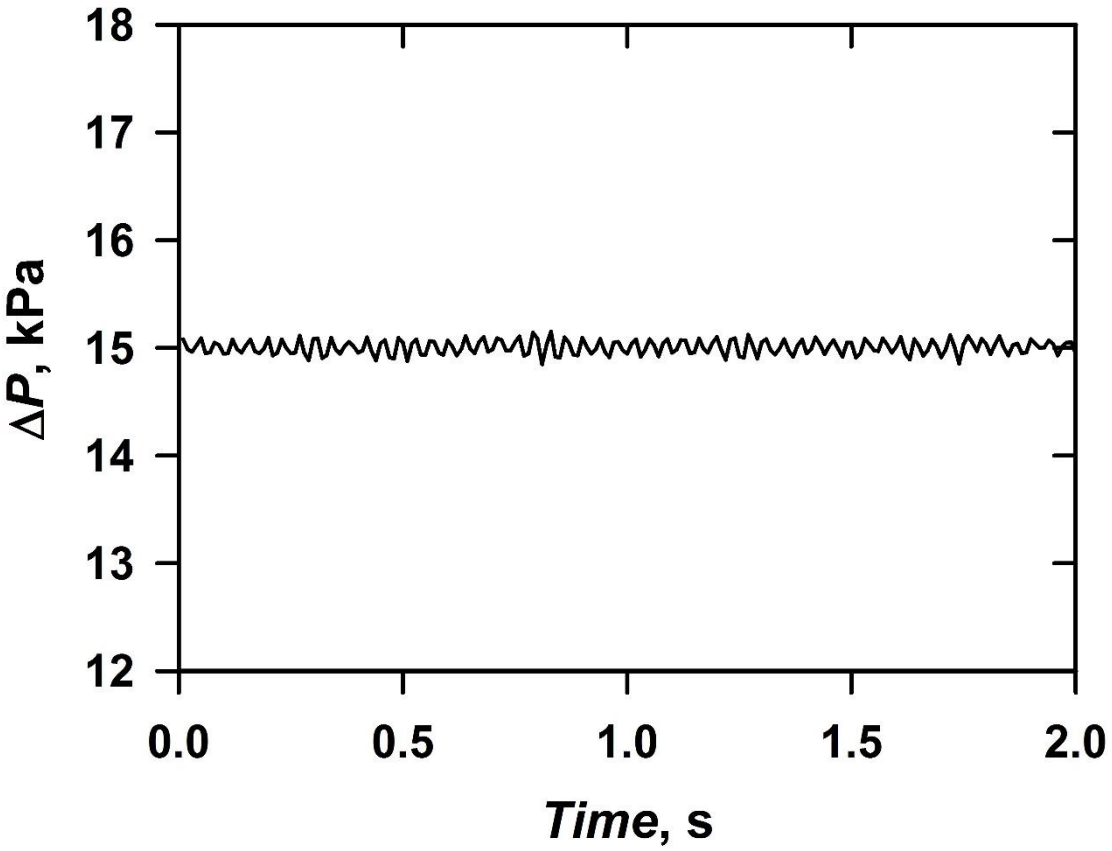

Figure 45: Sample of the pressure fluctuation signal (water/nitrogen, u_G = 0.022 m s^{-1}, P = 0.1 MPa, sensor 1).

Figure 46 is a representative sample of the dynamic gas disengagement for the second identified region and reveals the narrow size distribution of the bubbles. Figure 47 shows a photo of rising bubbles taken at u_G = 0.031 m s^{-1}. It confirms the narrow bubbles size distribution detected by the gas disengagement analysis. It can then be concluded that the second region corresponds to the homogenous regime.

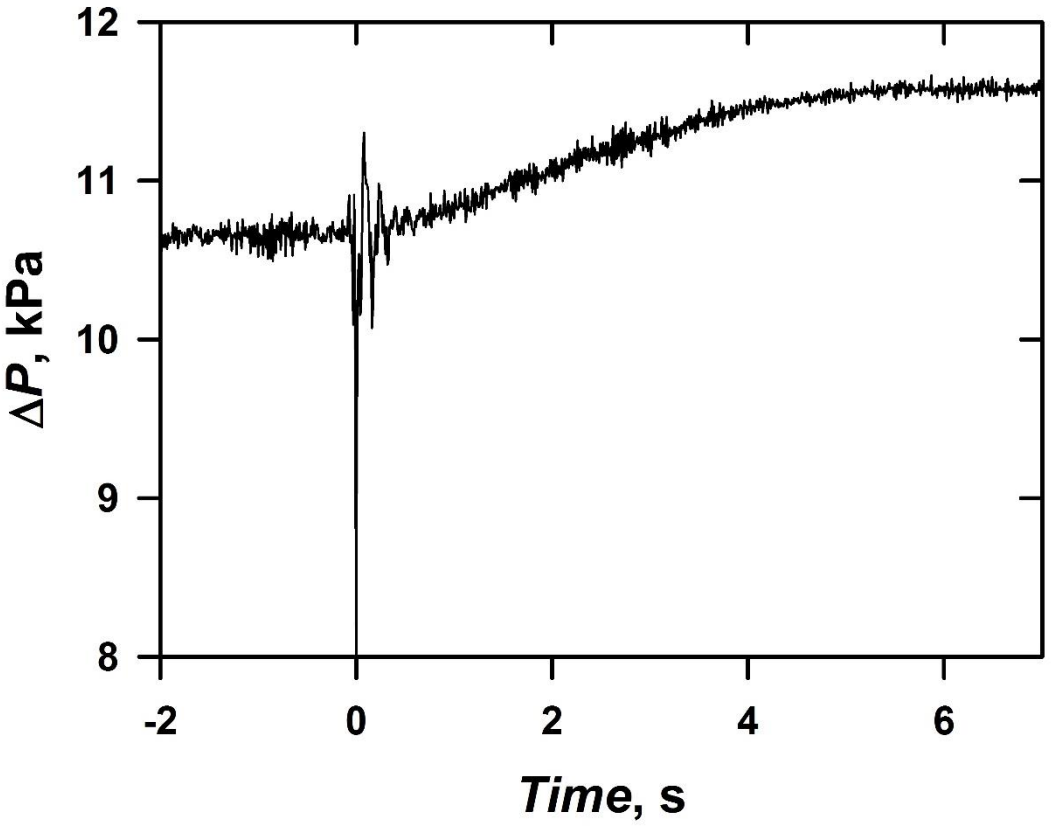

Figure 46: DGD profile at u_G = 0.031 m s^{-1} (water/nitrogen, P = 0.1 MPa, sensors 1 & 3).

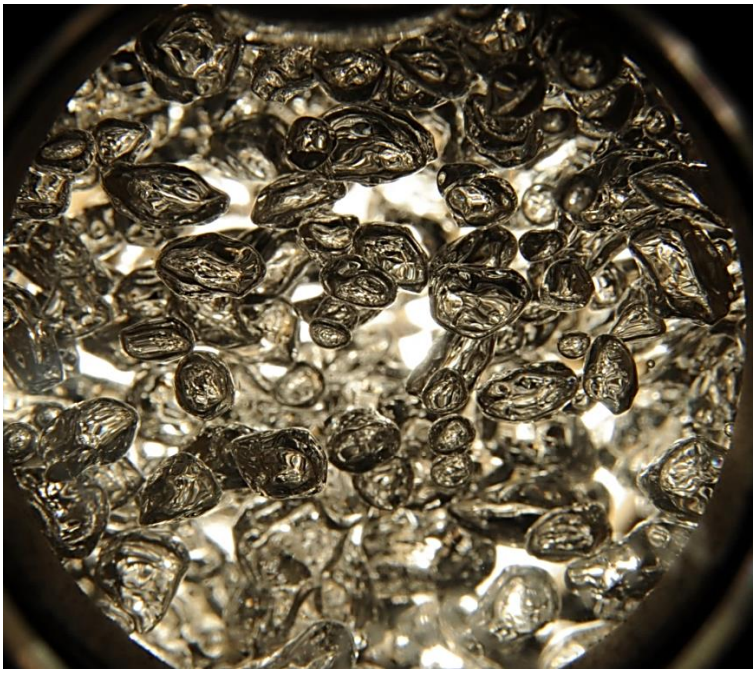

Figure 47: Bubbles in homogeneous flow (water/nitrogen, u_G = 0.031 m s^{-1}, P = 0.1 MPa).

A change of slope within the homogeneous regime can be observed on the K_E curve (see Figure 41) at about 0.03 m s^{-1}. This point corresponds to a minimum of the fractal dimension (see Figure 41). In the literature this minimum is usually considered as the first transition point in analyses carried out solely on the basis of the fractal dimension (or alternatively the Hurst exponent). The Kolmogorov entropy reaches a minimum at a considerably higher gas velocity. At that velocity, the fractal dimension just shows a change of slope (significant for the first sensor, only). The Kolmogorov entropy corresponds much better to the critical gas velocity for the main transition based on the gas hold-up and most other methods. The fractal analysis appears to be too sensitive to early changes in the bubbles flow.

c. The transition flow regime (third region)

The third identified region extends from about 0.045 to 0.065 m s^{-1}. Again, there is an effect of the axial location (see. 4.1.3). Figure 48 shows a sample of the PFS; it depicts a less regular signal with significantly higher fluctuation amplitudes. The former small fluctuations are fused within a trend of higher amplitude and lower frequency. This explains the higher and increasing standard deviation values observed in that region (see Figure 34).

The increase of the gas velocity gives rise to a higher probability of interactions between bubbles and leads to an increase of bubbles size and velocity. The transition regime starts at the point where the first bubbles coalesce. The coalescence of bubbles may cause a decrease of gas hold-up as shown on Figure 32 for the upper part of the column. The gas disengagement (see Figure 49) confirms the presence of two main bubbles classes. Figure 50 shows interactions taking place between bubbles of greater diameters. The wider bubble size distribution can also be noticed. The bubbles formed are not yet large enough to break-up. They rise with a clearly higher velocity, what increases the probability of collusions and, therefore, the rate of coalescence.

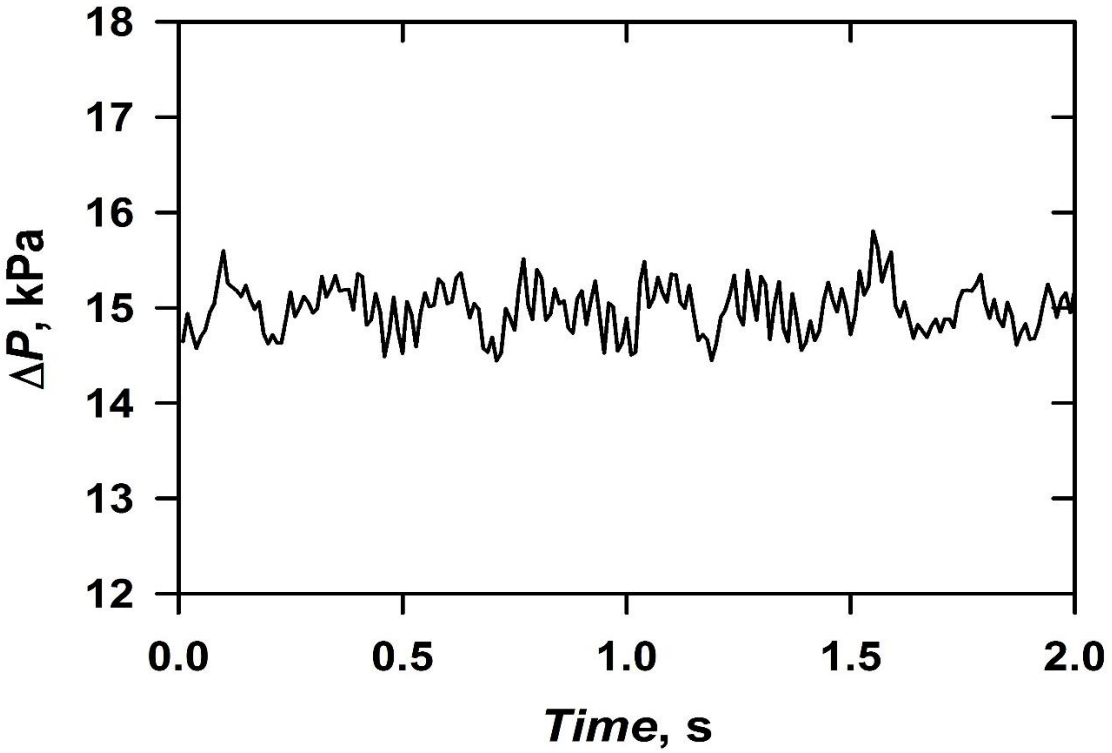

Figure 48: Sample of the pressure fluctuation signal (water/nitrogen, u_G = 0.057 m s^{-1}, P = 0.1 MPa, Sensor 1).

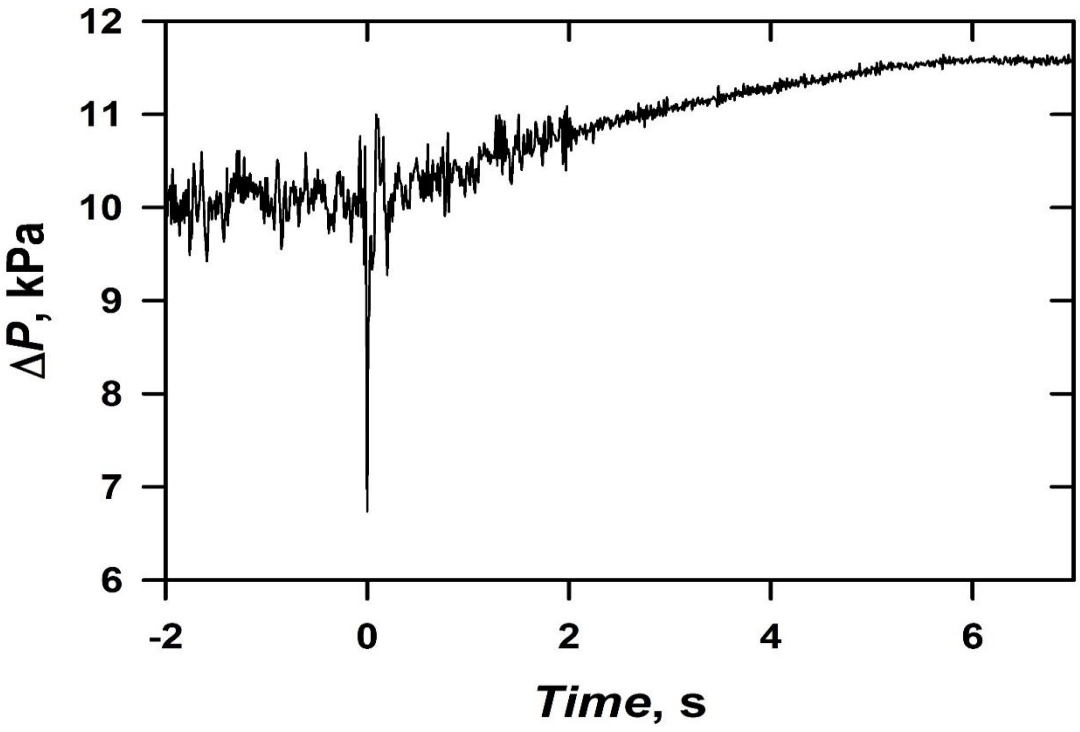

Figure 49: DGD profile at u_G = 0.057 m s^{-1}, (water/nitrogen, P = 0.1 MPa, sensors 1 & 3).

Figure 39 shows a slight shift of the first transition boundary between the upper and the two lower sensors. It proves that the coalescence process takes place first at higher axial locations (Deckwer, 1992).

Figure 50: Bubbles in the transition regime (water/nitrogen, u_G = 0.046 m s^{-1}, P = 0.1 MPa).

Contrary to Letzel et al. (1997) who reported the impossibility of flow regime identification with a sensor located at the bottom of the column, it was possible to identify flow the transitions with the sensor 1 located at the sparger.

d. The heterogeneous flow regime (fourth region)

The fourth identified region starts at about 0.06 m s^{-1}. Figure 51 shows a sample of the PFS recorded in the fourth region. It depicts a chaotic signal which cannot be

characterised as the previous one. The extremely high fluctuations of the signal explain the high values of the standard deviation (see Figure 34).

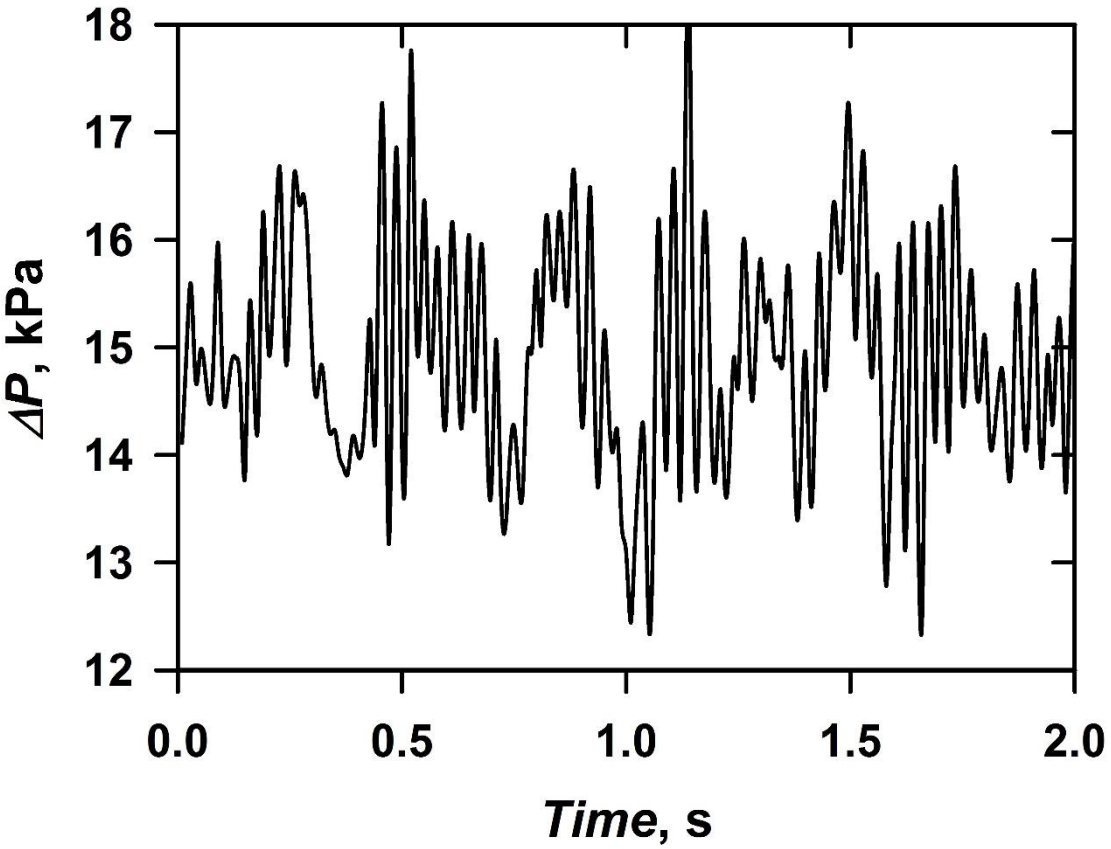

Figure 51: Sample of the pressure fluctuation signal (water/nitrogen, P = 0.1 MPa, u_G = 0.18 m s^{-1}, sensor 1).

The fully established heterogeneous regime is reached when both the coalescence and break-up processes occur in the column. In the first phase from 0.06 to 0.1 m s^{-1}, K_E is still a function of u_G; above 0.1 m s^{-1}, K_E reaches a constant value. The same observation can be made with the fractal dimension. Figure 52 shows a large bubble snapped at 0.096 m s^{-1}. Its dimension and form explain the high fluctuations of the pressure signal (see Figure 51). The deformation it undergoes might be the start of a break-up process; at least the bubble can probably not reach the top in that state. The dynamic gas disengagement (Figure 53) confirms the presence of at least two bubbles classes.

Figure 52: Bubbles in the heterogeneous flow regime (water/nitrogen, u_G = 0.096 m s^{-1}, P = 0.1 MPa).

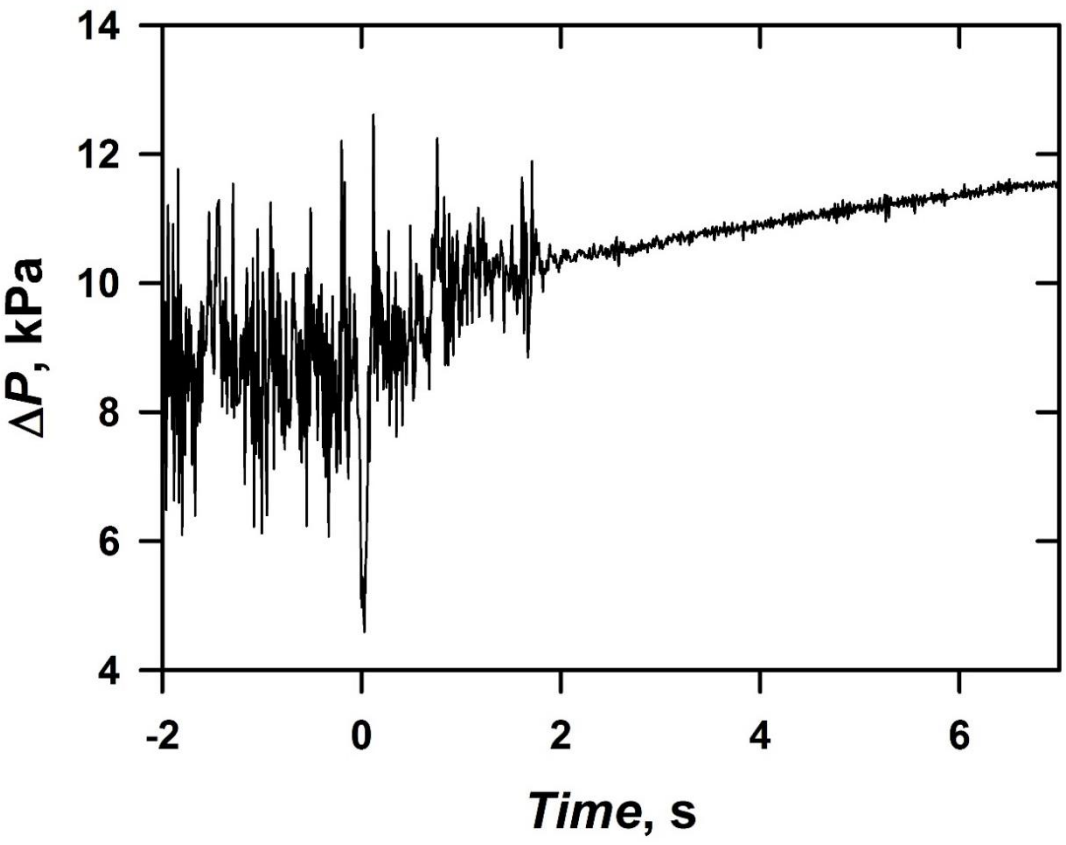

Figure 53: DGD profile at u_G = 0.16 m s^{-1} (water/nitrogen, P = 0.1 MPa, sensors 1 & 3).

4.1.3 Comparative assessment of the methods

Table 7 presents several critical main transition velocities published during the past decades. The values reported are spread on a relatively wide range both for the critical velocities as for the critical gas hold-up values. The critical velocities found belong to the upper limit of the range reported in the literature. Thanks to the ability of the Kolmogorov entropy to give sharp transitions, several boundaries can be established.

Figure 54 shows most of the transition points found at 0.1 MPa within the boundaries established for the three sensors.

- Transition intermittent to homogeneous regime: This transition (independent of the sensor axial location) could be accurately identified with the standard deviation, the PSD, the information entropy and the fractal analysis. The average cycle time showed a minimum at this transition. The Kolmogorov entropy fluctuated strongly and did not allow to define the transition point. Except for the gas hold-up analysis, a change is always noticed at that point.

Table 7: Comparison of the main transition points reported for water (Kantarci et al., 2005).

Research group	$u_{G,crit}$, m s^{-1}	$\varepsilon_{G,crit}$, -
Bach and Pilhofer (1978)	0.046	0.277
Oels et al. (1978)	0.039	0.178
Krishna et al. (1991)	0.033	0.198
Yamashita and Inoue (1975)	0.040	0.234
Hyndman et al. (1997)	0.037	0.137
This study (K_E, sensor 3)	**0.045**	**0.141**

- Main transition: The Kolmogorov entropy and the PSD alone allowed the accurate identification of the main transition point. Using the fractal analysis, this identification could only be performed with the first sensor; the criterion, the change of slope, is not highly objective. The gas hold-up gives a poorer criteria of transition and a lower accuracy.

- Third transition (beginning of the bubbles break-up): A transition is detected with most methods but the critical gas velocity differs widely. The boundary is accurately identified with the Kolmogorov entropy and the gas hold-up for the upper sensors. A comparable trend but at higher gas velocities is observed with the PSD.

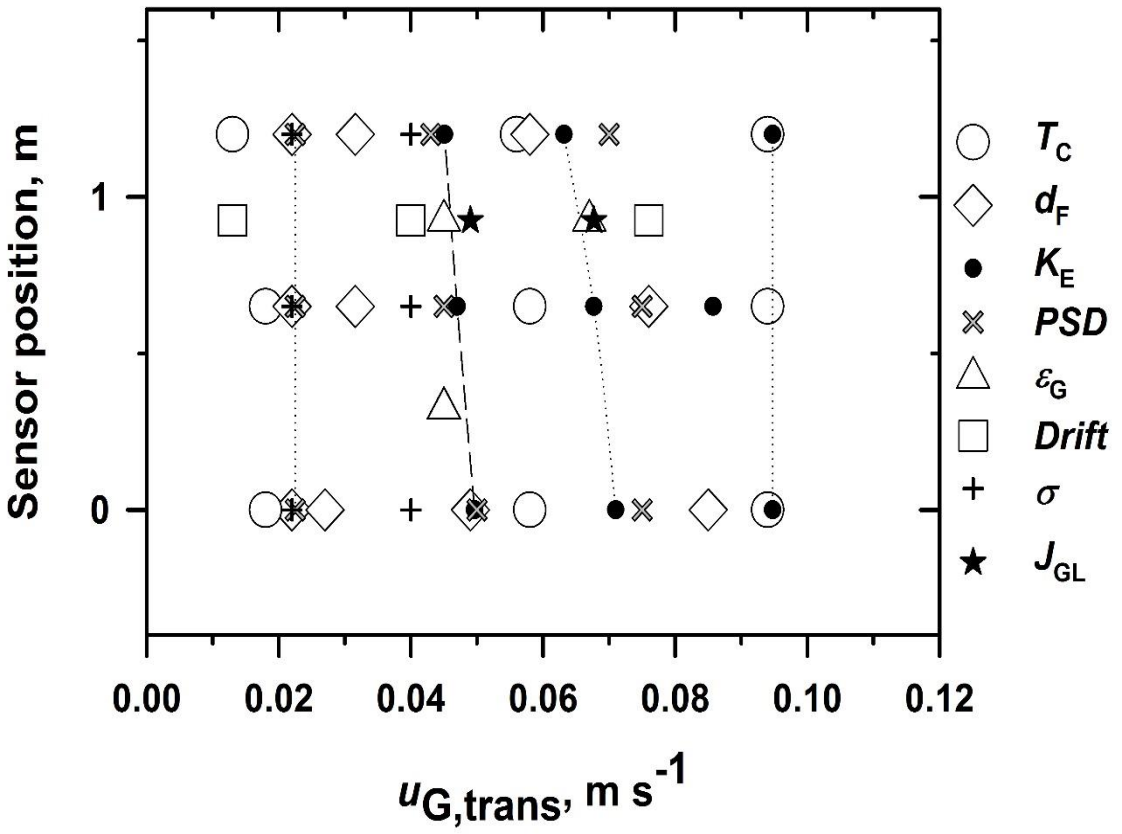

Figure 54: Comparison of the analysis methods used depending on the sensor axial location.

- Fourth transition (stabilisation of coalescence and break-up): Independent of the sensor axial location, this transition is identified with the Kolmogorov entropy and the average cycle time remains constant (independent of the gas velocity increase).

Globally, it is noticed that the classical statistical analysis are not efficient for the transition regimes identification. It can also be confirmed that the gas hold-up cannot be used for the accurate identification of the flow regime transition.

The minimum widely reported for the fractal analysis does not correspond to the main transition point as considered in the literature. The method which measures the self-organisation of the system, depicts an important and reproducible peak that might be associated to the first formation of the bubble clusters (Chilekar, 2007). This bubble cluster formation may be a more significant reorganisation pattern of the system than the coalescence. The beginning of bubbles coalescence is then marked by a change in slope.

The Kolmogorov entropy remains the most reliable method used. The PSD proved to be an identification method with a good level of accuracy. An analysis of the spectra can give a threshold under which the homogeneous regime can be defined, solving the issue of the instantaneous identification of the prevailing flow regime.

Figure 54 proves that two important factors of the discrepancies in the literature are method-specific differences and the effect of the axial location of the sensor. A summary of the methods assessments is listed in Table 8.

Table 8: Comparison of the analysis methods used.

	Regimes	Accuracy [a]	Simplicity [b]	Additional Information
Gas hold-up	2 to 3	0	+	-
Drift flux (Zuber & Findlay)	2 to 3	0	+	Bubble velocity
Drift flux (Wallis)	2 to 3	+	+	-
Standard deviation	2 to 3	0	+	-
PDF	2 to 3	-	+	-
Skewness	none	-	+	-
Kurtosis	none	-	+	-
Average cycle time	3 to 4	+	+	-
Fractal Dimension	3 to 4	++	-	Details in transition
Kolmogorov Entropy	4	++	-	Details in transition
Information entropy	2 to 3	+	0	-
Power Spectral Density	4	+	-	Pressure sources
High Speed Photography	2	+	-	Actual bubbles state

a: aptitude of the method to show a clear sharp transition (peak).

b: refers to the algorithm complexity of the method and its computation duration.

4.2 Effects on the critical gas velocity

4.2.1 Influence of the clear liquid height

Figure 55 illustrates the influence of the clear liquid height on the gas hold-up. The gas hold-up decreases with the clear liquid height increase. This is in good agreement with the results reported by e.g., Ruzicka et al. (2001). The tendency is caused by the onset of coalescence in the upper part of the column.

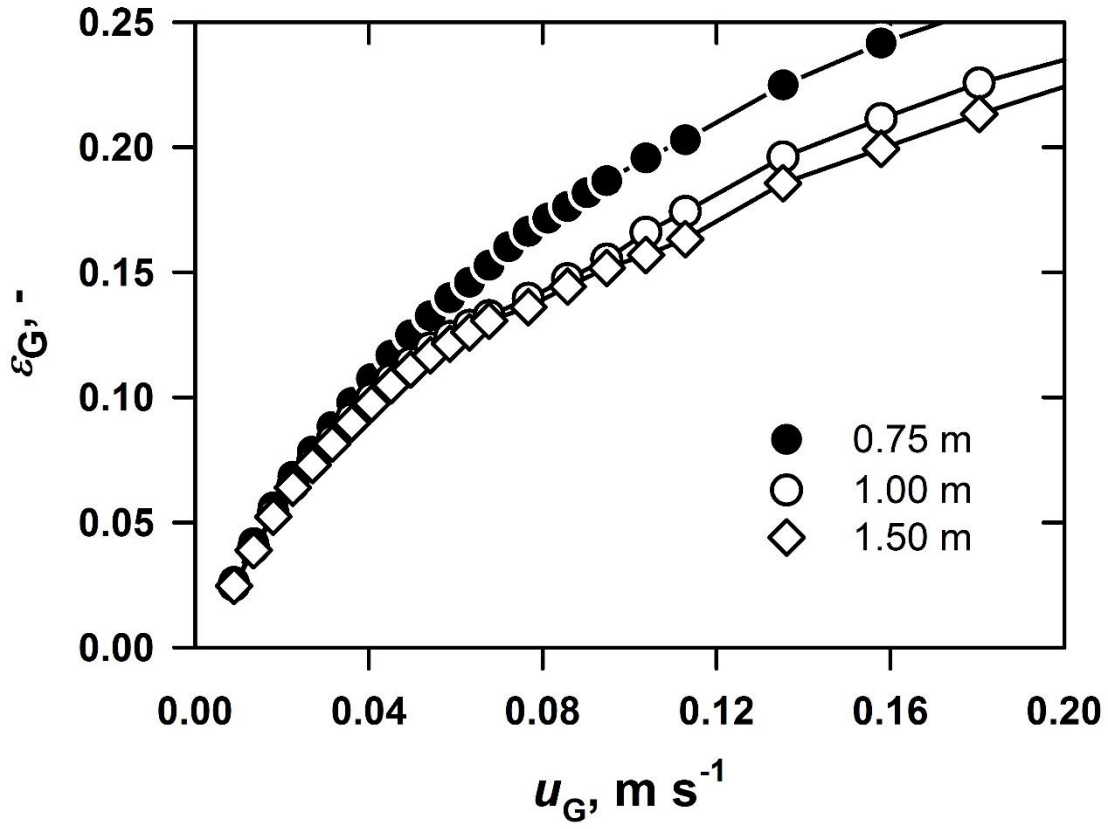

Figure 55: Influence of the clear liquid height on the gas hold-up (water/nitrogen, *P* = 0.1 MPa, sensors 1&2).

Figure 56 shows the effect of the clear liquid height on the transition velocity (based on K_E) for the system water/nitrogen. The main transition point is shifted to lower gas velocity values as the clear liquid height is increased. These results (in contradiction with Drahoš et al. (1991)) confirm those reported by Ruzicka et al. (2001). The critical gas velocity tends to the limiting value: 0.045 m s^{-1}.

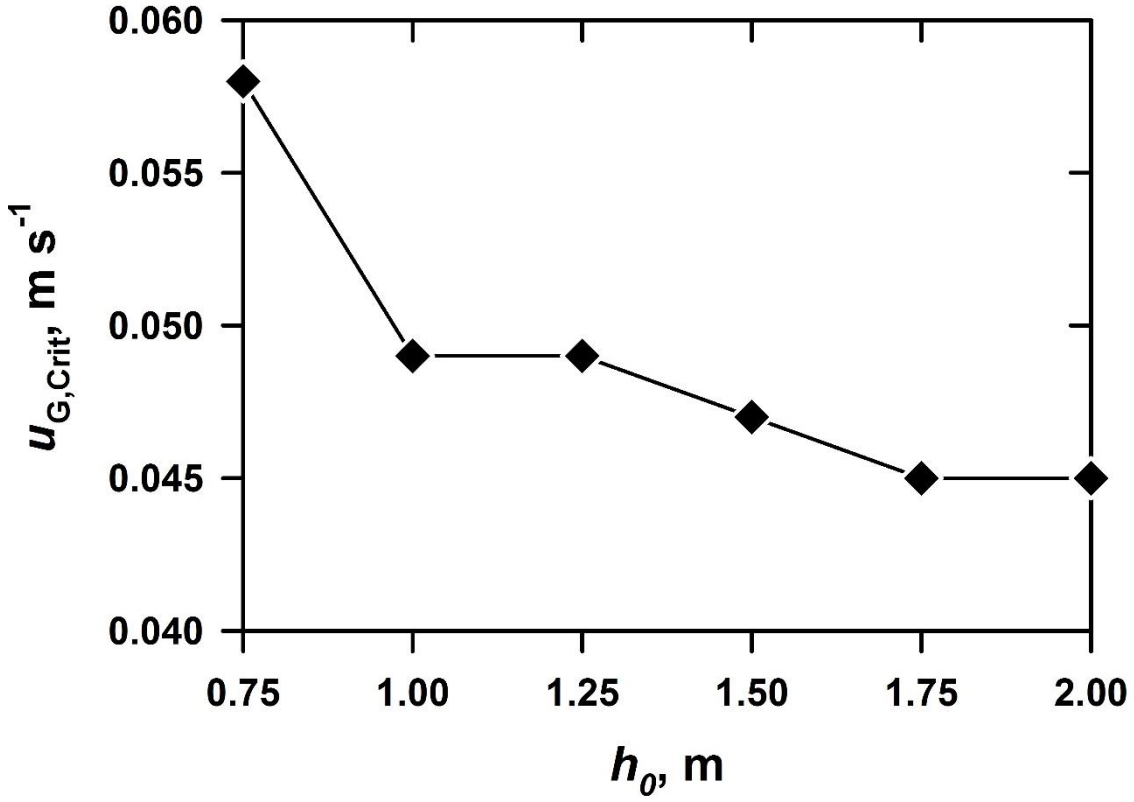

Figure 56: Critical velocity (based on K_E) as a function of the clear liquid height (water/nitrogen, P = 0.1 MPa, sensor 2).

The effect of the clear liquid height can be explained by the minimal distance necessary for the bubbles to coalesce. For high clear liquid height, the bubbles rise longer to reach the top of the column. The multiple bubbles collisions have a higher probability to end in a successful coalescence process. At about 1.75 m clear liquid height, the required critical distance for the collision seems to be reached. The critical velocity is then stabilized at about 0.045 m s^{-1}.

4.2.2 Influence of the viscosity

Figure 57 shows the influence of viscosity on the gas hold-up in the upper part of the column. As already reported in the literature, the gas hold-up decreases with the viscosity. The progressive loss of the curve trend and the disappearance of the transition phase (between 1.25 and 2.00 % CMC concentration) is obvious. In the literature, the decrease of gas hold-up with the viscosity is related to the increase of bubbles sizes.

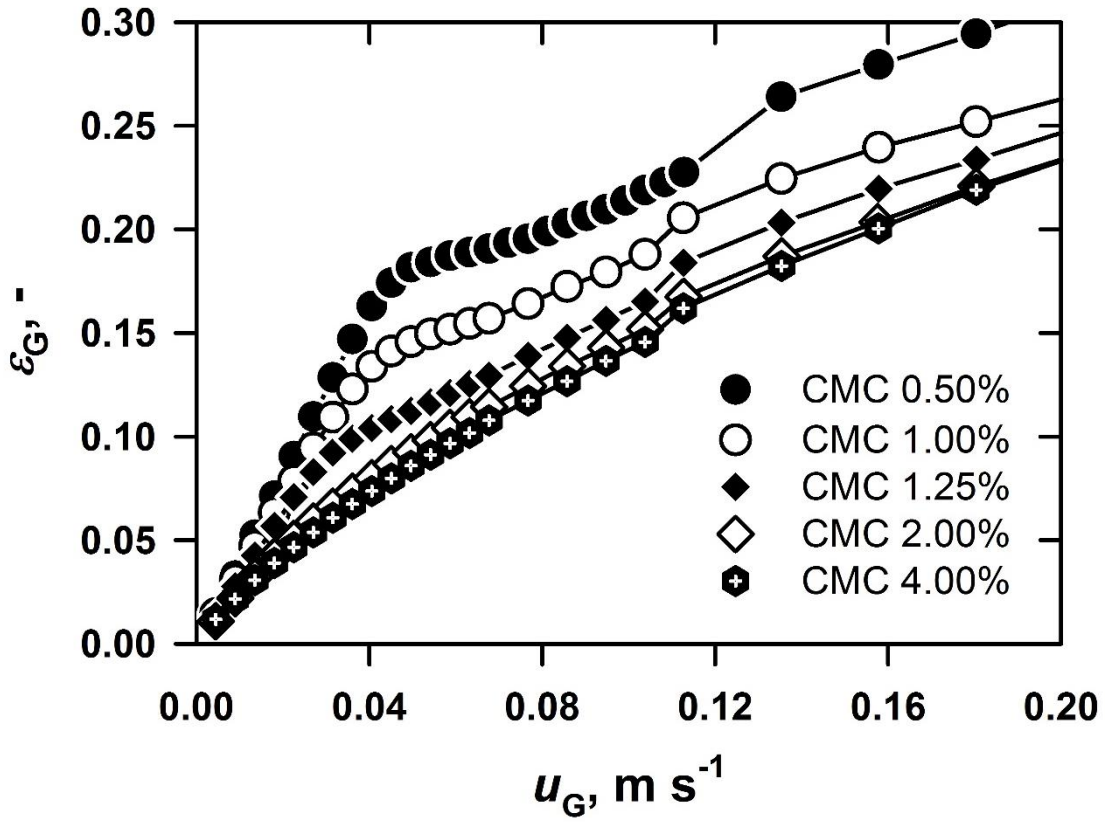

Figure 57: Influence of the viscosity on the gas hold-up (CMC solutions/nitrogen, *P* = 0.1 MPa, sensors 2 & 3, h_0 = 1.50 m).

Figure 58 illustrates the evolution of the fractal dimension with the viscosity; it shows a similar behaviour. The initially highly structured curves, which express the self-organisation of the system become flat as the viscosity increases. A closer look at the structure change shows that the minimum is progressively shifted to lower gas velocity. At 2.00% CMC the minimum is completely missing.

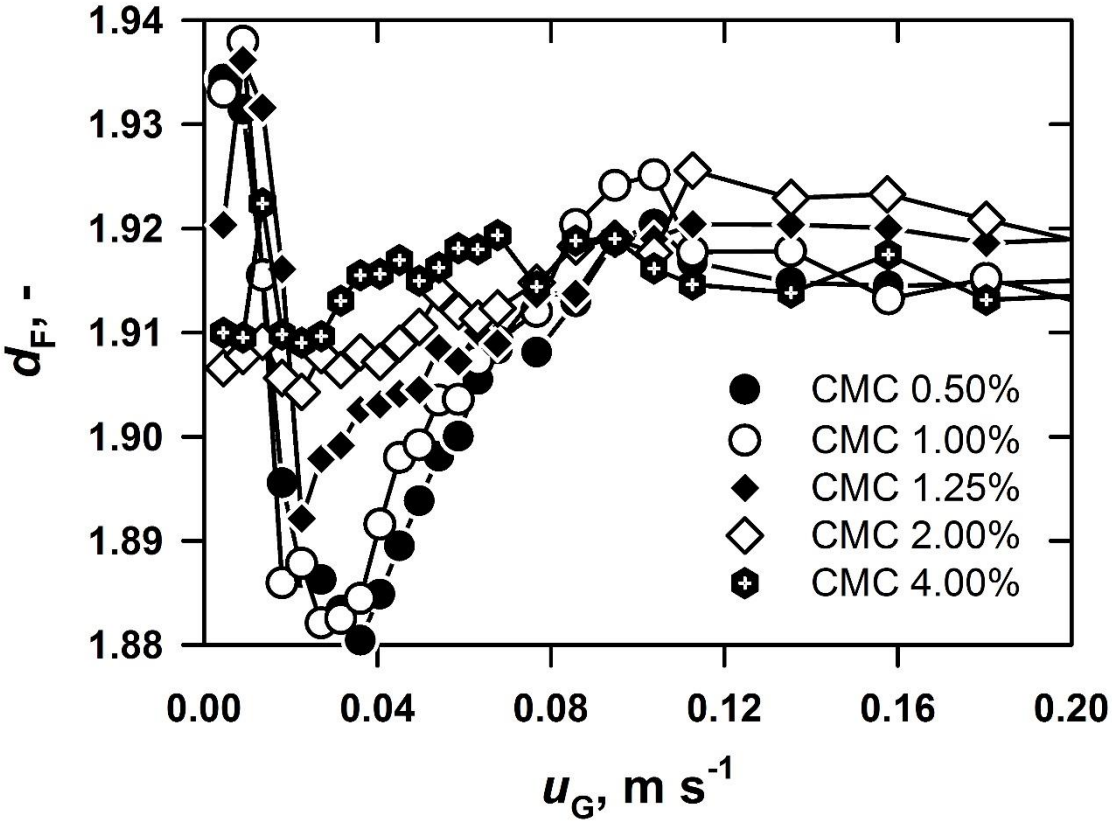

Figure 58: Evolution on the of the fractal dimension with the viscosity (CMC solutions/nitrogen, P = 0.1 MPa, sensor 1, h_0 = 1.50 m).

Figures 59 and 60 illustrate the evolution of the Kolmogorov entropy with the superficial gas velocity at different viscosities. The observations are similar as for the fractal analysis. The Kolmogorov entropy minimum (indicating the main flow transition) is shifted to lower gas velocity as the viscosity is increased.

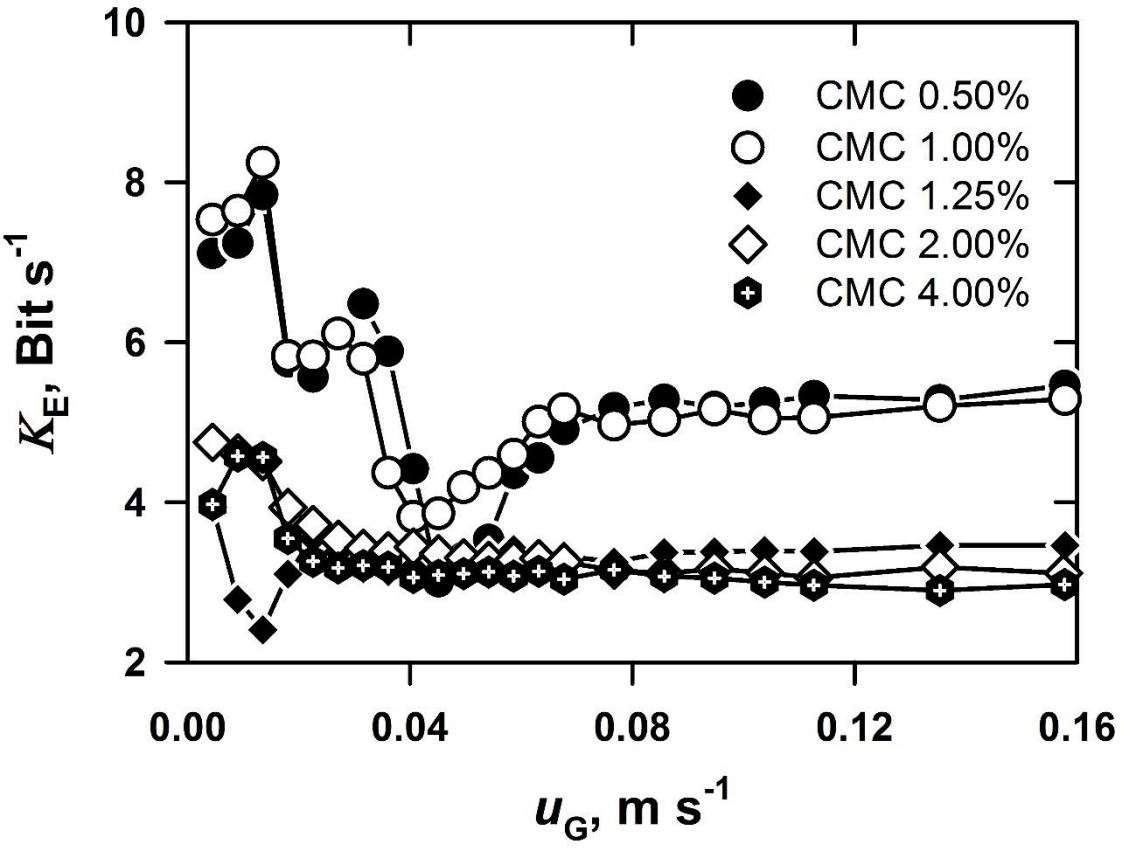

Figure 59: Viscosity effect on the Kolmogorov entropy (P = 0.1 MPa, sensor 2, h_0 = 1.50 m).

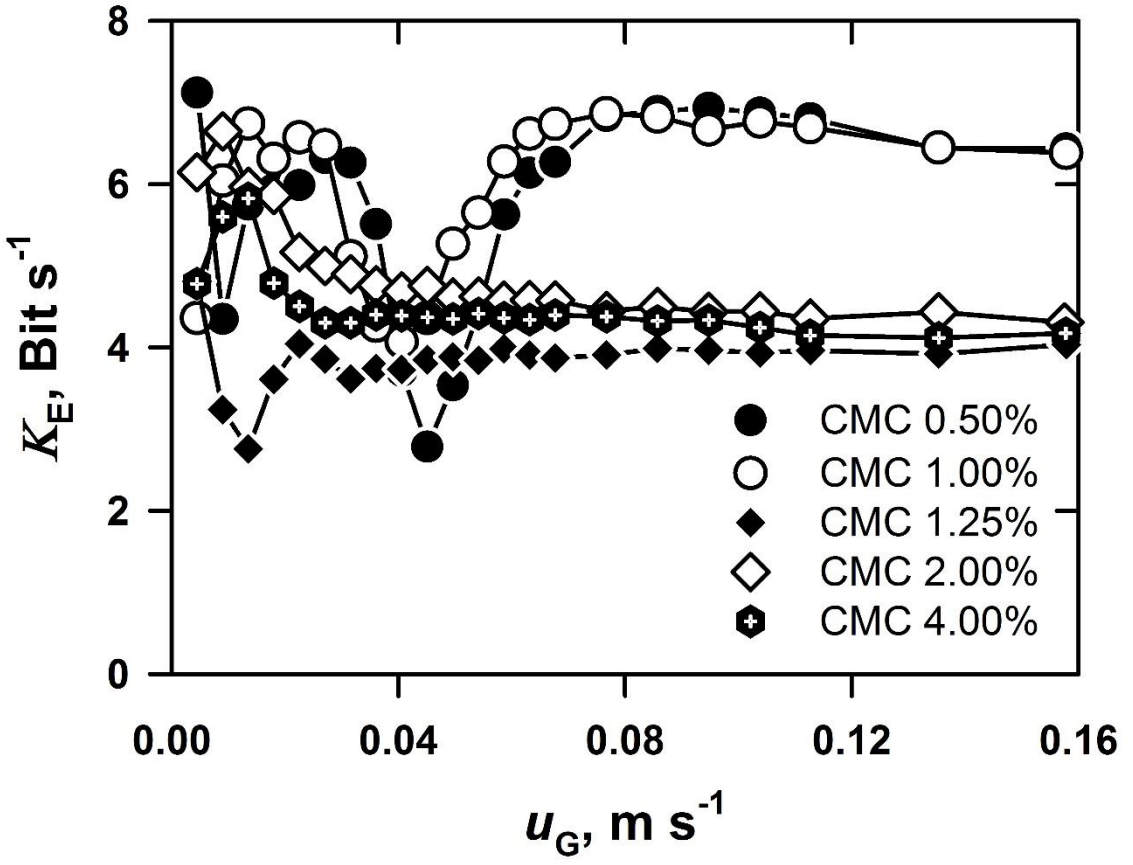

Figure 60: Viscosity effect on the Kolmogorov entropy P = 0.1 MPa, Sensor 3, h_0 = 1.50 m).

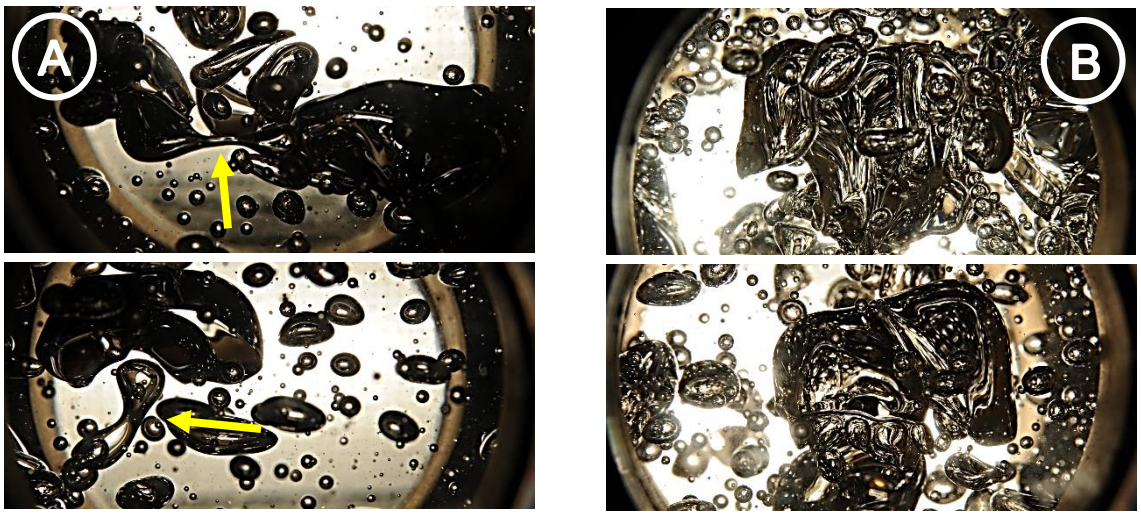

Figure 61: Bubbles photo in (A) Bubble break-up at 0.013 m s^{-1}, (B) Bubbles collision at 0.036 m s^{-1} in MEG/nitrogen.

Figure 61A shows two cases of bubbles in their break-up processes at very low gas velocity whereas Figure 61B shows two cases of colliding bubbles without coalescence at higher gas velocity in ethylene glycol.

Figures 62 and 63 show the evolution of the standard deviation and the average cycle time for the system MEG/nitrogen. At the opposite of the second and third sensors, the first sensor shows at 0.058 m s^{-1} a sudden jump of the standard deviation and a drop of the average cycle time. This suggests the flow of huge gas pockets. The resistance of the liquid to the rise of these large bubbles leads to their break-up into smaller and more stable ones thus the constant evolution observed at higher axial locations (sensors 2 and 3).

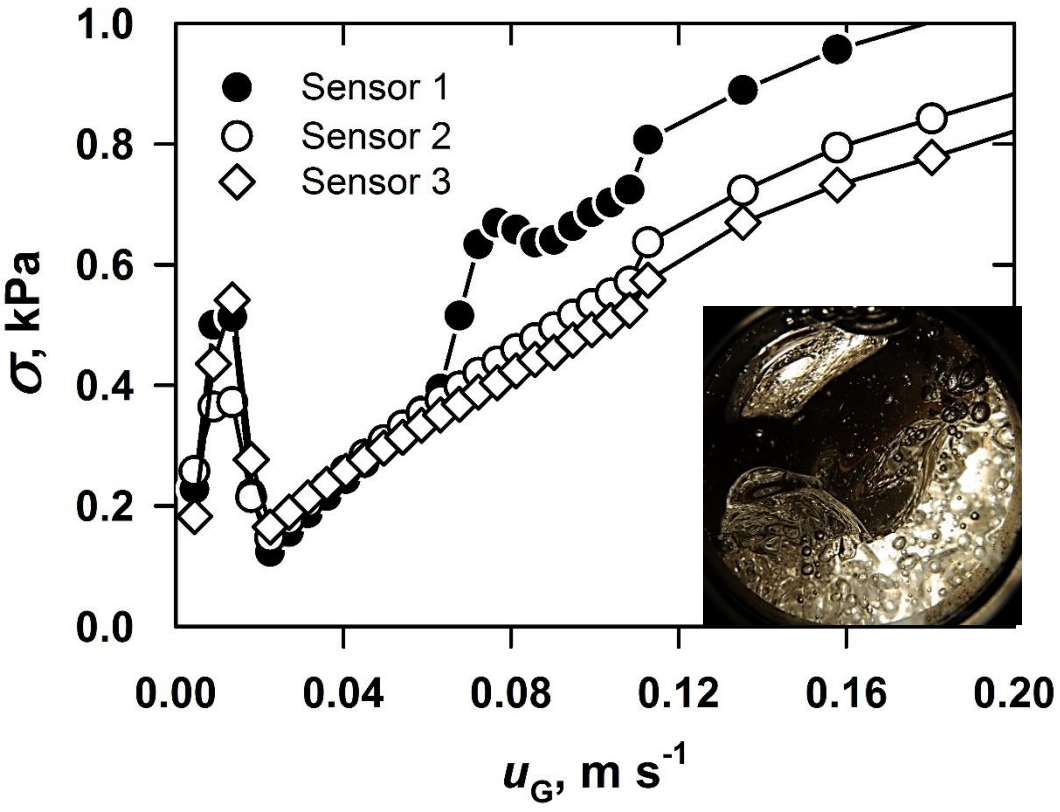

Figure 62: Standard deviation (MEG/nitrogen, P = 0.1 MPa, h_0 = 1.50 m).

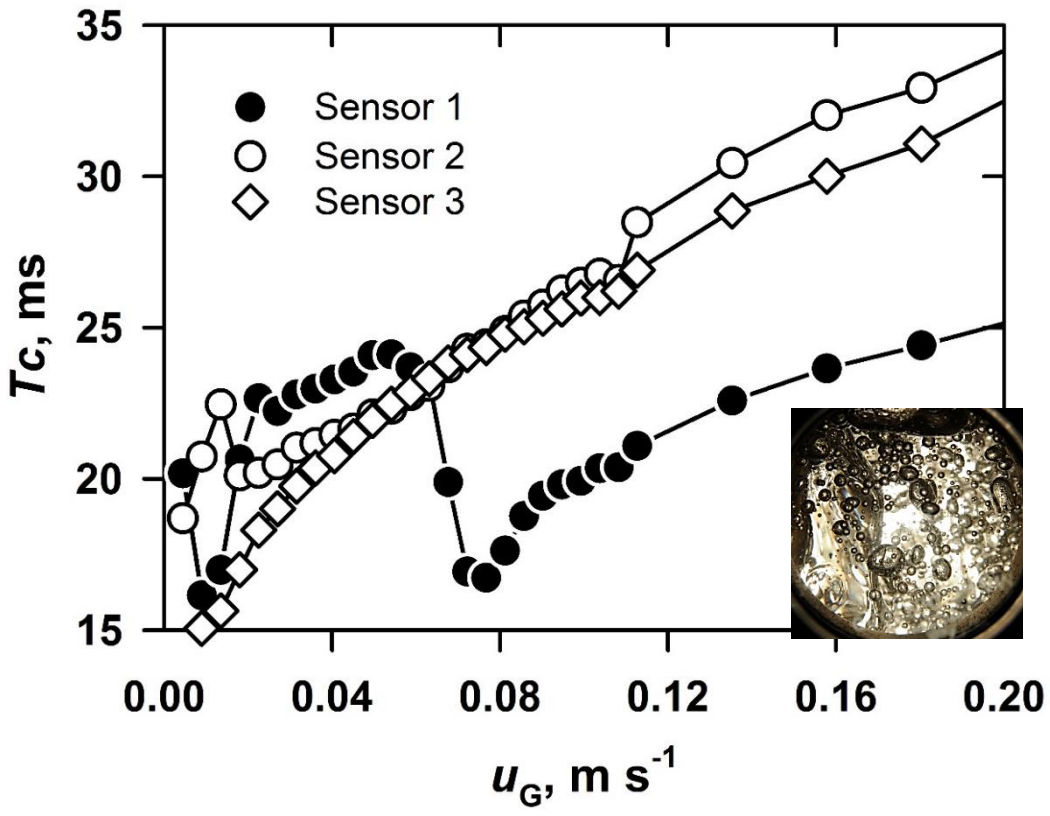

Figure 63: Average cycle time (MEG/nitrogen at P = 0.1 MPa, h_0 = 1.50 m).

Thanks to the critical superficial gas velocities collected from Figures 59 and 60, the viscosity effect on the flow regime boundaries illustrated on Figure 64 could be established.

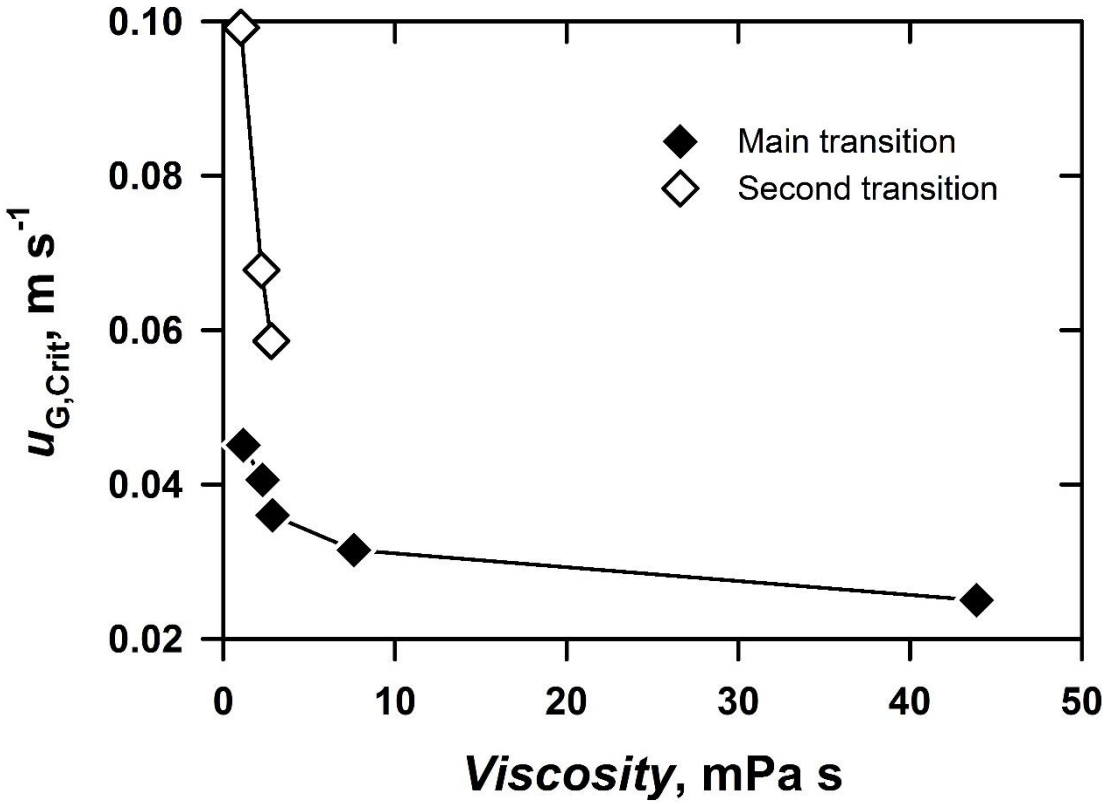

Figure 64: Evolution of the critical velocity with the viscosity (CMC solutions/nitrogene, P = 0.1 MPa, sensor 3, h_0 = 1.50 m).

The increase in viscosity shifts the main transition to lower superficial gas velocity. Then the homogeneous regime completely disappears.

4.2.3 Influence of the pressure

Figure 65 shows the influence of the pressure on the gas hold-up. The increase of the gas hold-up with the pressure is a phenomenon well explained in the literature. LaNauze and Harris (1974) related it to the high frequency at which the bubbles release takes place. The resulting small bubbles have low rise velocities.

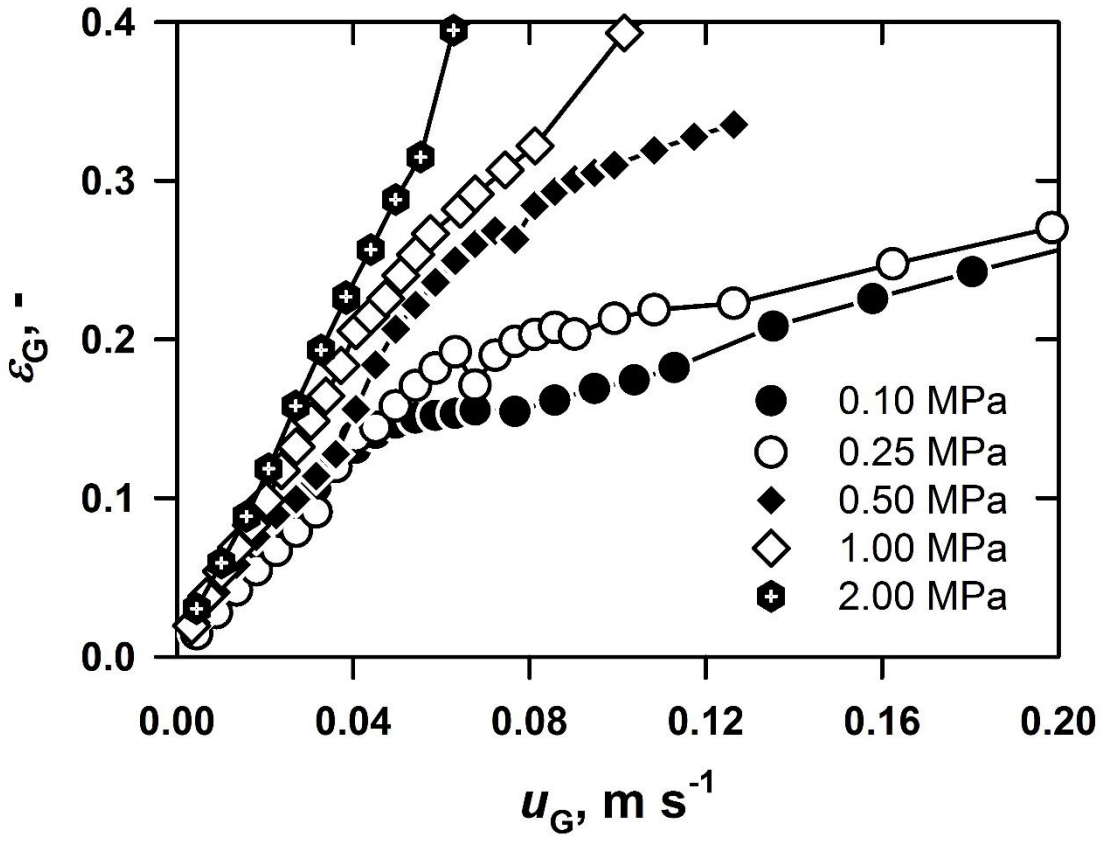

Figure 65: Influence of the pressure on the gas hold-up (water/nitrogen, sensors 2 and 3).

Figure 66 shows the evolution of the Kolmogorov entropy with the gas velocity, depending on the operating pressure. The progressive flattening of the curves with the operating pressure increase is noticed. The Kolmogorov entropy minimum (indicating the main flow transition) is shifted towards higher gas velocities but becomes less sharp. The trend agrees well with the prediction proposed by Reilly et al. (1994).

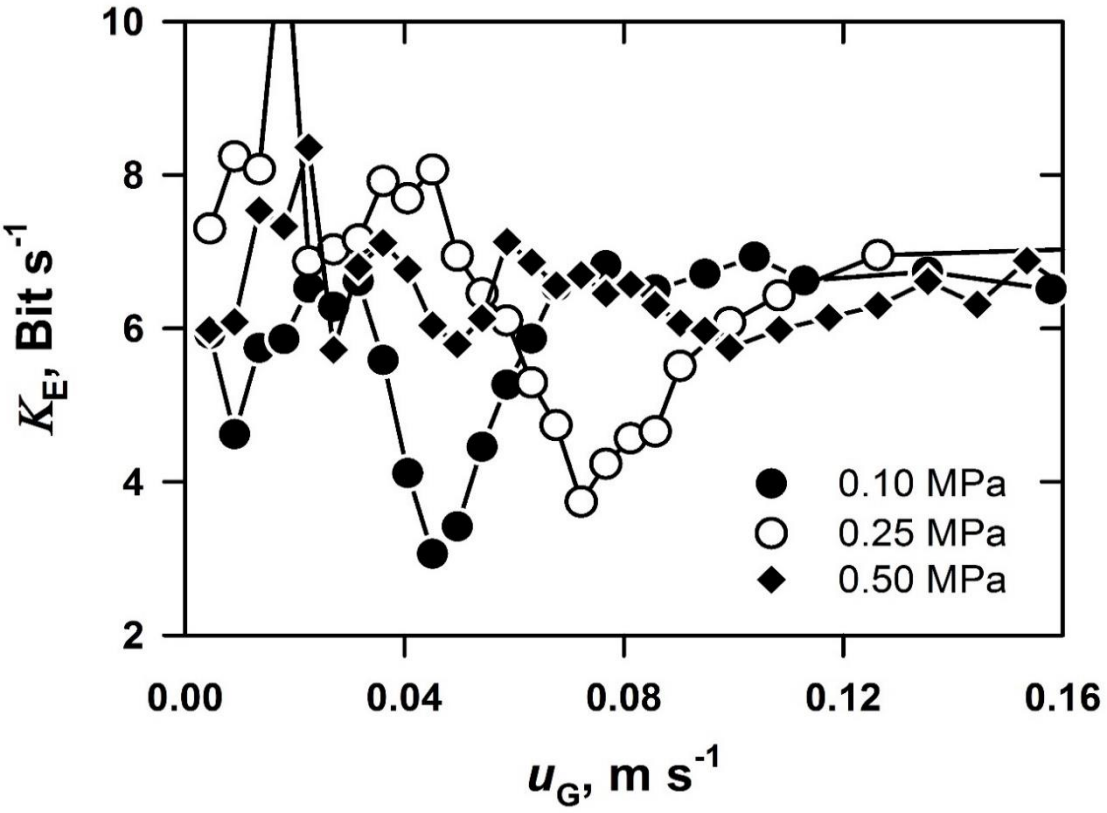

Figure 66: Evolution of the Kolmogorov entropy with the operating pressure (water/nitrogen, sensor 3, h_0 = 1.50 m).

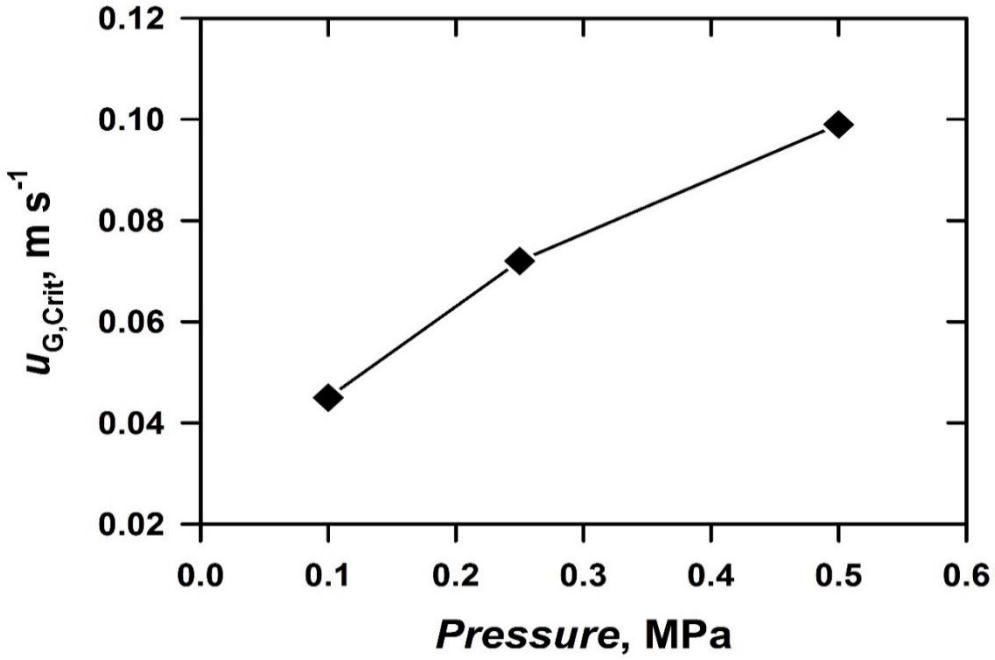

Figure 67: Critical velocity (based on K_E) as a function of the operating pressure (water/nitrogen system, sensor 3, h_0 = 1.50 m).

It is also possible to detect the influence of the operating pressure on the critical velocities for the system toluene/nitrogen.

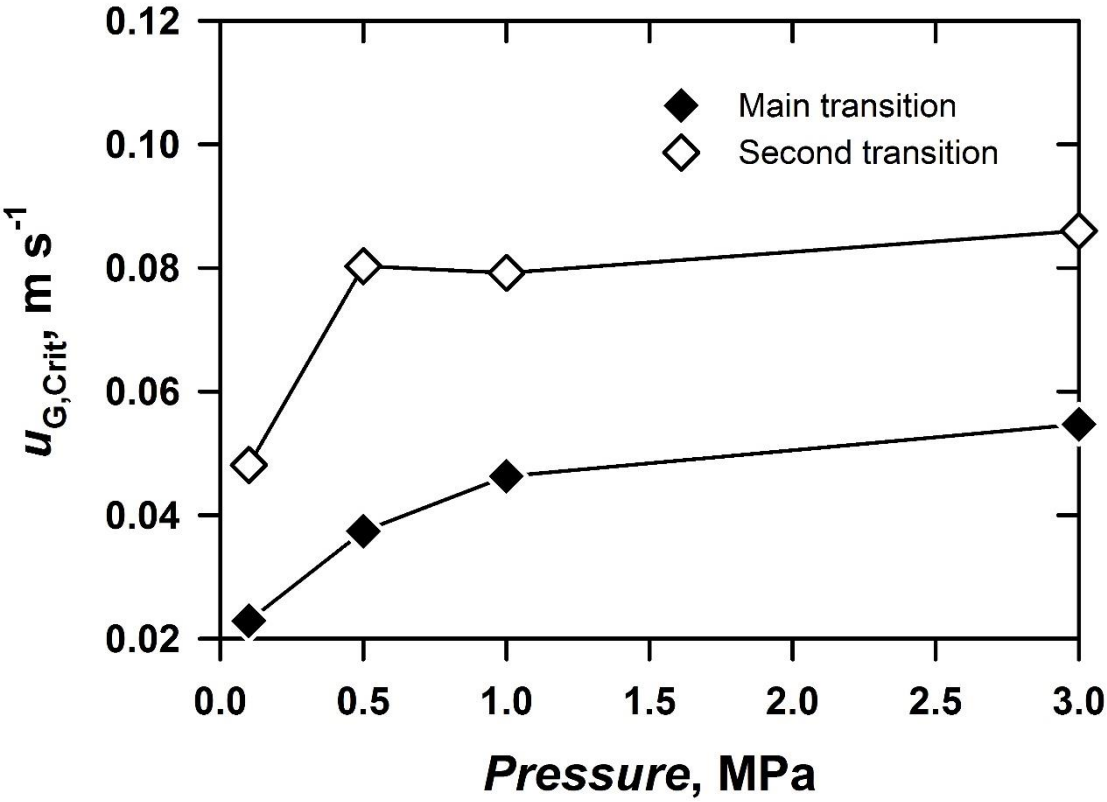

Figure 68: Critical velocity (based on K_E) as a function of the operating pressure (toluene/nitrogen, sensor 2, h_0 = 1.25 m).

Pressure effect in viscous liquid

Figure 69 shows the influence of the pressure on the standard deviation for ethylene glycol solution (16.1 mPa s). As the pressure increases, the boundary intermittent/heterogeneous flow (minimum) is shifted to lower gas velocities values. With the increase of the operating pressure, the pressure in the plenum chamber increases also. The frequency of the gas release increases also as expressed by equation (1). Based on the concept of the critical Weber number (We_{crit} = 2), the critical gas velocity is expected to vary with the gas density to power of -0.5 (cf. chapter 4.1.2 a).

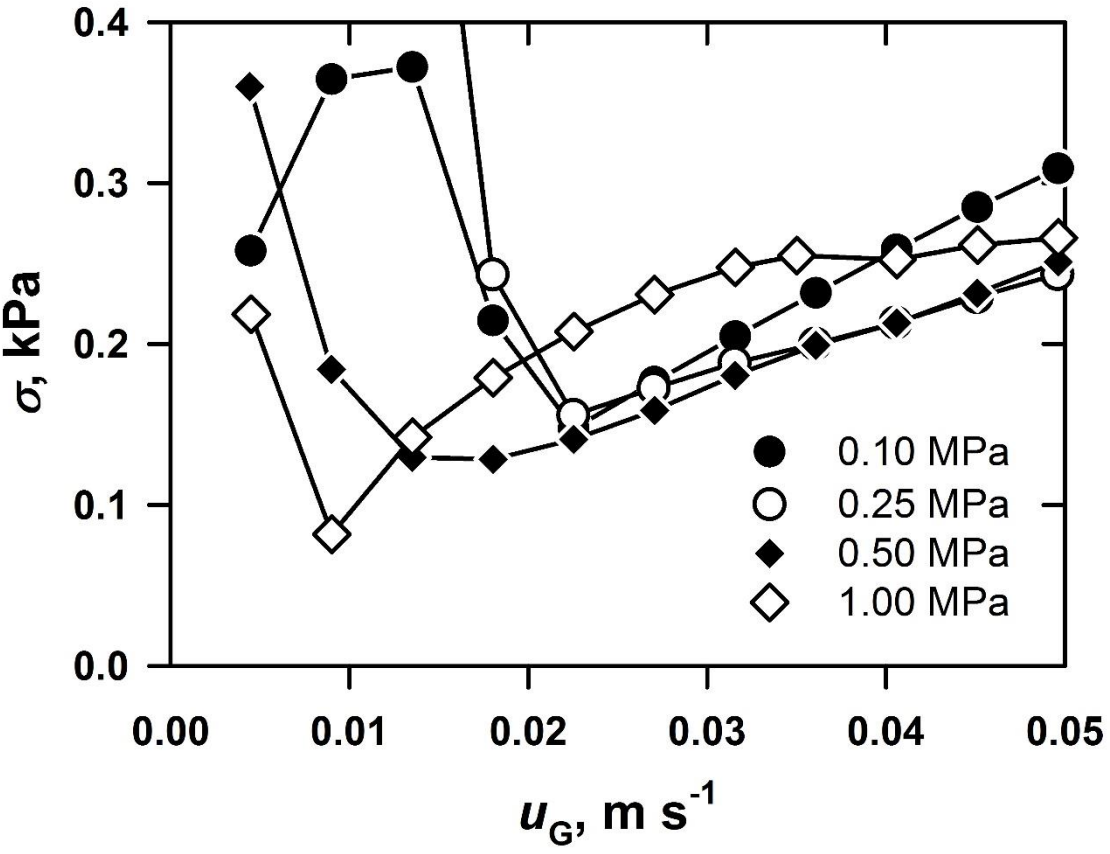

Figure 69: Evolution of the standard deviation with the operating pressure (MEG/nitrogen, sensor 2, h_0 = 1.50 m).

Figure 70 shows two pictures taken at 0.045 m s^{-1} in ethylene glycol, for two different operating pressures. The effect of the pressure on the hydrodynamics is obvious. At 1.00 MPa, the reduction of the bubble size distribution is significant.

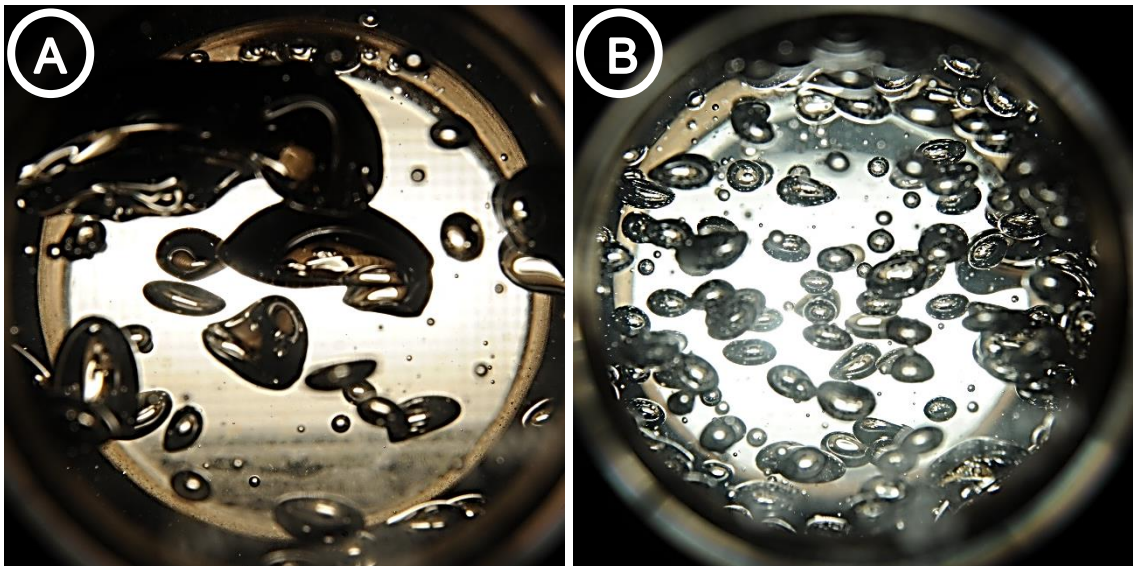

Figure 70: Effect of the pressure on the bubble size distribution at 0.045 m s^{-1} (MEG/nitrogen, A: *P* = 0.10 MPa, B: *P* = 1.00 MPa).

4.3 Pressure sources identification

Figure 71 depicts the PSD graph for the system water/nitrogen at atmospheric conditions for sensor 3. It shows peaks at three different frequencies. A fourth frequency is only detectable with the first sensor. Listed from one to four, these are:

1. Peaks at frequencies around 4 s^{-1} are always reported in the literature and detectable by all three sensors. The peaks are completely absent in the intermittent and homogeneous flow regimes. From the first transition point the amplitude increases significantly with the gas velocity and becomes the highest of the graph.

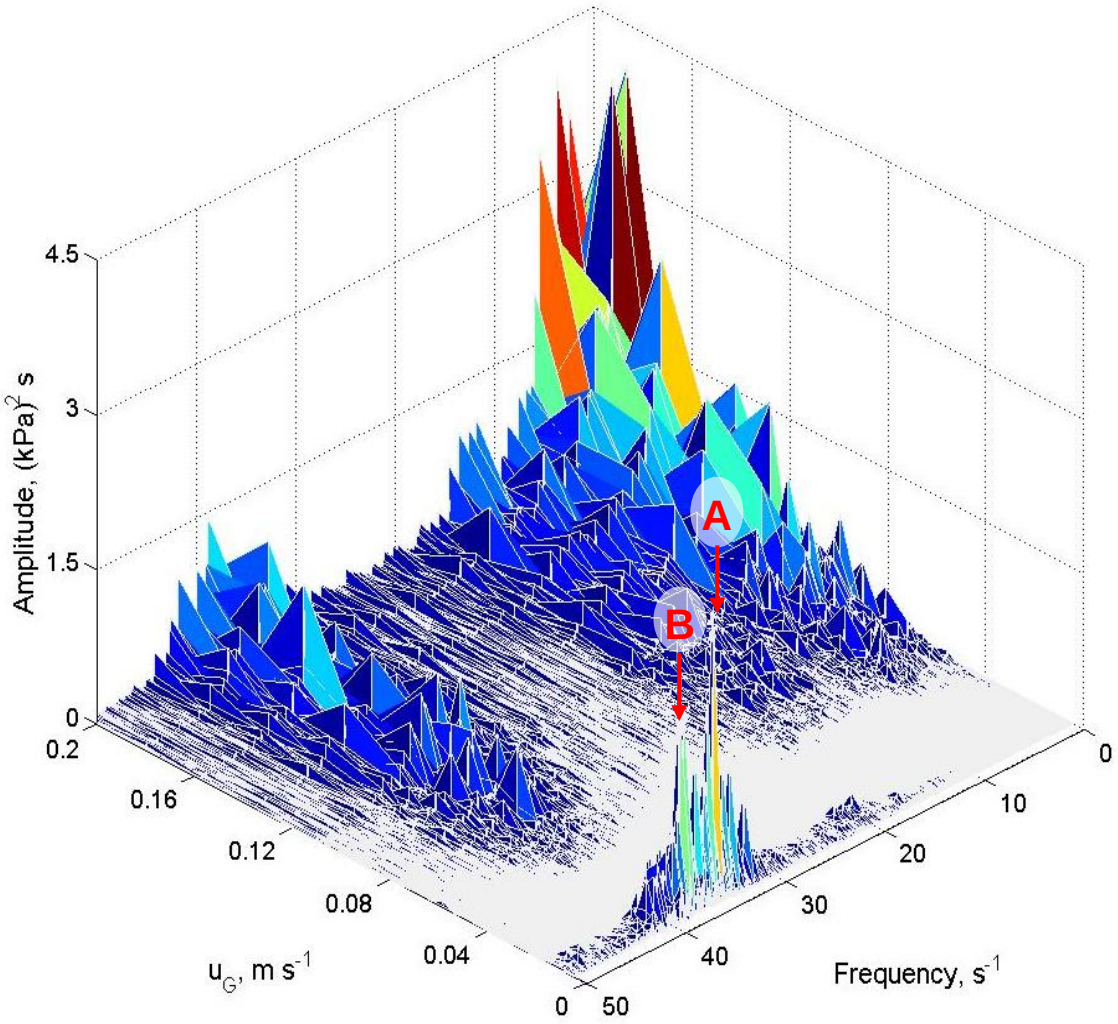

Figure 71: Power spectral density as a function of the superficial gas velocity (water/nitrogen, *P* = 0.1 MPa, sensor 3).

2. At frequencies around 13 s^{-1}, peaks are only detectable by the sensors 2 and 3. No peaks appear in the intermittent and homogeneous flow regimes. The amplitude is low in the transition regime; it increases with the gas velocity in the heterogeneous regime but at a noticeably lower extend than for (1).

3. At frequencies around 35 s^{-1}, peaks are only detectable by the sensors 2 and 3. In the intermittent flow regime, the signal appears split into two peaks of high but different amplitudes. Peaks are completely missing in the homogeneous flow regime. In the transition flow regime, peaks appear with low amplitudes. In the heterogeneous regime, the amplitudes are higher and increase slightly with the gas velocity. Peaks at similarly high frequencies are seldom reported in the literature, since the PFS is often filtered, cancelling the frequencies above 20 s^{-1}.

4. At slightly higher frequencies around 40 s^{-1}, peaks were only detectable by the sensor 1. In the intermittent flow regime, the signal appears split into two peaks of high and equal amplitude or spread on a wide region. Peaks at 40 s^{-1} are completely missing in the homogeneous flow regime. In the transition flow regime peaks appear with low and constant amplitude. In the heterogeneous regime, the amplitudes are higher and increase slightly with the gas velocity.

For the identification of the pressure sources, the evolution of the PSD as a function of superficial gas velocity is analysed, varying the following four parameters:

- clear liquid height

- sensor axial location

- liquid viscosity

- operating pressure

4.3.1 The liquid bed fluctuation

The liquid bed fluctuation is mainly the cumulated consequence of the bubbles formation and the bubbles eruption. Although these two phenomena take place simultaneously provoking changes of the mixing volume, they have opposite effects on the liquid height. At one hand, the bubbles formation process tends to increase continuously, uniformly and smoothly the liquid height because of the constant gas flow (Q) within the system. At the other hand, the bubbles eruption (gas flow out from the system) provokes the decrease of the clear liquid height. But, depending on the prevailing regime, this process can also be characterized as smooth or as discontinuous, non-uniform and abrupt. Indeed, while the liquid height remains almost constant in the homogeneous regime, the eruption of large bubbles in the heterogeneous regime causes significant fluctuations of the level.

Figure 72 shows the influence of the sensor axial location on the Peak 1. It shows clearly that distancing the sensor from the sparger provokes a decrease in amplitude of the peak type 1. This is in agreement with the results reported by Drahoš et al. (1991). But as depicted on Figure 73, an increase of the clear liquid height provokes an increase in amplitude of the Peak 1, independent from the sensor position. An increase of the clear liquid height (of the order of 16%) cannot lead to the increase in amplitude of the peak corresponding to the bubbles formation process as Drahoš et al. (1991) suggested. This second argument proves that the peak type 1 cannot be attributed the bubbles formation process.

Moreover, because of the hindrance caused by the other bubbles motion, the amplitude of the peak due to the bubbles formation should decrease with the axial location. At a critical distance from the sparger, the bubbles formation process should no more be detectable. But the peak type 1 is always present, regardless of the distance of the sensor from the sparger. At 1.20 m above the sparger (see Figure 72), it still appears clearly. This last argument excludes definitely the possibility for the peak type 1 to stand for the bubbles formation process. A phenomenon involving the whole liquid mass should be considered.

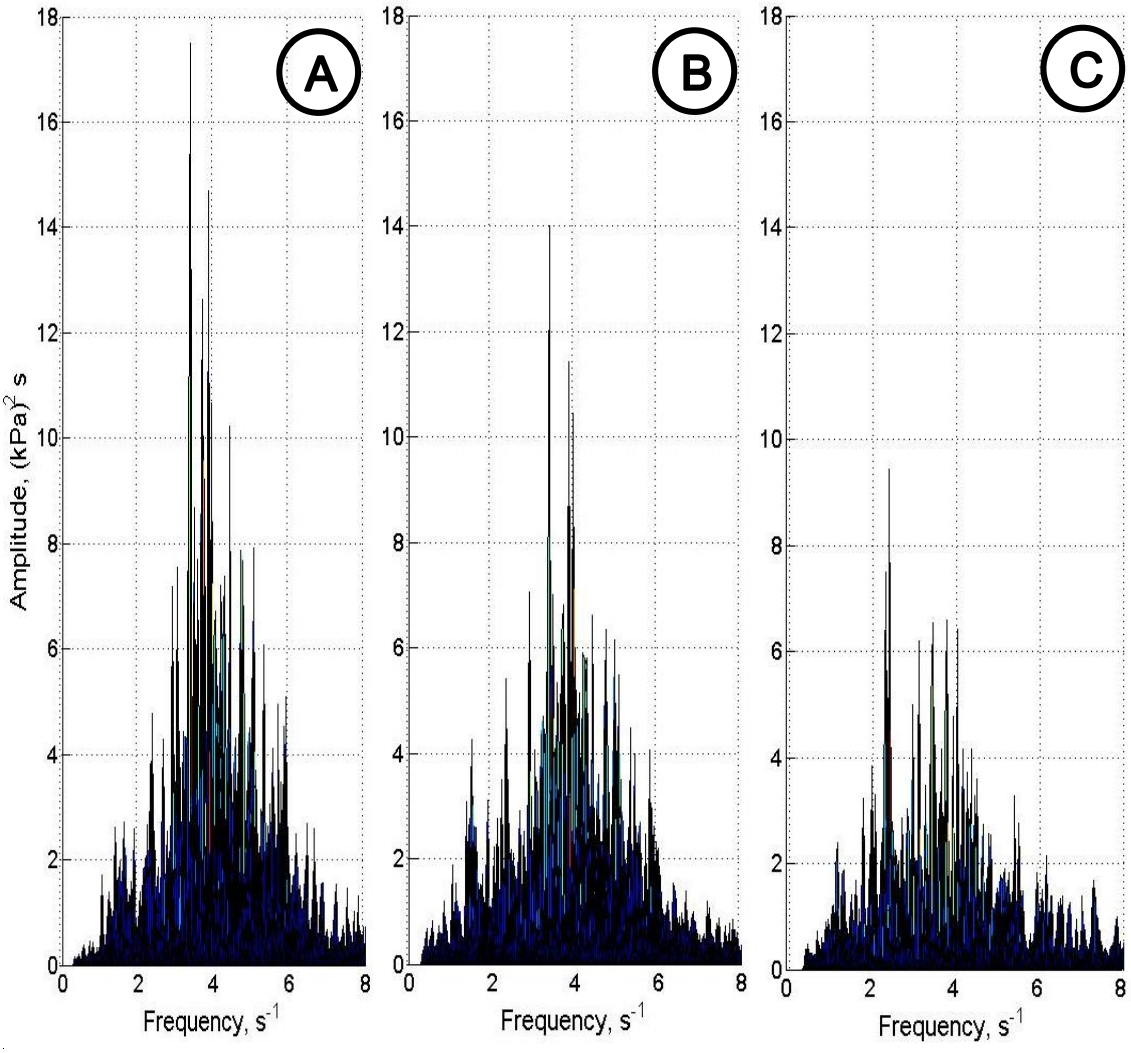

Figure 72: Influence of the sensor axial location on the peak type 1 amplitude, (A) *h* = 0 m, (B) *h* = 0.65 m, (C) *h* = 1.20 (MEG/nitrogen, *P* = 0.1 MPa, h_0 = 1.50 m).

From Figure 72 and 73 it is noticed that the amplitude of the peak type 1 is a function of the liquid amount above the sensor. Distancing the sensor from the sparger, reduces also the volume of liquid above it, leading to a decrease of the Peak 1 amplitude.

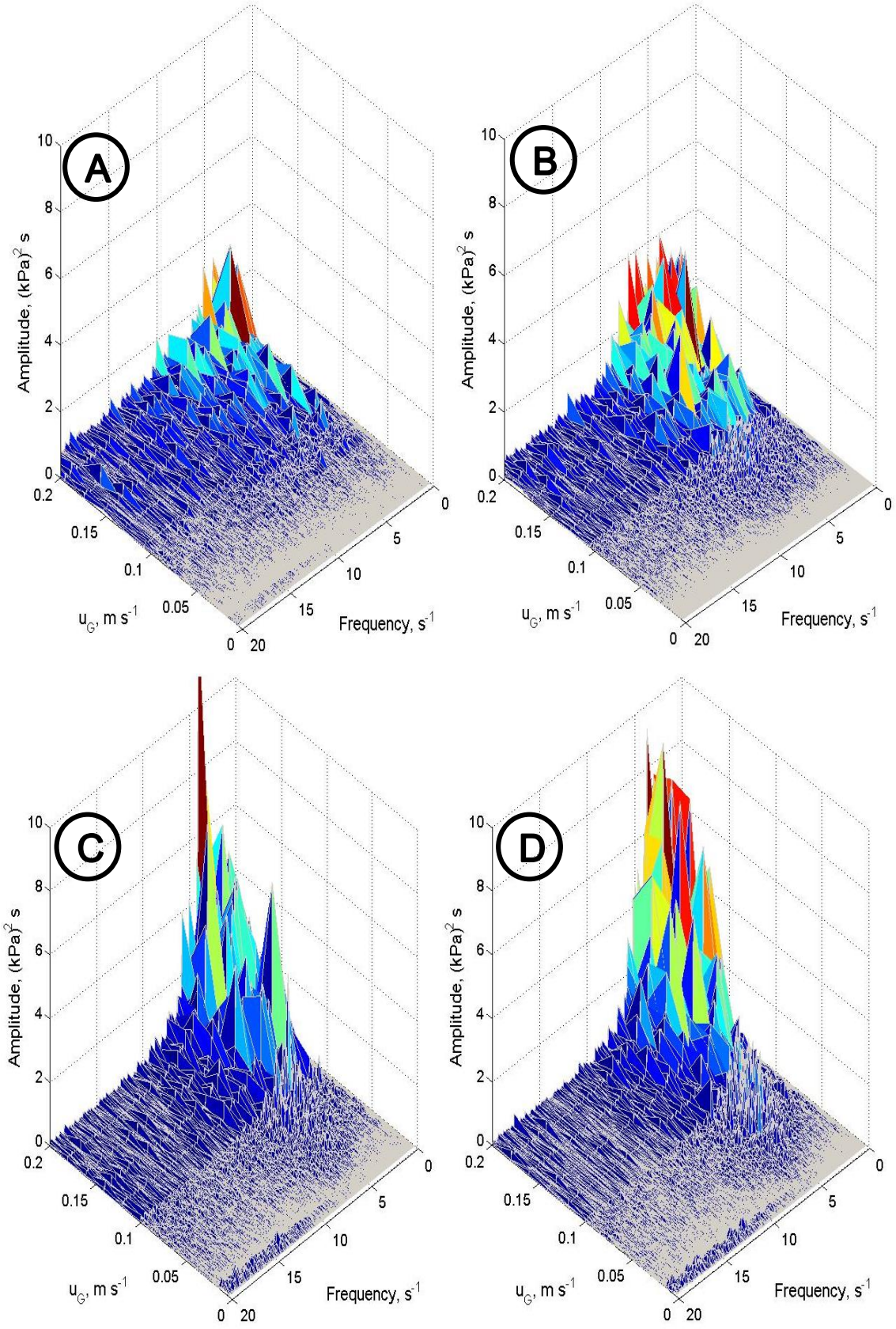

Figure 73: Influence of the clear liquid height on peak type 1 (A) h_0 = 1.00 m, (B) h_0 = 1.25 m, (C) h_0 = 1.50 m, (D) h_0 = 1.75 m (MEG/nitrogen, P = 0.1 MPa, sensor 2).

From these observations, it can be concluded that the Peak 1 represents the bed liquid fluctuation. This assumption is reinforced by the study of the coherence function. A highly coherence is observed at this frequency for the three sensors. Such a high correlated phenomenon can only be due to a process in which the whole liquid is simultaneously involved in.

4.3.2 The bubbles eruption process

The bubbles eruption takes place continuously at the liquid surface. The shock wave provoked by the bubble eruption is mainly due to the cavity collapse as explained in part 2.2.6. Thus, bringing the sensor closer to the surface should induce an increase of the amplitude of the peak corresponding to bubbles eruption. Inversely, the distancing of the sensor from the surface should lead to the amplitude decrease of that peak.

Figures 74 and 75 show the influence of the clear liquid height and the influence of the sensor axial location, respectively, on the peak type 2 at about 13 s^{-1}. It is noticed that the amplitude decreases with the clear liquid height (see Figure 74) but increases with the sensor axial location (see Figure 75). It means that getting the sensor closer to the top or reducing the liquid amount in the column (for a fixed axial location) increases the detected amplitude. These two observations are good evidence that the pressure fluctuation responsible of the peak type 2 takes it source at the surface of the liquid.

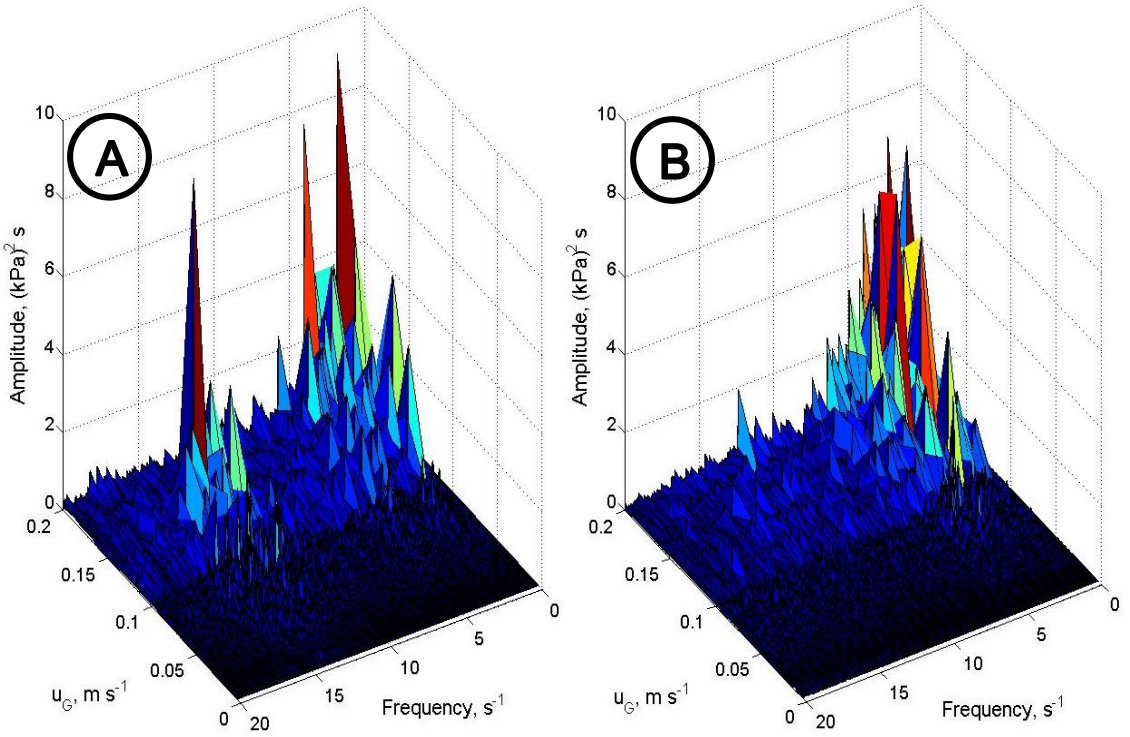

Figure 74: Influence of the clear liquid height on the peak type 2 (13 s^{-1}) with (A) h_0 = 1.25 m, (B) h_0 = 1.50 m (MEG/nitrogen, sensor 3).

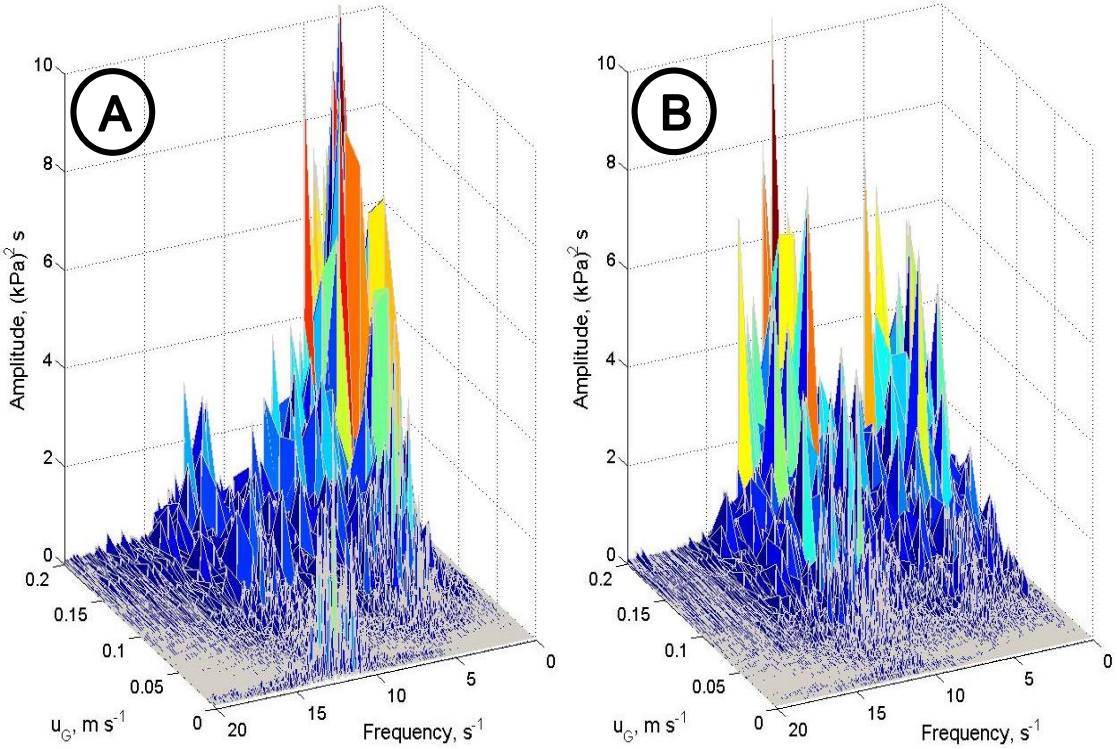

Figure 75: Influence of the sensor axial location on peak type 2 (13 s^{-1}) with (A) sensor 2, (B) sensor 3 (1.25% CMC solution/nitrogen, P = 0.1 MPa).

At equal gas velocity, the increase of the liquid viscosity leads to the formation of fewer bubbles with larger dimension. Figure 76 shows the influence of the viscosity on the bubble size distribution. At high viscosity, larger bubbles tend to be formed.

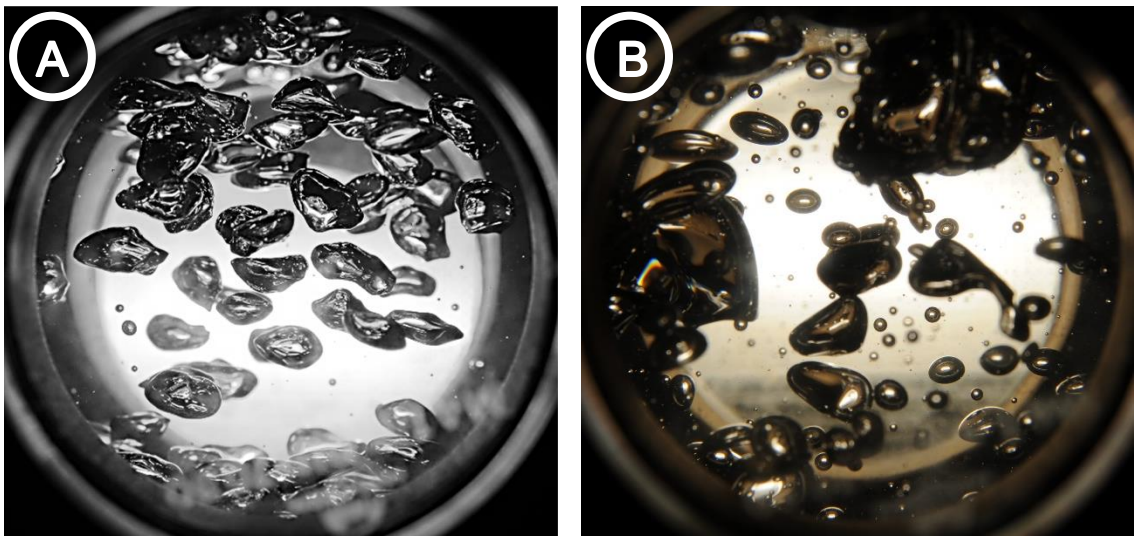

Figure 76: Influence of the viscosity on the bubble size distribution, P = 0.01 MPa, u_G = 0.009 m s^{-1}, (A) water, (B) MEG.

Figure 77 shows the influence of the viscosity on the peak type 2. Two observations can be made:

- The increase of the viscosity shifts peak to lower frequency by up to 5 s^{-1}. The peaks fuse progressively with the peak of type 1.

- The amplitude increases with the liquid viscosity. It is obvious that as the viscosity increases, large bubbles are formed (see Figure 76) and the film break-up becomes also more difficult. Thus, the shock wave caused by the walls collapse prior to the jet formation is also supposed to be stronger.

According to all the preceding analysis, it can be concluded that the peak type 2 stands for the bubbles eruption process. The absence of the peak type 2 at the bottom of the column (sensor 1, see Figure 83) confirms this idea.

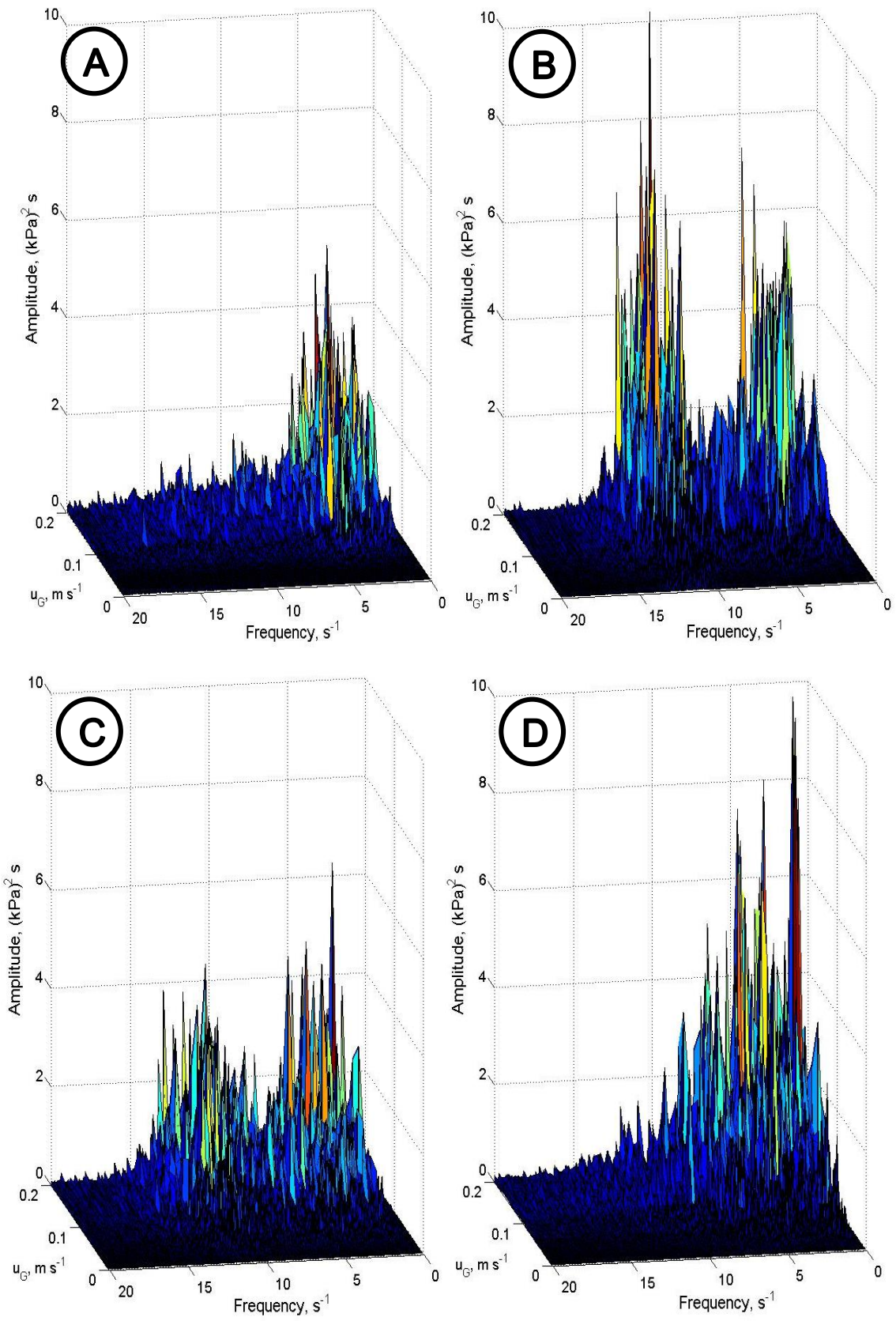

Figure 77: Influence of the viscosity on the peak type 2, (A) CMC 0.5%, (B) CMC1.0%, (C) CMC 2.0%, (D) CMC 4.0%for (*P* = 0.1 MPa, sensor 3).

4.3.3 The bubbles oscillation

Bubbles are highly deformable and often oscillate (Abdulmouti, 2014). The bubbles oscillation is due to the resistance of the liquid to the bubbles rise (see part 2.2). During their rise in water, bubbles of diameter greater than 3 mm may oscillate. Figure 78A shows evidence of these vibrations called bubble shape oscillation by Veldhuis et al. (2008). In water (see Figure 78A) the bubbles surface is wavy whereas in ethylene glycol (see Figure 78B) it remains smooth. The higher the viscosity of the liquid, the lower the bubbles oscillation will be.

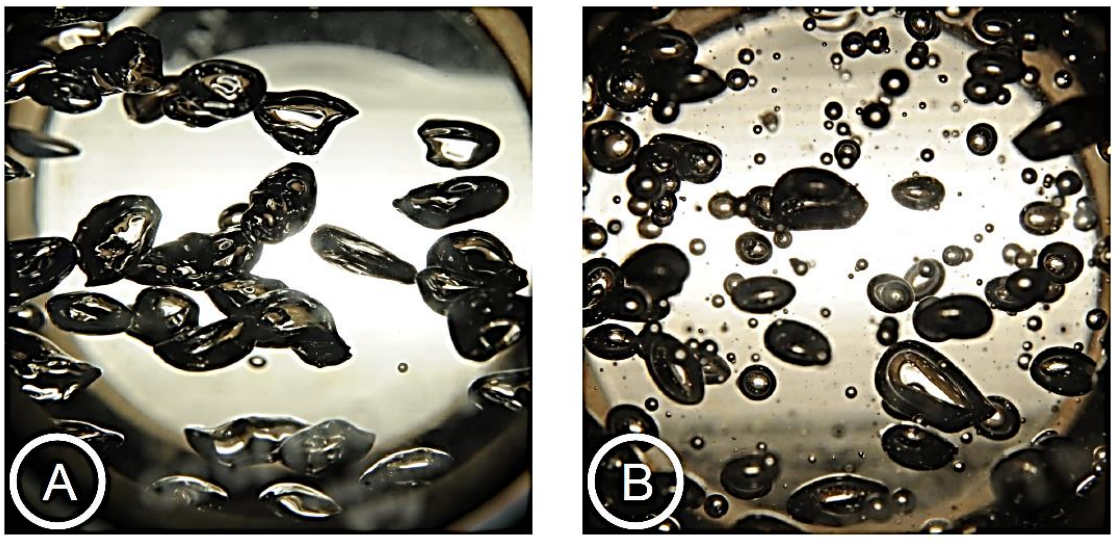

Figure 78: Bubbles shape vibration (A) water/nitrogen, (B) MEG/nitrogen (*P* = 0.1 MPa).

When operating at high pressure in the heterogeneous regime, the bubbles are more spherical and have a smaller dimension, narrow size distribution and a dense space occupation as it can be noticed on Figure 79B. These small bubbles have a lower tendency to vibrate.

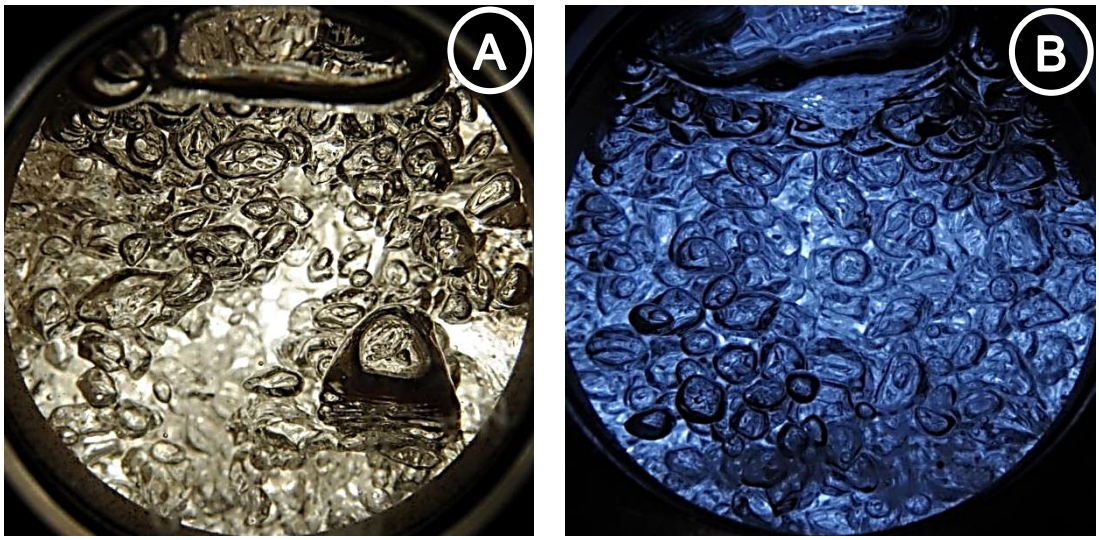

Figure 79: Bubbles shape vibration at u_G = 0.12 m s^{-1}, (A) P = 0.1 MPa and (B) P = 0.5 MPa (water/nitrogen).

When the gas density or the liquid viscosity is increased, the progressive disappearance of the peak type 3 at 35 s^{-1} is clearly noticed. Figure 80 shows that the amplitude decreases with the increase of the operating pressure and is spread on a larger frequency range. Similarly, as depicted on Figure 81, the peak type 3 amplitude decreases with the viscosity increase, up to the complete disappearance.

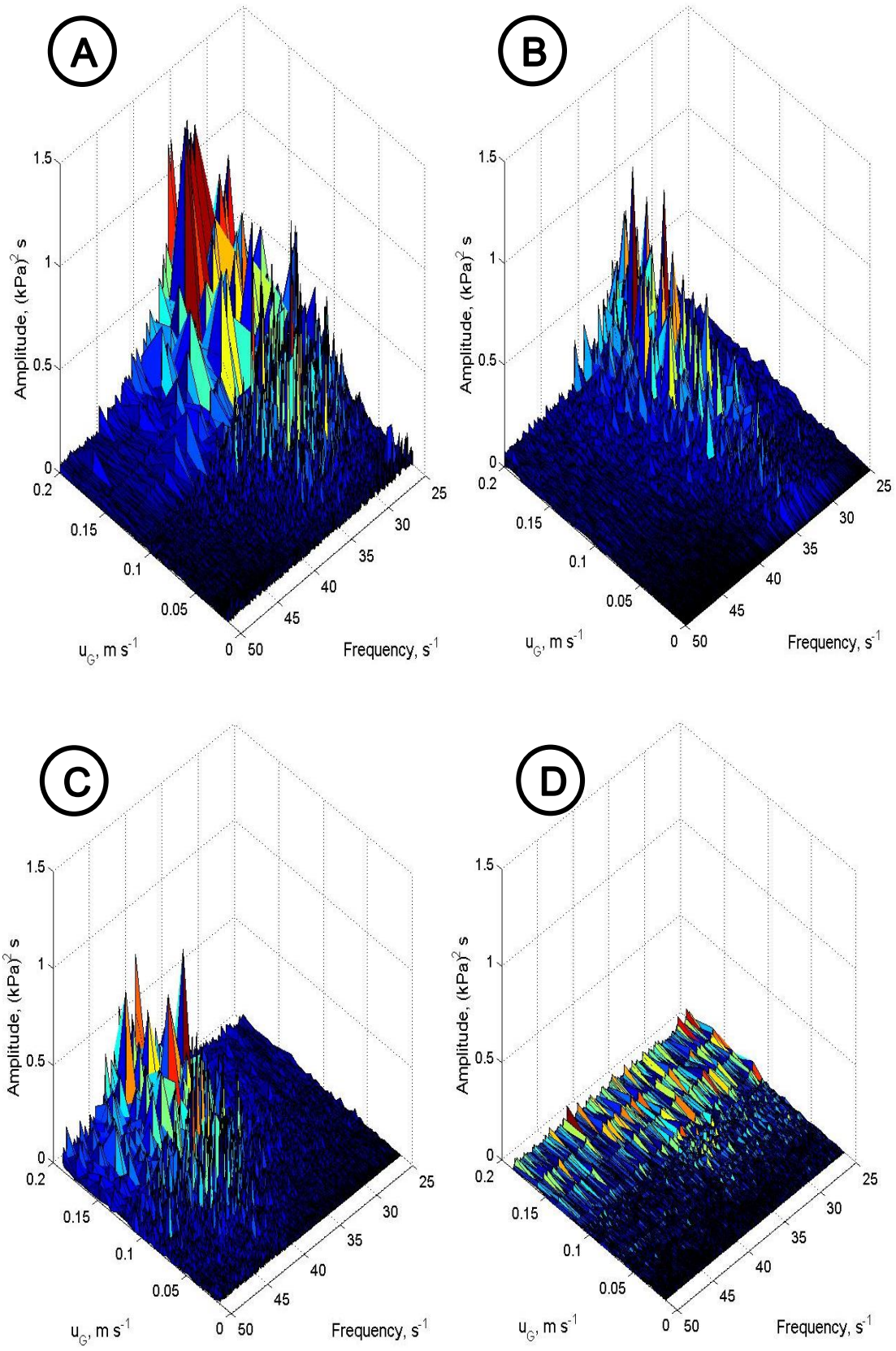

Figure 80: Influence of the pressure on the peak type 3 with *P* = (A) 0.1 MPa, (B) 0.25 MPa, (C) 0.50 MPa and (D) 1.00 MPa (MEG/nitrogen, sensor 2).

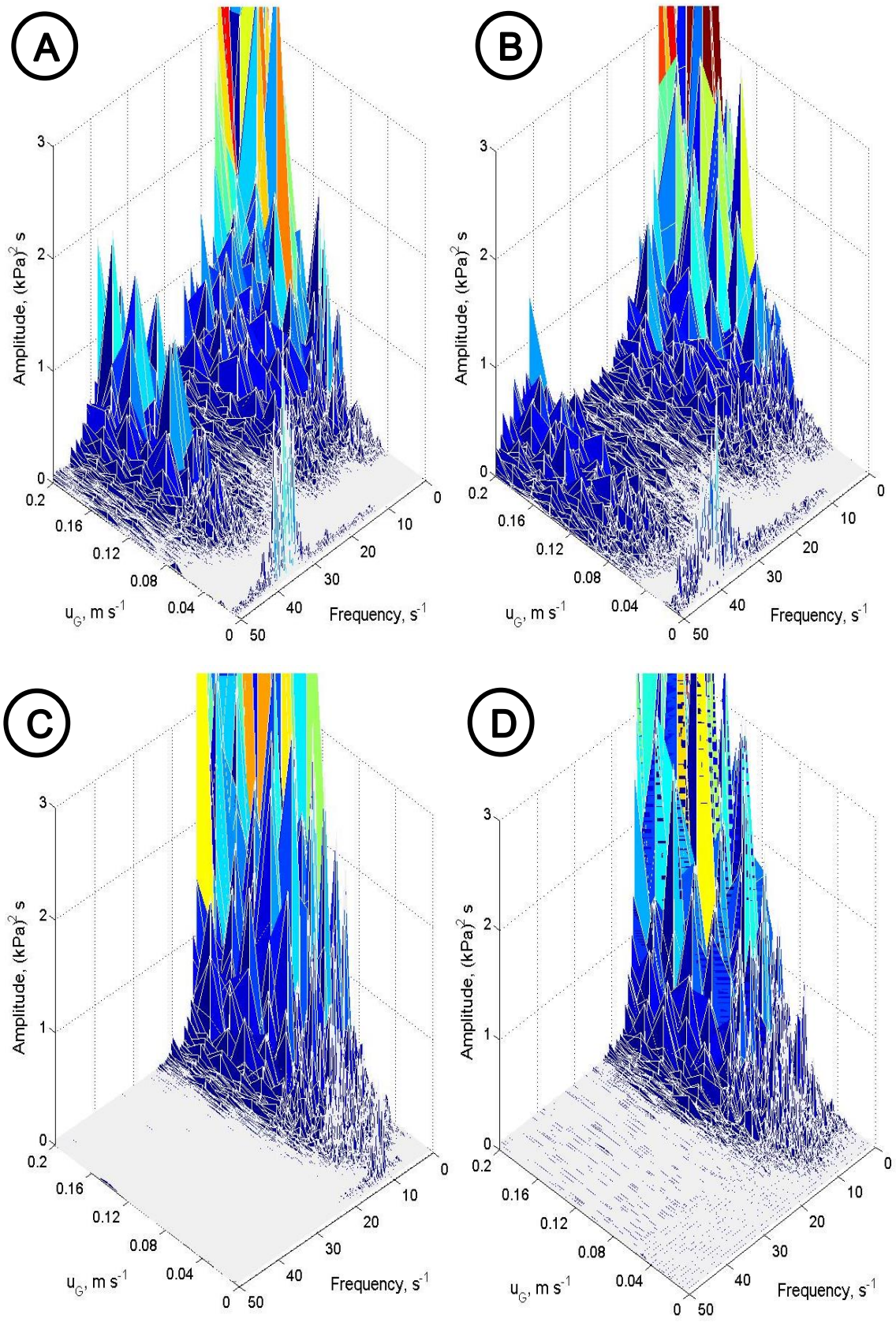

Figure 81: Influence of the viscosity on the peak type 3, CMC concentrations: (A) 0.5%, (B) 1.0%, (C) 1.25 %, (D) 2.0% (CMC solutions/nitrogen, sensor 3).

In the homogeneous regime the flowing bubbles oscillate as well. The total absence of peaks (see Figures 38 and 71) denotes an amorphous structure of the flow or a single phenomenon (or frequency) taking place. Figure 82 shows a sample of the PFS for the two upper sensors in the homogeneous regime. It depicts a sinusoidal curve. The signals have about 35 cycles which corresponds to the frequency of the peak type 3.

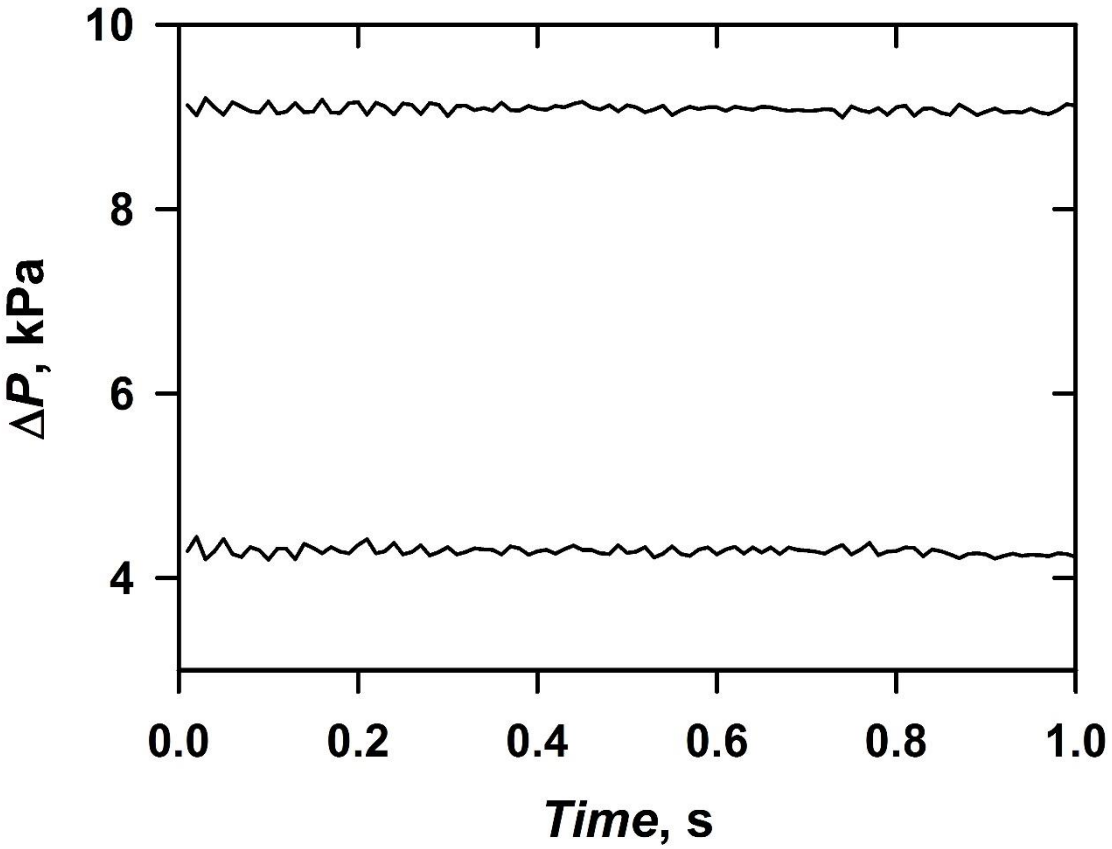

Figure 82: Samples of the pressure fluctuation signal in the homogeneous regime (water/nitrogen, *P* = 0.1 MPa, Sensors 2 and 3).

At intermittent flow the size distribution of the bubbles is narrow but two types of bubbles can be observed (Abdulmouti, 2014):

A- The leading bubbles belong to the front side of the bubbles coat. They are subject to a high initial resistance of the liquid and represent the smaller fraction of bubbles.

B- The trailing bubbles come after the front layer of the leading bubbles. They are submitted to a lower resistance and represent the larger fraction.

These two vibrating states of the bubbles explain the split of the type 3 peaks in the intermittent flow regime. Among both peaks, the peak 3A has the higher amplitude and the lower frequency. It corresponds to the trailing bubbles which represent the higher fraction (correlated here to the amplitude) but face the lower resistance (thus the lower frequency). Similarly, the peak 3B will then be attributed to the leading bubbles because of the higher frequency (higher resistance) and the lower amplitude (smaller bubbles fraction).

At last, the liquid vibration induced by the bubbles oscillation is specific both to the liquid properties and the bubbles size. The bubbles interactions lead to a wide bubble size distribution. The break-up leads to smaller bubbles with vibration frequency higher than the mother bubbles whereas the coalescence leads to the appearance of bigger bubbles with vibration of lower frequency than their mother bubbles. Thus, with increasing gas velocity, the type 3 peaks appears in a wider frequency range.

4.3.4 The bubbles formation process

The amplitude of the vibration due to the bubbles formation should decrease with the sensor axial location *h*.

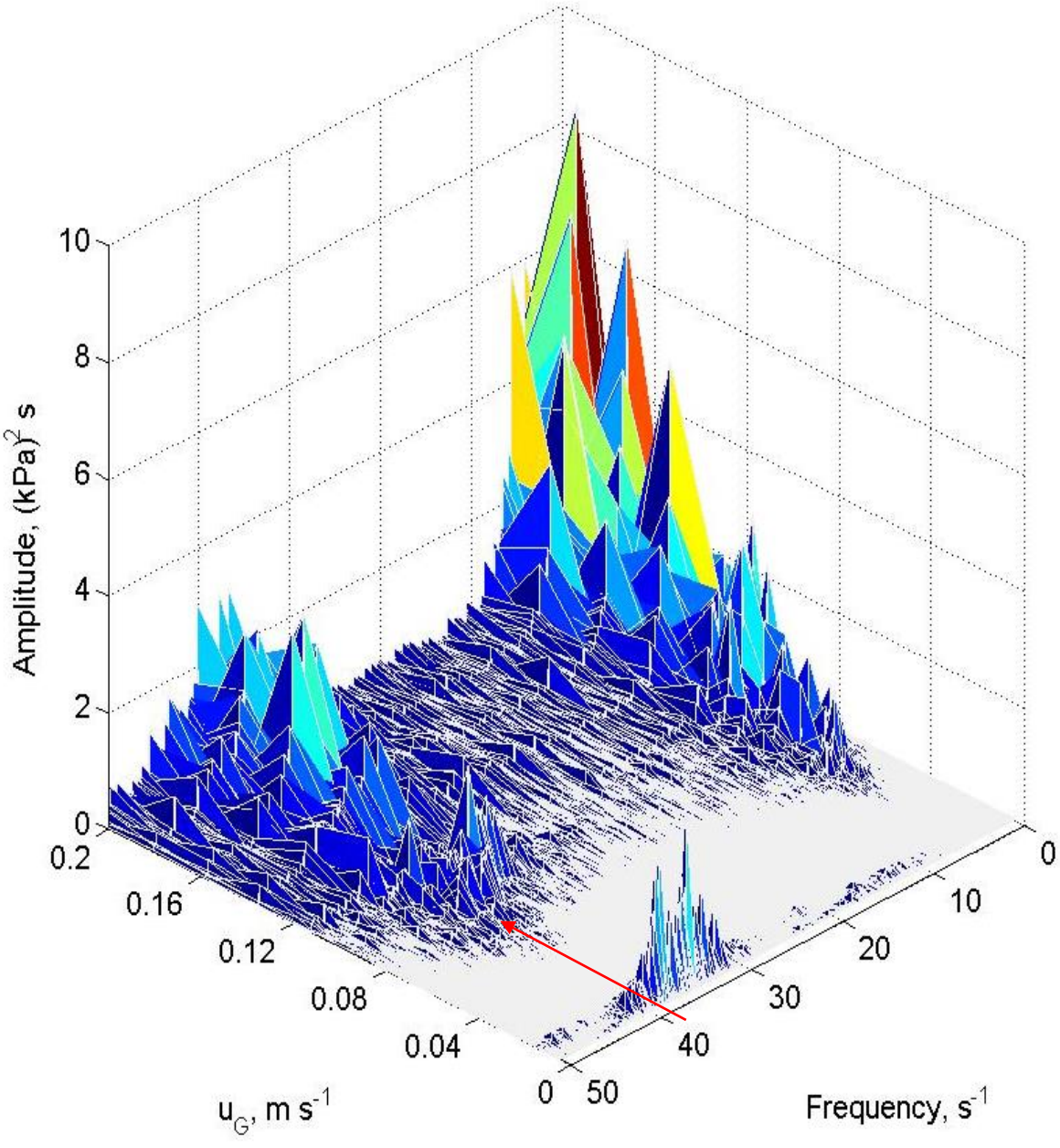

Figure 83: Power spectral density at the gas sparger (water/nitrogen, *P* = 0.1 MPa, sensor 1).

The peak type 4 at frequencies of about 39 s^{-1} is specific to the first sensor. It has a frequency slightly higher than the bubbles oscillation. At higher axial position it does not appear at all, at the difference of the peak type 3 which appears at the same frequency of 35 s^{-1} for the sensors 2 and 3.

Since the bubbles have to overcome the initial resistance due to the liquid, we can assume that the vibration caused by the bubbles formation is close but higher than the vibration caused later by the flow of the formed bubbles. Figure 83 shows of the peak type 4 for the system water/nitrogen.

Figure 84 shows the influence of the viscosity on the peak type 4. The viscosity increase shifts the peaks to lower frequency. This observation is an agreement with the results reported by Park et al. (2001). It is obvious that the bubble size increases with the liquid viscosity. The decrease of the frequency is then due to two factors:

- The bubbles size: The wobbling frequency increases with the bubble size decrease. The smaller the bubble is, the higher its oscillating frequency will be and inversely. However, two limits are to be considered. At a high critical size, large bubbles will split into smaller bubbles so that their vibration frequency cannot decrease indefinitely. The condition of break-up is proposed by the ratio We/Fr which should be smaller than 9. At the other boundary, small bubbles are spherical or ellipsoidal. They do no more vibrate when rising (see Figure 3, part 2.2.2) so that the vibration frequency cannot increase indefinitely.

- The viscosity: Because of the resistance to flow of the liquid, it is obvious that the higher the viscosity, the lower the vibration will be. Figure 78 showed the influence of the viscosity on the bubbles oscillation at about 35 s^{-1}. The non-wobbling state of the rising bubbles is reached for 1.25% CMC solution.

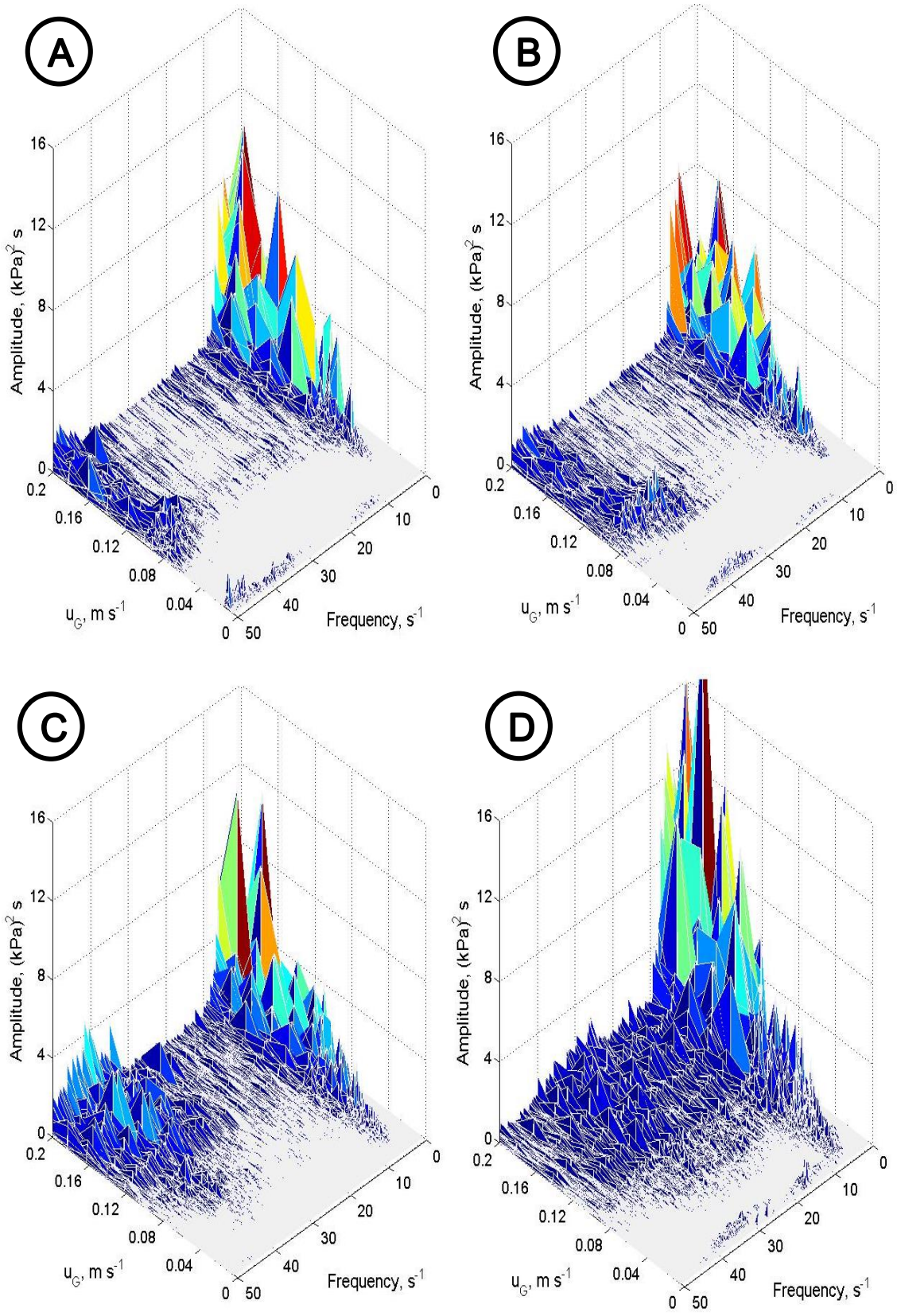

Figure 84: Influence of the viscosity on the peak type 4 frequency with (A) CMC 0.5%, (B) CMC 1.0%, (C) CMC 2.0%, (D) CMC= 4.0% (*P* = 0.1 MPa, sensor 1).

For 1.25% CMC, Figure 85A shows the peak type 4 for the sensor 1 whereas no peak appears (Figure 85B) at higher axial location (sensor 2). The same fact is observed for higher viscosity solution. For 0.50% CMC, the peak type 4 (sensor 1) appears at frequencies higher than 50 s^{-1} (see Figure 86A), whereas at higher axial location, another type of peak appears at about 35 s^{-1} (see Figure 86B). The latter frequency is characteristic of the bubble oscillation, peak type 3. These are evidence of the difference between peak types 3 and 4. The peak type 3 stands for the bubbles vibration whereas the peak type 4 stands for the bubbles formation process (vibration at bubbles formation).

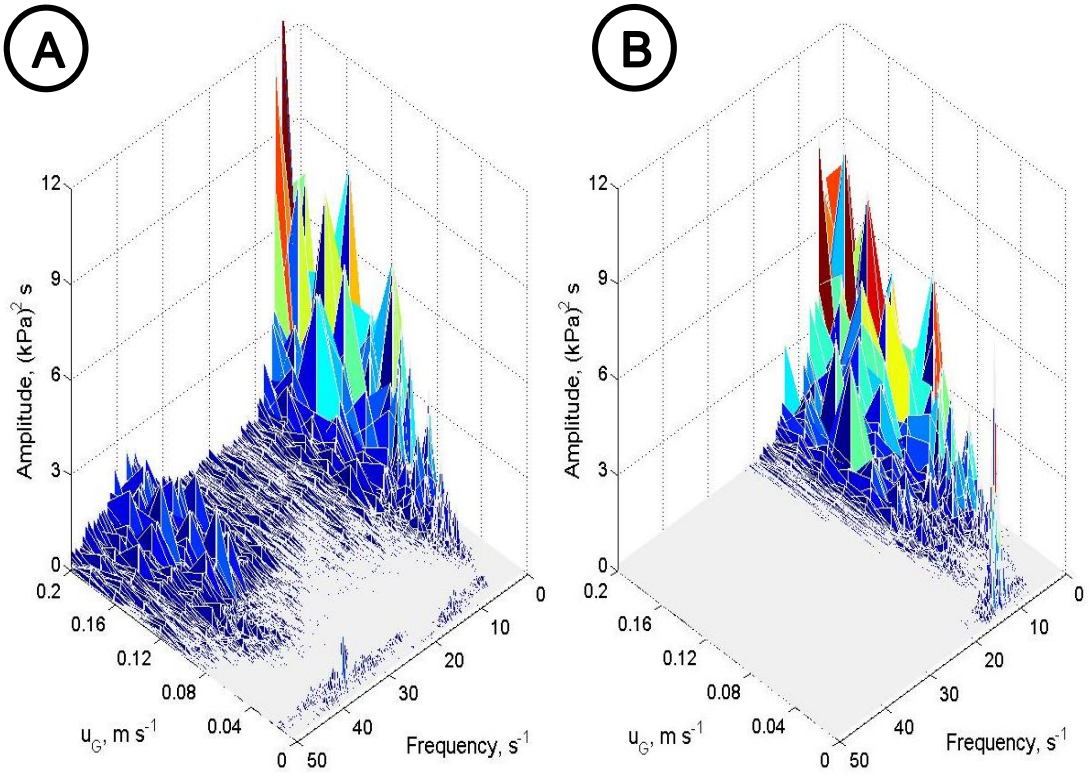

Figure 85: Influence of the sensor axial location on the peak type 4 with (A) sensor 1, (B) sensor 2 (1.25% CMC/nitrogen, *P* = 0.1 MPa).

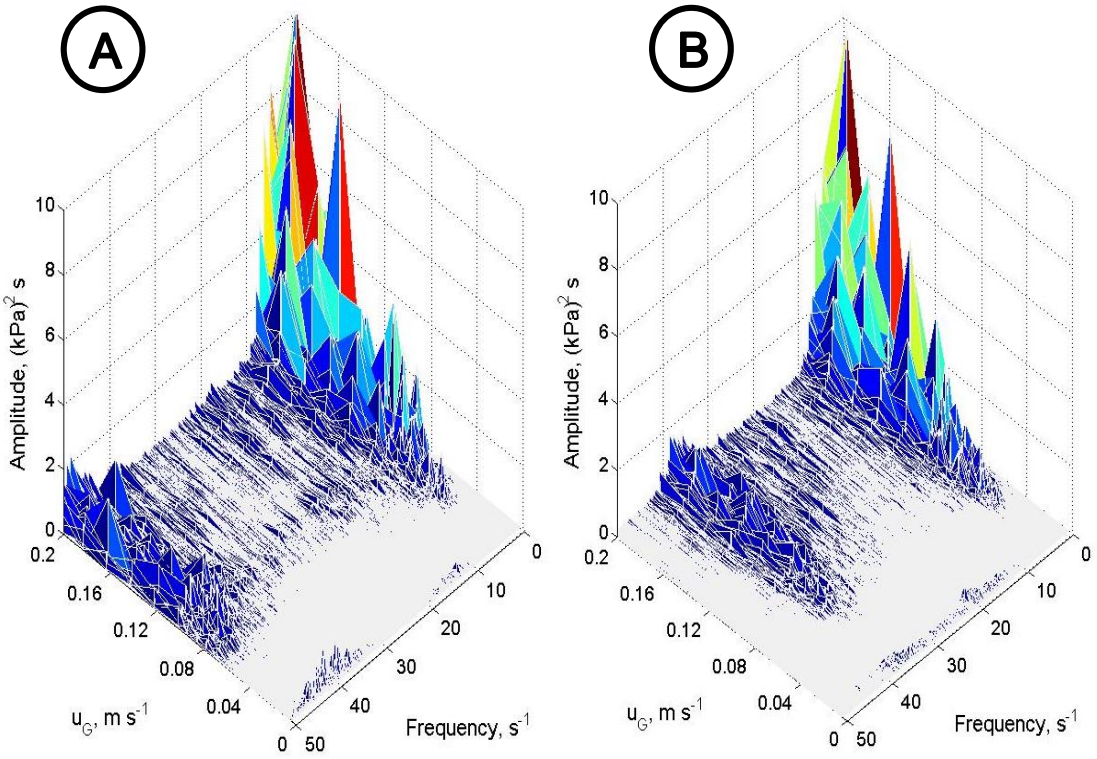

Figure 86: Power spectral density as a function of the superficial gas velocity (A) sensor 1, (B) sensor 2 (0.5% CMC/nitrogen, *P* = 0.1 MPa).

5. Conclusions

In a 0.102 m ID bubble column, various techniques for flow regime identification based on pressure fluctuation measurements were applied. Most experiments were carried out for the system tap water/nitrogen at ambient pressure. Additionally, the pressure was increased up to 2 MPa, the viscosity was varied up to 16 mPa s using ethylene glycol and carboxymethyl cellulose solutions, respectively, and some experiments were performed with toluene.

Four flow regimes could be identified: intermittent, homogeneous, transition and heterogeneous flow. Intermittent flow occurs when the gas flow is too low for continuous bubble formation at all sparger holes (We < 2); at ambient pressure, this occurred at superficial gas velocities $u_G < 0.02$ m s^{-1}. The main flow transition from the homogenous to the transition regime was observed at about 0.045 m s^{-1}. Finally, heterogeneous flow was fully developed at $u_G > 0.10$ m s^{-1}. Since coalescence starts at the top, the critical transition velocities depend slightly and systematically on the axial position of the pressure sensor and on the clear liquid height. The critical velocities decrease as the viscosity is increased and they strongly increase with the pressure.

There are also systematic differences between the various methods and not all transitions can be detected with all methods applied to analyse the pressure fluctuation signal: standard deviation, fractal analysis, Kolmogorov entropy and power spectral density. The Kolmogorov entropy shows a sharp minimum at the main flow transition and, overall, it is the most accurate way of its determination. The fractal analysis also shows a minimum, however, it occurs at a clearly lower gas velocity. Therefore, it must indicate a different reorganisation of the system (perhaps the first bubble clusters formation). Both methods require a variation of the gas velocity in order to locate the minimum. The standard deviation and the power spectral density are less accurate than the Kolmogorov entropy but they are more convenient since the absolute value obtained in a single measurement could be used.

The use of the power spectral density for flow regime identification is a new approach developed in this study. The homogeneous regime is characterized by a clear zone without any peaks. The peaks observed in other flow regimes at certain frequencies could be related to specific pressure sources: The bubbles formation at the sparger was associated

with peaks at 39 s^{-1} while bubbles oscillations during the rise was related to about 35 s^{-1}. Large bubbles eruption at the surface produces peaks at about 13 s^{-1} and liquid bed fluctuations cause low frequency signals at about 4 s^{-1}. The peaks detection threshold and the identification of the pressure sources open a door to the direct detection of the prevailing flow regime.

6. Bibliography

Abdulmouti H. “Bubbly two-phase flow: characteristics, structures, behaviour and flow patterns.” *American Journal of Fluid Dynamics,* 2014: 194-240.

Adkins D. R, Shollenberger K. A., O'Hern T. J., Torczynski J. R. “Pressure effects on bubble column flow characteristics.” *National Heat Transfer Conference Instrumentation and Measurement Symposium, Houston, Texas,* 1996.

Amaya-Bower Luz, Lee Taehum. “Single bubble rising dynamics for moderate Reynolds number using Lattice Boltzmann methode.” *Computers and Fluids, Vol. 39,* 2010: 1191-1207.

Barghi S., Prakash A., Margaritis A., Bergougnou M.A. “Flow regime identification in a slurry bubble column from gas hold-up and pressure fluctuation analysis.” *The Canadian Journal of Chemical Engineering, Vol. 82,* 2004: 865-870.

Bhaga D., Weber M. E. “Bubbles in viscous liquids: shapes, wake and velocities.” *Journal of Fluid Mechanics, Vol. 105,* 1981: 61-65.

Brennen C. E. *Cavitation and Bubbles Dynamics.* Pasadena, California: Oxford University Press, 1995.

Brennen C. E. *Fundamentals of Multiphase Flows.* Pasadena, California: Cambridge University Press, 2005.

Briens L. A., Briens C. L., Margaritis A., Hay J. “Minimum fluidization and gas maldistribution in fluidized beds.” *Journal of the American Institute of Chemical Engineering, Vol. 43,* 1997: 1180-1189.

Camarasa E., Carvahlo E., Meleiro L. A. C., Maciel Filho R., Domingues A., Wild G., Poncin S., Midoux N., Bouillard J. “Development of a complete model for an air-lift reactor.” *Chemical Engineering Science, Vol. 56,* 2001: 493-503.

Chilekar V. P. *Hydrodynamics and mass transfer in slurry bubble columns: scale and pressure effects.* Eindhoven: Eindhoven University of Technology, 2007.

Chilekar V. P., van der Schaaf J., Kuster B. F. M., Tinge J. T.,. “Influence of elevated pressure and particle lyophobicity on hydrodynamics and gas–liquid mass transfer in slurry bubble columns.” *Journal of the American Institute of Chemical Engineering, Vol. 56,* 2010: 584-596.

Clift R., Grace J. R., Weber M. E. *Bubbles, Drops and Particles.* New York, San Francisco, London: Acadenmic Press, 1978.

Davidson J. F., Schüler B. O. G. “Bubble formation at an orifice in a viscous liquid.” *Transactions of the Institution of Chemical Engineers, Vol. 38*, 1960: 105-115.

Deckwer W. D., Schumpe A. “Viscous media in tower bioreactors: Hydrodynamic characteristics and mass transfer properties.” *Bioprocess Engineering, Vol. 2*, 1987: 79-94.

Deckwer W.-D. *Bubble Column Reactors.* West Sussex: John Wiley and Sons, 1992.

Drahoš J., Bradka F., Puncochar M. “Fractal behaviour of pressure fluctuations in a bubble column.” *Chemical Engineering Science, Vol. 47*, 1992: 4069-4075.

Drahoš J., Cermak J. “Diagnostics of gas-liquid flow pattern in chemical engineering systems.” *Chemical Engineering Processing, Vol. 26*, 1989: 148-164.

Drahoš J., Tihon J., Serio C., Lübbert A. “Deterministic chaos analysis of pressure fluctuations in a horizontal pipe at intermittent flow regime.” *The Chemical Engineering Journal, Vol. 64*, 1996: 149-156.

Drahoš J., Zahradnik J., Puncochar M., Fialova M., Bradka F. “Effect of operating conditions on the characteristics of pressure fluctuations in a bubble column.” *Chemical Engineering Processing, Vol. 29*, 1991: 107-115.

Elperin T., Klochko M. “Flow regime identification in a two-phase flow using wavelet transform.” *Experiments in Fluids, Vol. 32*, 2002: 674-682.

Franca F., Acrikgoz M., Laheh Jr R. T., Clausse A. “The use of fractal techniques for flow regime identification.” *International Journal of Multiphase Flow, Vol. 17*, 1991: 545-552.

Gaddis E. S., Vogelpohl A. “Bubble formation in quiescent liquids under constant flow conditions.” *Chemical Engineering Science, Vol. 41*, 1986: 97-105.

Gerardus A. W. *Path and wake of a rising bubble.* Twente, The Netherlands: A.W.G. de Vries, 2001.

Gourich B, Vial C., Essadki A. H., Allam F., Soulami M. B., Ziyad M. “Identification of flow regimes and transition points in a bubble column through analysis of differential pressure signal—Influence of the coalescence behavior of the liquid phase.” *Chemical Engineering and Processing, Vol. 45*, 2006: 214-223.

Grund G., Schumpe A. “The gas disengagement technique for studying gas hold-up structure in bubble columns.” *The Canadian Journal of Chemical Engineering, Vol. 64*, 1986: 881-896.

Hristov J. “Benchmarking of the construct of dimensionless correlations regarding batch bubble columns with suspended solids: Performance of the pressure transform approach.” *International Review of Chemical Engineering, Vol. 1*, 2009: 475-483.

Hurst H. E. “Long terme storage capacity of reservoirs.” *Transaction of the American Society of Civil Engineers*, 1852: 770-808.

Idogawa K., Ikeda K., Fukuda T. “Formation and flow of gas bubbles in a pressurized bubble column with a single orifice or nozzle gas distributor.” *Chemical Engineering Communication, Vol. 59*, 1987: 201-212.

Jordan U., Saxena A., Schumpe A. “Dynamic gas disengagement in a high pressure bubble column.” *The Canadian Journal of Chemical Engineering, Vol. 81*, 2003: 491-498.

Kang Y., Cho Y.J., Woo K.J., Kim K.I., Kim S.D. “Bubble properties and pressure fluctuations in pressurized bubble columns.” *Chemical Engineering Science, Vol. 55*, 2000: 411-419.

Kantarci N., Borak F., Ulgen K. O. “Bubble column reactors.” *Process Biochemistry, Vol. 40*, 2005: 2263-2283.

Kazakis N. A., Papadopoulous I. D., Mouza A. A. “Bubble columns with fine pore sparger operating in the pseudo-homogeneous regime: Gas hold-up prediction and a criterion for the transition to the heterogeneous regime.” *Chemical Engineering Science, Vol. 62*, 2007: 3091-3103.

Kientzler C. F., Arons A. B., Blanchard D. C., Woodcock A. H. “Photographic investigation of the projection of droplets by bubbles bursting at a water surface.” *Tellus, A Quartesly Journal of Geophysics; Vol. 6*, 1954: 1-7.

Kumar R., Kuloor N. R. “Bubble formation in viscous liquids under constant flow conditions.” *The Canadian Journal of Chemical Engineering, Vol. 48*, 1970: 383-388.

Lanauze D., HARRIS I. J. “Gas bubble formation at elevated system pressure.” *Transactions of the Institution of Chemical Engineers, Vol. 52*, 1974: 337-348.

Lee J. S., Weon B. M., Park J. S., Je J. H., Fezzaa K., Lee W.-K. “Size limits the formation of liquid jets during bubble bursting.” *Nature Communication*, 2011: 1-7.

Letzel H. M., Schouten J. C., Krishna R., van den Bleek C. M. “Characterization of regimes and regime transitions in bubble columns by chaos analysis of pressure signals.” *Chemical Engineering Science, Vol. 52*, 1997: 4447-4459.

Letzel H. M., Schouten J. C., Krishna R., van den Bleek C. M. "Gas hold-up and mass transfer in bubble column reactors operated at high pressure." *Chemical Engineering Science, Vol. 54*, 1999: 2237-2246.

Letzel H. M., Schouten J. C., van den Bleek C. M., Krishna R. "Influence of elevated pressure on the stability of bubbly flows." *Chemical Engineering Science, Vol. 52*, 1997: 3733-3739.

Li W. -L., Zhong W.-Q., Jin B.-S., Xiao R., He T. -T. "Flow regime identification in a three-phase bubble column based on statistical, Hurst, Hilbert–Huang transform and Shannon entropy analysis." *Chemical Engineering Science, Vol. 102*, 2013: 474-485.

Lin T. J., Tsuchiya K., Fan L. -S. "On the measurements of regime transition in high-pressure bubble columns." *The Canadian Journal of Chemical Engineering, Vol. 77*, 1999: 370-374.

Lin T.-J., Juang R.C., Chen Y.-C., Chen C.-C. "Predictions of flow transitions in a bubble column by chaotic time series analysis of pressure fluctuation signals." *Chemical Engineering Science, Vol. 56*, 2001: 1057-1065.

Li-shun H., Xing-jun W., Guang-suo Y., Yi-fei W., Zhi-jie Z., Fu-chen W., Zun-hong Y. "Chaotic analysis of pressure fluctuation signal in the gas-liquid-solid slurry column." *Nonlinear Analysis: Real World Application, Vol. 10*, 2009: 410-415.

Luo X., Lee D. J., Ölau R., Yang G., Fan L. -S. "Maximun stable bubble size and gas hold-up in high pressure slurry bubble columns." *Journal of the American Institute of Chemical Engineering - Fluid Mechanics and Transport Phenomena, Vol. 45*, 1999: 665-680.

Manish R. B., Jyeshtharaj B. J. "Stability analysis of bubble columns: Predictions for regime transition." *Chemical Engineering Science, Vol. 60*, 2005: 4493-4507.

Matsui G. "Identification of flow regimes in vertical gas liquid two phase flow using differential pressure fluctuations." *International Journal of Multiphase Flow, Vol. 10*, 1984: 711-720.

Matsui G. "Automatic identification of flow regimes in vertical two-phase flow using differential pressure fluctuations." *Nuclear Engineerig and Design, Vol. 95*, 1986: 221-231.

Mersmann A. "Design and scale-up of bubble and spray column." *German Chemical Engineering, Vol. 1*, 1978: 1-11.

Nedeltchev S., Jordan U., Lorenz O., Schumpe A. "Identification of various transition velocities in a bubble volumn based on Kolmogorov entropy." *Chemical Engineering Technology, Vol. 30*, 2007: 534-539.

Nedeltchev S., Shaikh A. “A new method for identification of the main transition velocities in multiphase reactors based on information entropy theory.” *Chemical Engineering Science, Vol. 100*, 2013: 2-14.

Oolman T. O., Blanch H. W. “Bubble coalescence in stagnant liquids.” *Chemical Engineering Communications, Vol. 43*, 1986: 237-261.

Oyevaar M. H., Westerterp K. R. “Mass transfer phenomena and hydrodynamics in agitated gas-liquid reactors and bubble columns at elevated pressures state of the art.” *Chemical Engineering Processing, Vol. 25*, 1989: 85-98.

Park S. H., Kang Y., Cho Y. J., Fan L. T., Kim S. D. “Characterization of pressure signal in a bubble column by wavelet transform.” *Journal of Chemical Engineering of Japan*, 2001: 158-165.

Qian D., McLaughlin J. B., Sankaranarayanan K., Sundaresan S., Kontomaris K. “Simulation of bubble break-up dynamics in homogeneous turbulence.” *Chemical Engineering Communications, Vol. 193*, 2006: 1038-1063.

Räbiger N. *Blasenbildung an Düsen sowie Blasenbewegung in ruhenden und strömenden newtonschen und nichtnewtonschen Flüssigkeiten.* Düsseldorf: VDI-Verlag, 1984.

Ramakrishnan S., Kumar R., Kulor N. R. “Studies in bubble formation: 1. bubble formation under constant flow conditions.” *Chemical Engineering Science, Vol. 24*, 1969: 731-747.

Reilly I. G., Scott D. S., Bruijn T. J. W., MacIntyre D. “The role of the phase momentum in dertermining gas hold-up and hydrodynamic flow regimes in bubble column operations.” *The Canadian Journal of Chemical Engineering, Vol. 72*, 1994: 3-12.

Ribeiro Jr P. C. “On the estimation of the regime transition point in bubble columns.” *Chemical Engineering Journal, Vol. 140*, 2008: 473-482.

Rosenbaum A., A. *Hydrodynamics of viscous liquids in bubble columns.* Master Engineering Thesis, Universidad Nacional del Comahue, Neuquen, 2015.

Ruzicka M. C., Drahos J., Fialova M., Thomas N. H. “Effect of bubble column dimensions on flow regime transition.” *Chemical Engineering Science, Vol. 56*, 2001: 6117-6124.

Ruzicka M. C., Drahos J., Mena P. C., Teixeira J. A. “Effect of viscosity on homogeneous–heterogeneous flow regime transition in bubble columns.” *Chemical Engineering Journal, Vol. 96*, 2003: 15-22.

Ruzicka M. C., Zahradnik J., Drahoš J., Thomas N. H. “Homogeneous–heterogeneous regime transition in bubble columns.” *Chemical Engineering Science, Vol. 56*, 2001: 4609-4626.

Scheid C. M., Puget F. P., Halasz M. R. T., Massarani G. “Fluid dynamics of bubbles in liquid.” *Brazilian Journal of Chemical Engineering, Vol. 16*, 1999: 351-362.

Schouten J. C., Takens F., van den Bleek C. M. “Maximum-Likehood estimation of the entropy of an attractor.” *The American Physical Society, Vol. 49*, 1994: 126-129.

Schouten J. C., Takens F., van den Bleek C. M. “Estimation of the dimension of a noisy attractor.” *The American Physical Society, Vol. 50*, 1994: 1851-1861.

Shaban H., Tavoularis S. “Identification of flow regime in vertical upward air–water pipe flow using differential pressure signals and elastic maps.” *International Journal of Multiphase Flow, Vol. 61*, 2014: 62-72.

Shah Y. T., Keökar B. G., Deckwer W. -D. “Design parameters estimation for bubble column reactors.” *Journal of the American Institute of Chemical Engineering, Vol. 28*, 1982: 353-379.

Shaikh A., Al-Dahhan M. H. “A review on flow regime transition in bubble columns.” *International Journal of Chemical Reactor Engineering, Vol. 5*, 2007: 1-68.

Shnip A. I., Kolhatkar R. V., Swamy D., Joshi J. B. “Criteria for the transition from the homogeneous to the heterogeneous regime in two-dimensional bubble column reactors.” *Internation Journal of Multiphase Flow, Vol. 18*, 1992: 705-726.

Sriram R., Mann R. “Dynamic gas disengagement: A new technique for assessing the behaviour of bubble columns.” *Chemical Engineering Science, Vol. 32*, 1977: 571-580.

Tutu N. K. “Pressure drop fluctuatuations and bubble-slug transition in a vertical two phase air-water flow.” *International Journal of Multiphase Flow, Vol. 2*, 1984: 211-216.

Tutu N. K. “Pressure fluctuatuations and flow pattern recognition in vertical two phase gas-liquid flow.” *International Journal of Multiphase Flow, Vol. 4*, 1982: 443-447.

Veldhuis C., Biesheuvel A., Van Wijngaarden L. “Schape oscillations on bubbles rising in clean and tap water.” *Physics of Fluids, Vol. 20*, 2008: 1-12.

Vial C., Camarasa E., Poncin S., Wild G., Midoux N., Bouillard J. “Study of the hydrodynamic behaviour in bubble column and external loop airlift reactors through analysis of pressure fluctuations.” *Chemical Engineerng Science, Vol. 55*, 2000: 2957-2973.

Vial C., Poncin S., Wild G., Midoux N. “A simple method for regime identification and flow characterisation in bubble columns and airlift reactors.” *Chemical Engineering and Processing, Vol. 40*, 2001: 135-151.

Vince M. A., Lahey Jr. R.T. “On the development of an objective flow regime indicator.” *International Journal of Multiphase Flow, Vol. 8*, 1982: 93-124.

Waheed A. A. -M., Emad M. A., Mohamed N. A. -K. “Prediction of regime transitions in bubble columns using acoustic and differential pressure signals.” *Chemical Engineering Journal, Vol. 133*, 2007: 139-149.

Wallis G. B. *One-dimensional two-phase flow.* New York: McGraw-Hill, 1969.

Wild G., Poncin S., Li H. -Z., Olmos E. “Some aspects of the hydrodynamics of bubble columns.” *International Journal of Chemical Reactor Engineering, Vol. 1*, 2003: 1-36.

Wilkinson P. M., Spek A. P., van Dierendonck L. L. “Design parameters estimation for scale-up of high-pressure bubble columns.” *Journal of the American Institute of Chemical Engineering, Vol. 38*, 1992: 544-554.

Yang J. H., Yang J.-II., Kim H. J., Chun D. H., Lee H. -T., Jung H. “Two regime transitions to pseudo-homogeneous and heterogeneous bubble flow for various liquid viscosities.” *Chemical Engineering and Processing: Process Intensification, Vol. 10*, 2010: 1044-1050.

Zahradnik J., Fialová M., Ruzicka M., Drahos J., Kastánek., Thomas N. M. “Duality of the gas-liquid flow regimes in bubble column reactors.” *Chemical Engineering Science, Vol. 52*, 1997: 3811-3826.

Zhang J.-P., Grace J.R., Epstein N., Lim K.S. “Flow regime identification in gas-liquid flow and three-phase fluidized beds.” *Chemical Engineering Science, Vol. 52*, 1997: 3979-3992.

Zhang W. -H., Li H., Li X. “Identification of regime transitions in an inner-loop airlift reactor using local bubble-induced pressure fluctuation signals.” *Chemical Engineering Science, Vol. 162*, 2010: 296-300.

Zhang W. -H., Li X. “Origin of pressure fluctuations in an internal-loop airlift reactor and its application in flow regime detection.” *Chemical Engineering Science, Vol. 64*, 2009: 1009-1018.

Zuber N., Findlay J. A. “Average volumetric concentration in two-phase flow systems.” *Journal of Heat Transfer*, 1965: 453-468.

7. Annexes

7.1 The Hurst exponent (*H*) determination

For the Hurst exponent determination, the signal is characterised according to the rescaled range R/S theory. R/S is firstly determined for the whole signal. The next step is the determination of its mean value for both half parts of the initial signal (meaning n = 2). The same procedure is followed for smaller segments of the initial signal (increasing values of n) till a critical vector dimension fixed at 1250 in our case.

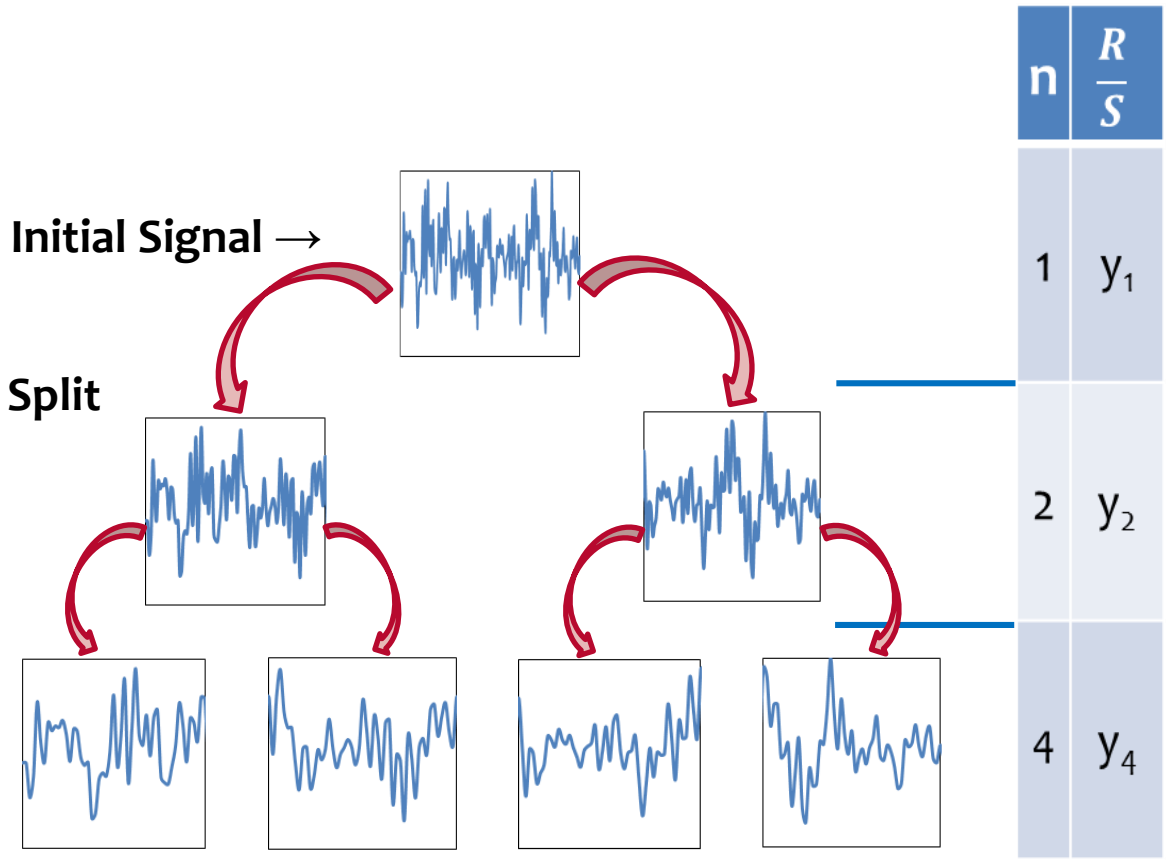

Figure 87: Hurst exponent determination.

As shown on the following Figure, the logarithm of segments amount represent the x values whereas the logarithm of their corresponding R/S value represent the y values. The slope of the strait line obtained thanks to a linear regression is the Hurst coefficient (*H*) to be determined.

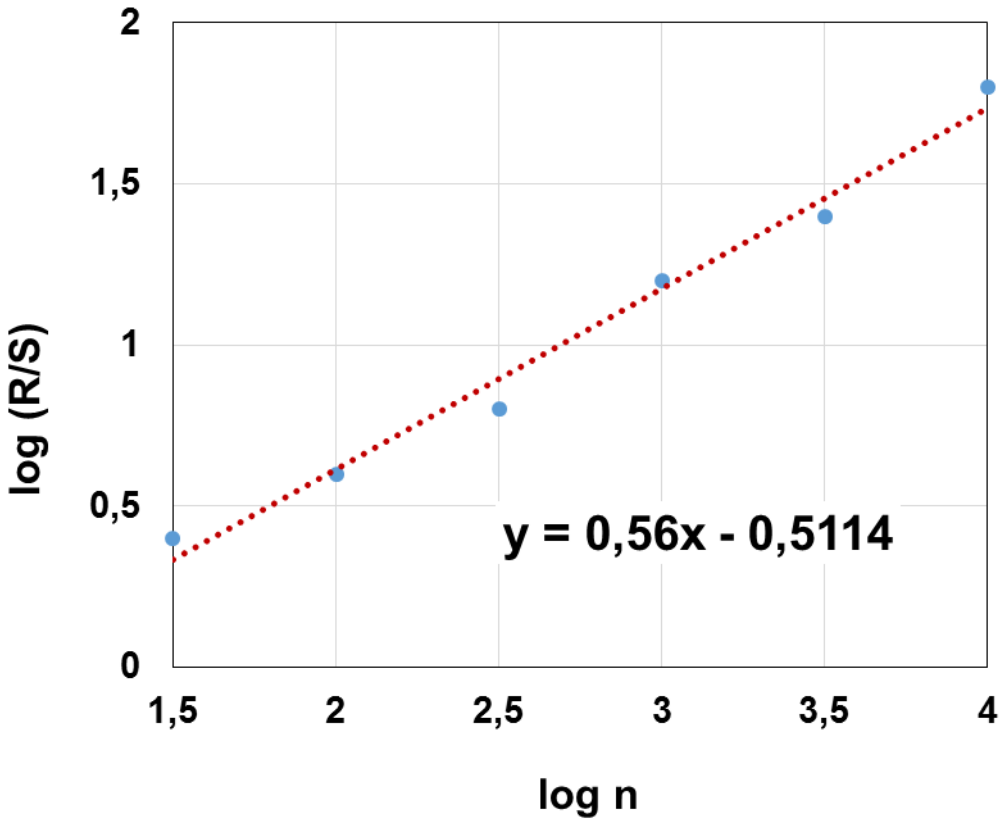

Figure 88: Rescaled range analysis.

In the formula R/S,

$$\boldsymbol{R = V_{max} - V_{min}}\,,$$

with $\boldsymbol{V\ (N,k) = \sum_{i=1}^{k}[P(t_i) - \bar{P}\ (\tau)]}$ for $1 \leq k \leq N$

S is the standard deviation.

7.2 The Kolmogorov entropy determination

The Kolmogorov entropy is based on the reconstruction of the initial signal in orbitals. For the same signal, the first figure shows initially closed and well-ordered orbitals at $t+\tau_1$. For $t+\tau_2$, the second figure shows distanced and disorganised orbitals. The method determines the time necessary for two initially closed vectors (first figure) to diverge (second figure). The distance between the vectors is determined with the norm whereas the orbitals proximity is considered for the vectors norm smaller than the average absolute deviation. The vectors dimension varies from 50 to 100.

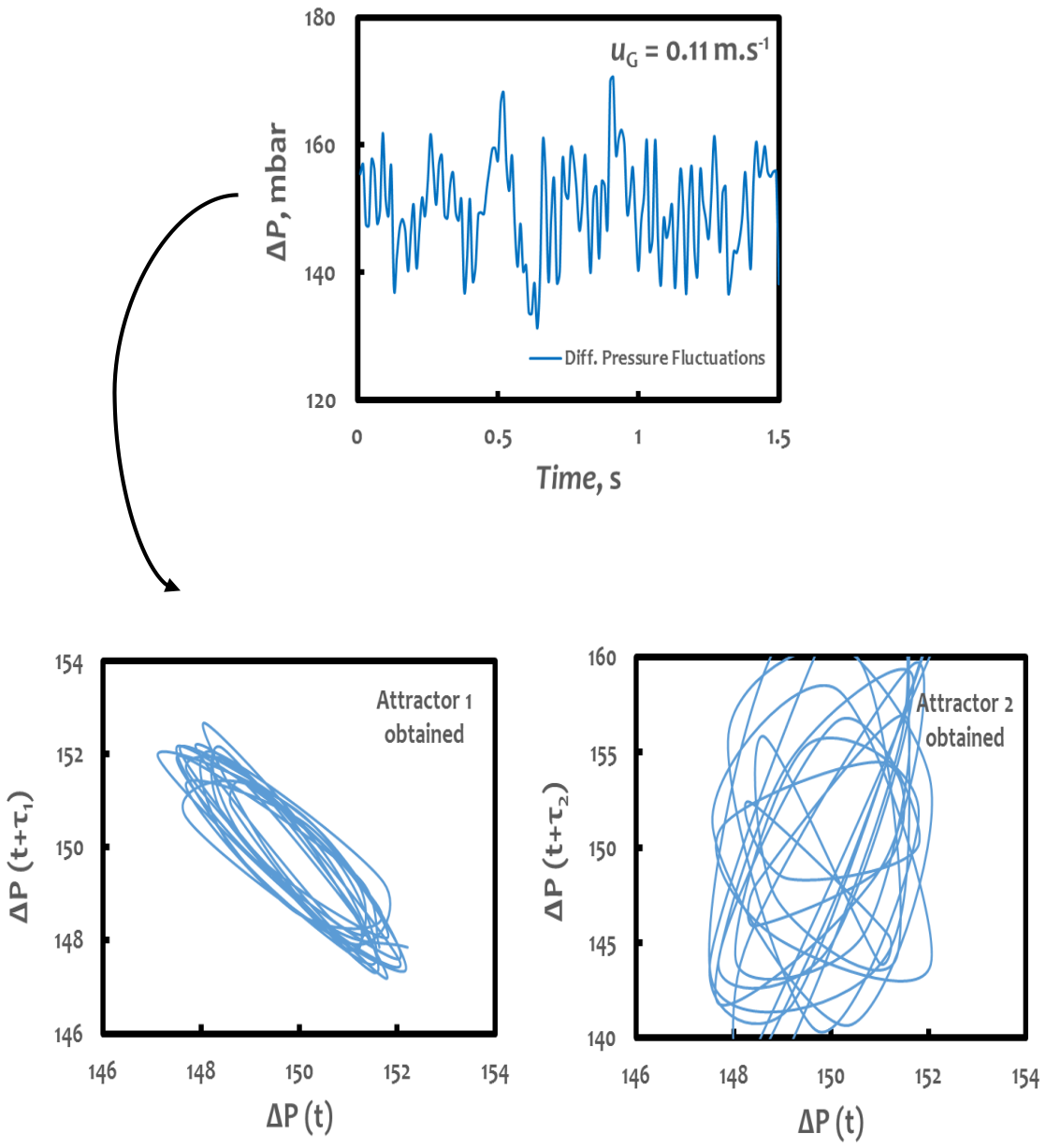

Figure 89: Kolmogorov entropy determination.